

Enrico Chlechowicz

**Plasmastrom- und Druckmessungen am WEGA Stellarator**

**Plasma Current and Pressure Measurements at the WEGA Stellarator**

**IPP 13/19  
September, 2010**



Ernst-Moritz-Arndt-Universität Greifswald  
Institut für Physik



Max-Planck-Institut für Plasmaphysik  
Teilinstitut Greifswald

## **DIplomARBEIT**

# Plasma Current and Pressure Measurements at the WEGA Stellarator

zum  
Erlangen des akademischen Grades

## **DIplomPHYSIKER** (Dipl.-Phys.)

Vorgelegt von: Enrico Chlechowicz  
geboren am: 21. April 1984 in: Eberswalde-Finow

Erstgutachter: Prof. Dr. Dr. h.c. Friedrich Wagner  
Zweitgutachter: Prof. Dr. André Melzer  
Betreuer: PD Dr. Heinrich Peter Laqua  
Tag der Einreichung: 23. April 2010



---

## **Abstract**

Magnetic diagnostics represent a fundamental module in all fusion experiments. They allow contactless access to basic parameters of high temperature plasmas, which are indispensable for magnetic confinement experiments. The aim of this work was to build up different magnetic diagnostics in order to measure the plasma current and the plasma pressure. After an introduction, the fundamentals of plasma current and pressure are given. In the next section, the principle of magnetic diagnostics, as well as the setup installed at WEGA, is described. Lastly, the measurements from different plasma scenarios are presented before a summary and an outlook will be given.



# Contents

<b>1</b>	<b>Introduction</b>	<b>1</b>
1.1	Nuclear Fusion . . . . .	1
1.2	Magnetic Confinement . . . . .	3
1.2.1	Gyration of single particles . . . . .	3
1.2.2	Toroidal Magnetic Confinement . . . . .	4
1.3	The WEGA Stellarator . . . . .	7
1.3.1	Setup . . . . .	7
1.3.2	Plasma heating . . . . .	8
1.3.3	Diagnostics . . . . .	9
<b>2</b>	<b>Fundamentals of Plasma Current and Pressure in Fusion Devices</b>	<b>11</b>
2.1	Diamagnetism in Plasmas . . . . .	11
2.2	Plasma Pressure and $\beta$ . . . . .	18
2.3	Plasma Waves Relevant for Current Drive . . . . .	20
2.3.1	Electron Cyclotron Wave . . . . .	20
2.3.2	Electron Bernstein Wave . . . . .	21
2.3.3	Lower Hybrid Wave . . . . .	21
2.3.4	Doppler shift . . . . .	23
2.4	Plasma Currents in Toroidal Magnetic Confinement . . . . .	23
2.4.1	Plasma Current Drive Efficiency . . . . .	24
2.4.2	Inductive Current Drive . . . . .	25
2.4.3	Electron Cyclotron Current Drive . . . . .	26
2.4.4	Lower Hybrid Current Drive . . . . .	28
2.4.5	Electron Bernstein Wave Current Drive . . . . .	30
2.4.6	Bootstrap Current . . . . .	30
2.4.7	Pfirsch-Schlüter Current . . . . .	32
2.5	Spitzer Resistivity . . . . .	32
<b>3</b>	<b>Magnetic Diagnostics</b>	<b>35</b>
3.1	Inductive Magnetic Diagnostics . . . . .	35
3.1.1	Rogowski Coil . . . . .	35
3.1.2	Diamagnetic and Compensation Loop . . . . .	37
3.1.3	Toroidal Flux Loop . . . . .	38
3.2	Systems for Determination of the Diamagnetic Effect . . . . .	39
3.2.1	Diamagnetic and Compensation Loop System . . . . .	39
3.2.2	Two Loop System . . . . .	39

3.3	Integrators . . . . .	41
3.3.1	Analog Integrators . . . . .	41
3.3.2	Digital Integrators . . . . .	42
<b>4</b>	<b>Diagnostic Setup at the WEGA Stellarator</b>	<b>45</b>
4.1	Assembling of Magnetic Loops . . . . .	45
4.1.1	Diagnostic Requirements . . . . .	46
4.1.2	Diamagnetic Loop . . . . .	46
4.1.3	Compensation Loop . . . . .	49
4.1.4	Two Loop System . . . . .	51
4.1.5	Rogowski Coils . . . . .	52
4.1.6	Place of Location . . . . .	52
4.1.7	Alignment of Magnetic Diagnostic . . . . .	55
4.2	Digital Integrator . . . . .	56
4.2.1	Reconstruction and Integration Algorithm . . . . .	56
4.2.2	Suppression of Leaking Voltages . . . . .	60
4.2.3	Clock Frequency Optimization . . . . .	61
4.2.4	Amplifier Setting . . . . .	61
4.3	Data Acquisition and Processing . . . . .	62
<b>5</b>	<b>Experimental Results</b>	<b>65</b>
5.1	Calibration . . . . .	66
5.1.1	Setup for Calibration of Magnetic Diagnostics . . . . .	66
5.1.2	Results . . . . .	67
5.2	Plasma Currents in Resonantly Electron Cyclotron Heated Discharges	70
5.3	Lower Hybrid Current Drive Experiments . . . . .	74
5.4	Plasma Currents in OXB Heated Discharges . . . . .	79
5.5	Inductive Current Drive Measurements . . . . .	85
5.6	Plasma Pressure Measurements . . . . .	87
<b>6</b>	<b>Summary</b>	<b>95</b>
<b>7</b>	<b>Outlook</b>	<b>99</b>
<b>8</b>	<b>Appendix</b>	<b>103</b>

# 1 Introduction

Aristotle<sup>1</sup> once said “Wonder is the beginning of all science.” In respect thereof, the sun has inspired mankind for thousands of years prompting much research of this heavenly body. From the study of the orbits of the luminaries in the ancient world, to Wollaston and Fraunhofer, who were the pioneers in the exploration of the composition of the sun, and the satellites which can three-dimensionally investigate the interaction of mass eruption and the Earth’s magnetic field today, the sun has been a research topic for hundreds of generations.

Further highlights represent the experiments with the aim to let a sun burn on earth, and to be able to use their inner processes to make this potential of energy gain available for the mankind.

## 1.1 Nuclear Fusion

A wide variety of particle processes take place in the sun. The dominant fusion process occurring in the sun is the so-called proton-proton-process, which was firstly described by Bethe in 1938 [Bet39]. The principle of fusion is, however, also applicable wherever the binding energy of the starting material is less compared to the reaction products. An overview of the binding energies per nucleon depending on the mass number  $A$  is given in figure 1.1 where a maximum is reached for iron with  $A = 56$ . Thus, an energy gain can occur by means of fusion of light to heavy particles or by fission of heavy to light particles.

In the proton-proton processes helium is created in a sequence of sub processes based on the reaction of protons with each other. However, this process is not applicable on earth, since the reaction rate on sun (caused by the high particle densities) cannot be reached on earth. Nevertheless, using a process based on deuterium and tritium much higher reaction rates  $\langle \sigma v \rangle$  can be achieved at much lower energies as seen in figure 1.2. In order to generate fusion processes the Coulomb barrier of the participating particles has to be overcome which is possible by means of quantum-mechanical tunneling.

---

<sup>1</sup>Greek philosopher who lived between 384 BC and 322 BC



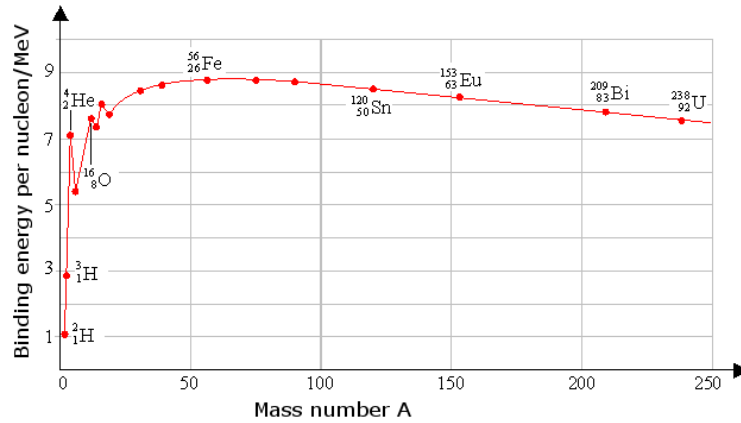


**Figure 1.1:** Binding energy per nucleon in dependency on the mass number  $A$

For this purpose high energies are required which are in the order of  $10 \text{ keV}^2$  as seen in figure 1.2 for a fusion power plant. At these energies, the starting material becomes an ionized gas which is referred to as plasma.

After tunneling the Coulomb barrier the strong interaction occurs leading to the generation of a compound particle. Due to the instability of this particle, a decay into an alpha particle (ionized helium) and a neutron takes place as well an energy release of 17.6 MeV.



This power results from the difference of the binding energies between the starting and reaction products. 4/5 of this power is carried as kinetic energy by the neutron and 1/5 by the alpha particle. This energy can be used on the one hand for further plasma heating through collisions, required to reach the desired reaction rates, and on the other hand for conventional generation of energy by means of heat exchanger and turbines. Additionally the neutron is used for tritium production by fission of lithium, since tritium is not available on earth in sufficient manner. In order to use fusion for energy production on earth different concepts exist. These are the inertial fusion and the magnetic confinement, where the latter is the subject of this work.

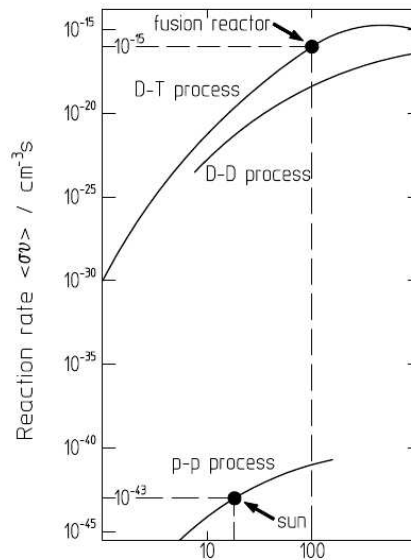


**Figure 1.2:** Reactions rate for possible fusion processes in dependence on the temperature [Har07]

<sup>2</sup>In plasma physics the energy of particles is usually given as a temperature where  $1 \text{ eV} = 11605 \text{ K}$  under the condition of a Maxwell distribution in a thermodynamic equilibrium.

The condition for a continuous self sustained fusion without external heating is given by the Lawson criterion, which balances the energy loss from the reactor character with the gain of energy through fusion itself. The result is that the product of the electron density  $n_e$  times the ion temperature  $T_i$  times the energy confinement time  $\tau_E$ , which describes the quality of heat confinement, has to exceed a value of

$$n_e T_i \tau_E = 2.8 \cdot 10^{24} \frac{\text{eV s}}{\text{m}^3} . \quad (1.2)$$

Previous experiments reached a value of a maximal 60% compared to the required value above. However, the experiment ITER, which is currently under construction, shall fulfill this criterion for the first time.

## 1.2 Magnetic Confinement

Magnetic confinement as opportunity to realize fusion is based on compelling charged particles on trajectories, which are determined by a certain magnetic field topology. Here, different ways of realization exist, which are characterized in section 1.2.2. However, the origin of the particle movement will be explained before.

### 1.2.1 Gyration of single particles

Starting point for the deviation of the trajectories of particles with a charge  $q_k$  and a mass  $m_k$  is the general equation of motion

$$\gamma m_k \frac{d\vec{v}_k}{dt} = q_k \left( \vec{E} + \vec{v}_k \times \vec{B} \right) + \vec{F}_{ext} \quad (1.3)$$

with the external force  $\vec{F}_{ext}$ , the electric field  $\vec{E}$ , the magnetic field  $\vec{B}$ , the particle velocity  $v_k$  and the relativistic factor  $\gamma$ . In case of a vanishing electric field and external force, the particle motion is determined by the Lorentz force

$$\vec{F}_L = \gamma m_k \frac{d\vec{v}_k}{dt} = q_k \left( \vec{v}_k \times \vec{B} \right) . \quad (1.4)$$

If the coordinate system is chosen such that the constant magnetic field shows in z-direction  $\vec{B} = B_z \vec{e}_z$ , equation (1.4) can be rewritten in vector components as

$$\begin{aligned} \frac{d^2 v_{k;x,y}}{dt^2} &= - \left( \frac{q_k B_z}{\gamma m_k} \right)^2 v_{k;x,y} \\ &= - \left( \frac{\omega_{c,k}}{\gamma} \right)^2 v_{k;x,y} \end{aligned} \quad (1.5)$$

$$\frac{dv_{k;z}}{dt} = 0 \quad (1.6)$$

where  $\omega_{c,k}$  represents the positively defined cyclotron frequency of electrons and ions, respectively

$$\omega_{c,k} = \frac{|q_k|B_z}{m_k} \quad (1.7)$$

In case of a non-relativistic motion the solution of equation (1.6) for the single components results in the trajectory  $\vec{r}(t)$  given by

$$\vec{r}_k(t) = \pm \frac{v_{\perp,k}}{\omega_{c,k}} \sin(\omega_{c,k}t) \vec{e}_x \mp \frac{v_{\perp,k}}{\omega_{c,k}} \cos(\omega_{c,k}t) \vec{e}_y + v_{\parallel,k}t \vec{e}_z \quad (1.8)$$

with  $v_{\parallel} = v_z$  as the parallel velocity along the magnetic field lines and  $v_{\perp} = \sqrt{v_x^2 + v_y^2}$  as the velocity component perpendicular to the field lines. The upper sign in equation (1.8) holds for electrons and the lower one for ions. With a finite  $v_{\parallel,k}$  the particle follows a spiral orbit spinning around the magnetic field line. This can be seen in figure 1.3. Projecting the orbit onto the x-y-plane, the particle trajectory is a circle with the radius

$$r_{L,k} = \frac{m_k v_{\perp,k}}{|q_k|B} \quad (1.9)$$

which is called Lamor radius.

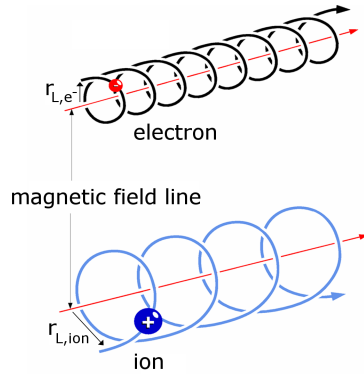


**Figure 1.3:** Motion of charged particles along magnetic field lines

Thus, with an appropriate field topology the plasma can be confined in a contactless way since the particles follow the magnetic field lines.

## 1.2.2 Toroidal Magnetic Confinement

With knowledge of the Lawson criterion and the achievable densities and temperatures of the plasma in a fusion reactor the confinement time needs to be about one second. This is the essential condition for continuous energy production and therefore for the confinement device.

A pure linear confinement along a straight magnetic field line can only be guaranteed, if the magnetic field strength on the end is increased, so that a so-called mirror configuration is generated. As an example for this confinement method, the charged particles in the magnetosphere are trapped by the earth's magnetic dipole. These particles form the van Allen radiation belt [Wag07]. However, there exists also the probability that particles escape from the mirror leading to the result that this method is unsuitable for fusion since  $\tau_E \ll 1$  s. A solution presents the confinement by enclosing the field lines in a toroidal geometry by means of a toroidal magnetic field [Nüh07]. The related coordinate system is shown in figure 1.4.

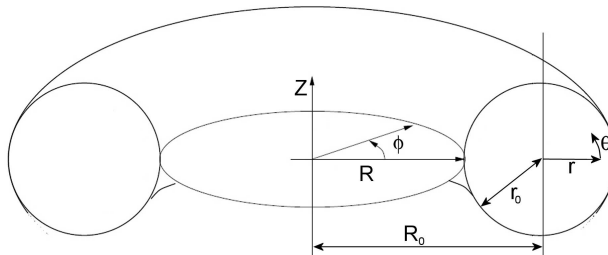


**Figure 1.4:** Coordinate system for a toroidal symmetry

The torus is defined by its major radius  $R$  and its minor radius  $r_0$ . The points inside this system are described by the distance from the vessel axis given by the radius  $r$  as well as their toroidal position determined by the angle  $\phi$ . The poloidal component is defined by the angle  $\theta$ .

However, electrical fields  $\vec{E}$  arise due to charge separation resulting from a radial inhomogeneous magnetic field in the torus, which decays with  $1/R$ . These fields lead to  $\vec{E} \times \vec{B}$  force, whose derivation is shortly explained in section 2.1. This force causes a radial transport of the particles to the low field side destroying the confinement [Wag07]. In order to compensate these particle movements a poloidal magnetic field component is overlaid which leads to a twisting of field lines. The grade of the twisting is characterized by the rotational transform  $\iota$ . Tracing a magnetic field line a change of  $\theta$  occurs by varying  $\phi$ . If this field line is considered after one toroidal cycle of  $\Delta\phi = 2\pi$  the poloidal change of  $\Delta\theta$  defines the normalized rotational transform

$$t = \frac{\Delta\theta}{2\pi} . \quad (1.10)$$

The inverse  $t$  is called safety factor  $q$ . If  $t$  is different from a rational value the field line will not close after an infinite number of circles. In this case the field line spans magnetic flux surfaces whose radial content is limited through a material limiter inside the torus or by the magnetic field configuration. The mobility of the particles along this flux surface in parallel direction is much faster compared to the perpendicular direction resulting in a constant density and temperature on a flux surface.

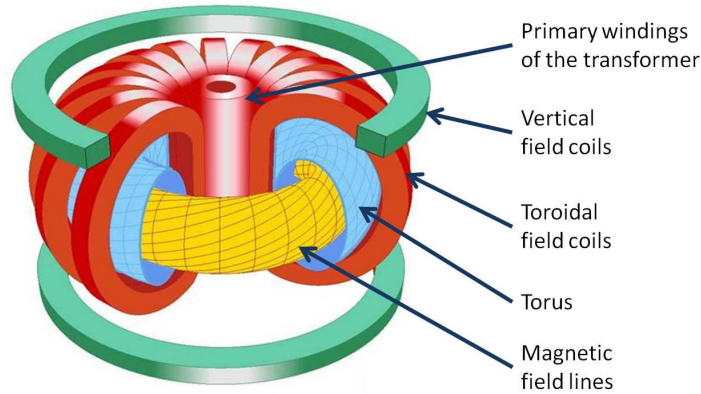


**Figure 1.5:** Schematic setup of a tokamak

For the generation of a confining magnetic field, basically two experimental concepts exist. In case of tokamak experiments, whose configuration is shown in figure 1.5, the necessary poloidal magnetic field causing the rotational transform is generated by a toroidal plasma current. Here, various ways to drive plasma current exist. Initially this current was mainly generated by means of a transformer using the plasma as secondary winding. With further development of this concept - since the 1950's - new concepts of current drive, which are also topic of this work and therefore presented in section 2.4, have been developed. Non-inductive current drive is of general interest for tokamak operation where the pulse length is classically limited by the transformer capability.

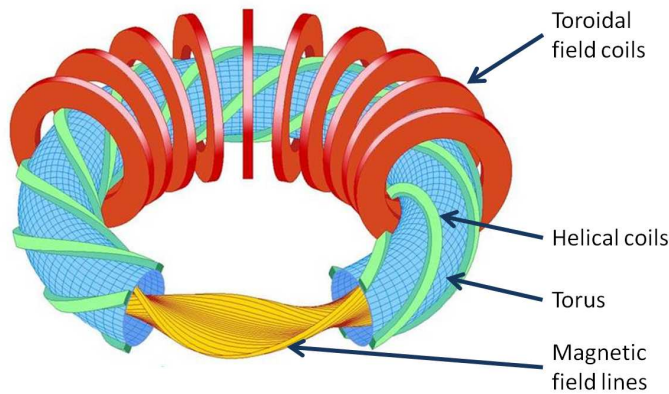


**Figure 1.6:** Schematic setup of a classical stellarator

A second opportunity to create a poloidal field component is based on the use of additional magnetic field coils. This kind of experiments is declared as stellarators, where also different classifications on the basis of the used coils exist. In case of a classical stellarator, shown in figure 1.6, the toroidal field is generated analog to tokamaks by means of toroidal field coils.

The poloidal field is caused by helical coils. This leads to a three dimensional magnetic field geometry causing further transport phenomena. With respect thereof further improvements in the magnetic field coils have been developed leading to a concept of modular coils which may result in confinement behavior similar to same sized tokamak experiments. This concept will be realized with the experiment Wendelstein 7-X (W7-X) which is currently under construction.

## 1.3 The WEGA Stellarator

The WEGA experiment (**W**endelstein **E**xperiment in **G**reifswald für die **A**usbildung) was originally built up in Grenoble, France in 1975. It was developed as a hybrid experiment allowing tokamak as well as stellarator scenarios with an exploratory focus on heating with lower hybrid waves [BHI<sup>+</sup>77]. Initially started as tokamak experiment, WEGA was mostly used as a stellarator after the late 70's. From 1983 to 2000 research on WEGA has been performed at the Institut für Plasmaforschung (IPF) in Stuttgart, Germany. In 2001 WEGA has been reassembled at the Max-Planck-Institut für Plasmaphysik (IPP) in Greifswald, Germany. Here, it is used for training and education of physicists, basic plasma research and as a test bed for W7-X components. Especially the control and data acquisition system is tested at WEGA to guarantee a faultless and fast implementation at W7-X later.

### 1.3.1 Setup

The magnetic field coil system of WEGA consists of 40 toroidal field and 4 helical coils. The helical coils lead to a twofold poloidal ( $l=2$ ) and a fivefold toroidal ( $m=5$ ) symmetry. The coils made of copper are water cooled. Thus, the cooling of the coils determines factor the run time of experiments. At a magnetic field of 0.5 T, experiments can be performed with a duration of around 30 seconds, whereas at 0.05 T steady state operation of the coil system is possible. The non-cooled vertical field coils are used for a radial shift of the plasma inside the vessel and to control the shear which describes the radial variation of  $\iota$ .  $\iota$  can be varied by adjusting the helical field coil current  $I_{HF}$  with respect to the toroidal field coil current  $I_{TF}$ . The major radius  $R$  of WEGA is 0.72 m and the inner radius  $r$  of the vessel is 0.19 m. Discharges can be performed with a plasma radius  $a$  up to 11 cm.

Furthermore, a transformer with 64 primary windings can be used for inductive current drive and therefore gives access of  $\iota$  variations. The inductively driven current is limited by the finite flux generation in the transformer core. Saturation is reached at 440 mVs. With respect to the other possible heating methods at WEGA, described in the next section, ohmic heating plays a minor role. At WEGA different working gases can be used. It is possible to investigate argon, neon, helium, deuterium and hydrogen discharges. In this work only argon and helium discharges have been examined.

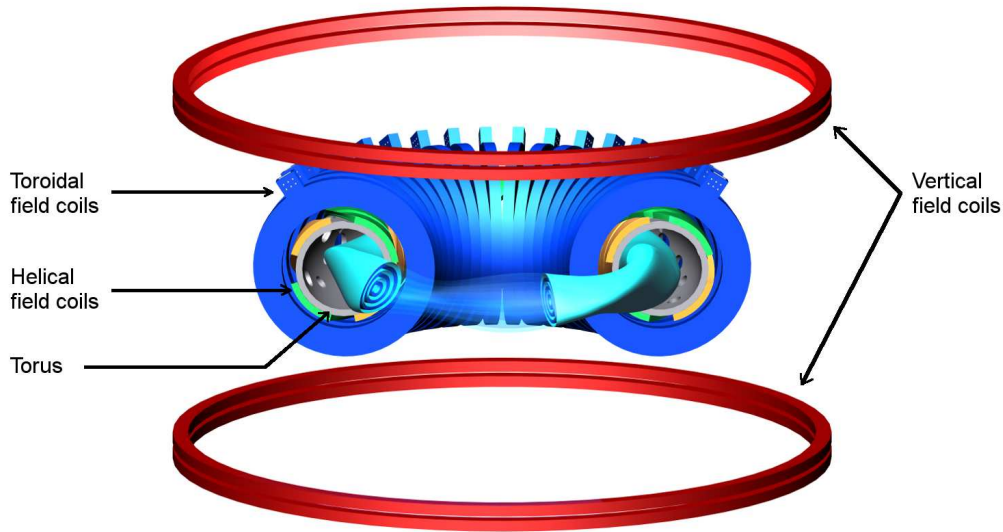


*Figure 1.7: Schematic diagram of the WEGA stellarator and the flux surfaces*

### 1.3.2 Plasma heating

At WEGA plasma ignition and heating is realized by means of microwaves. On the one hand a gyrotron with a power of 10 kW and an emission frequency of 28 GHz is available. On the other hand two magnetrons with 20 kW and 6 kW at a frequency of 2.45 GHz can be used. The energy transfer into charged plasma particles is possible by means of wave damping processes. Here, one has to distinguish between cyclotron damping and Landau damping. The first is valid for particles which have a cyclotron frequency close to the emission frequency of the microwave. Considering electrons as the preferred heating particles the resonant heating waves of 28 GHz and 2.45 GHz require a magnetic field of 1.0 and 0.0875 Tesla, respectively. In this case electrons are referred to as resonant electrons. Thus the heating method is called electron cyclotron resonant heating (ECRH). The resonantly heated electrons release their energy and heat the bulk plasma by means of collisions with other particles. However, for the first case of utilizing the 28 GHz microwave a magnetic field of 0.5 T is used at WEGA due to technical limitations described below. The same heating process is also possible for ions (ICRH) by applying a frequency corresponding to the cyclotron frequency of the ions which is in the range of 5 to 50 MHz. However, this heating method is not available at WEGA yet.

The later shown discharges have been realized at 0.5 T. The standard heating scenario at this magnetic field is the so called X2-mode heating with the 28 GHz system. Here, an extra-ordinary wave (X-wave), defined by its electrical vector pointing perpendicular to the external magnetic field, is irradiated into the plasma. In order to get a high absorption the irradiation angle should be perpendicular to the external magnetic field [EG94]. Furthermore, it is possible to change this angle by means of a movable mirror system mounted inside the torus and controlled from the outside. The mirror system is shown in figure 1.8.

The number '2' in X2-heating states that the emitted wave corresponds to the second harmonic cyclotron frequency of the electrons. For X1 heating a magnetic field of 1 T would be necessary. However, WEGA's power supply is not licensed for 1 T experiments yet.

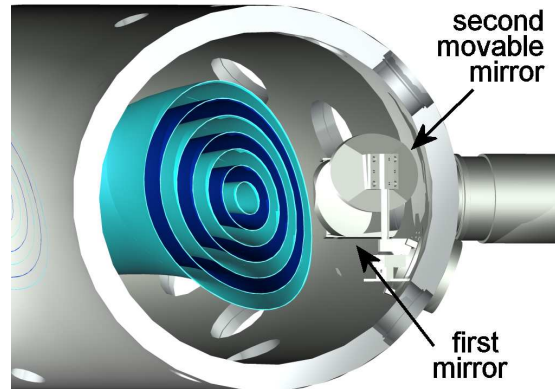


*Figure 1.8: Movable mirror system at WEGA for changing the heating scenario*

A further opportunity for transferring energy into the WEGA plasma makes use of electrostatic Bernstein waves induced by electromagnetic waves. Here, the microwave is launched in O-mode polarization, defined by an electric vector parallel to the external magnetic field, under an oblique angle of  $55^\circ$ . In a two-step conversion the O-wave is converted into a slow X-wave and later into an electrostatic Bernstein wave [LMM<sup>+</sup>03]. This process, which is referred to as OXB mode conversion, could be realized at WEGA for the 28 GHz resonant heating with argon and helium since a critical density of  $n_e = 0.97 \cdot 10^{19} m^{-3}$  required for the mode conversion can be reached. The magnetic field for OXB heating has to be reduced due to Doppler down shift to 0.460...0.480 T. In Hydrogen it was not possible to achieve this density and therefore this heating method yet. Consequently the highest plasma densities can be realized in argon and helium at WEGA since by using this heating scenario the Bernstein waves may propagate into the plasma without an upper density cut-off limit. For resonant 2.45 GHz heating this is the default heating scenario at WEGA. It has been found that the best absorption occurs at a reduced magnetic field of 50...60 mT [Hor04, Pod06]. At a magnetic field of 0.5 T electron densities of  $1 \cdot 10^{18}$ ... $1.5 \cdot 10^{19}$  and electron temperatures of 5...50 eV can be reached at WEGA.

### 1.3.3 Diagnostics

At WEGA various diagnostics are available. A overview of the diagnostics is presented in figure 1.9. For line integrated density measurements a one-channel Mach-Zehnder interferometer is used. Langmuir probes are also available for localized density measurements as well as for temperature measurements. Here, several manipulators with single Langmuir probes and probe arrays can be used.



However, the use of the probes is limited in case of high plasma temperature leading to thermal destruction or perturbation by the penetrating probes. Additionally an electron cyclotron emission (ECE) and a soft X-Ray diagnostic are located at WEGA which give access to the electron temperature and the energy spectrum of super thermal particles, respectively. A fast 16-channel AXUV diode array with a resolution of below  $30 \mu\text{s}$  can be used to determine the temporal evolution of radiation profiles. Furthermore, a gold foil bolometer measures the total emitted power [Gla10]. A supersonic helium beam diagnostic was setup which allows the determination of the temperature and density profiles in conjunction with a collisional radiative model [Mül10].

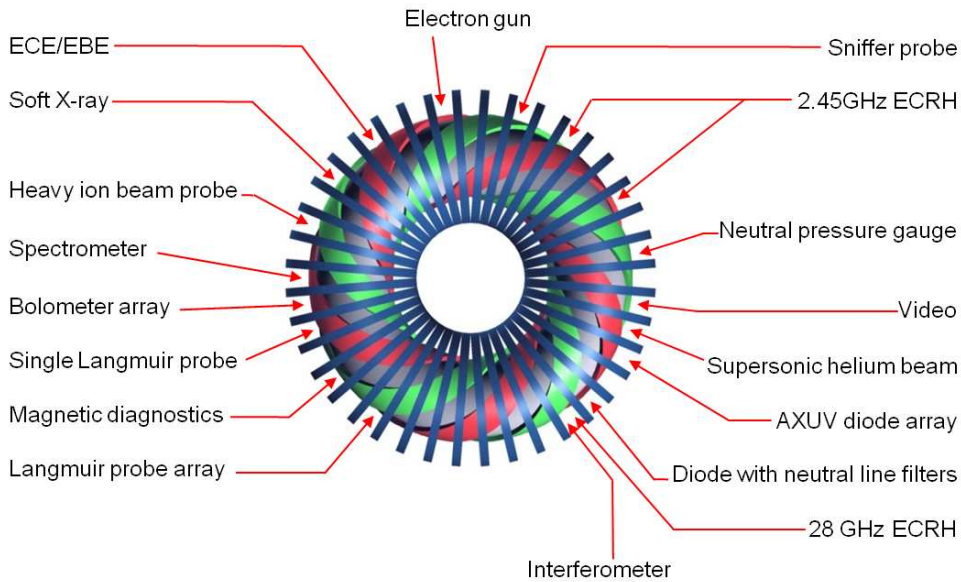


**Figure 1.9:** Overview of diagnostics at the WEGA stellarator

## 2 Fundamentals of Plasma Current and Pressure in Fusion Devices

Investigations of the plasma confinement need information about the plasma energy and the normalized plasma pressure  $\beta$ . By means of the diamagnetic effect in plasmas it is possible to determine these quantities using magnetic diagnostics. The theory and impact of the diamagnetic effect is shown in section 2.1 and 2.2.

In order to control magnetically confined plasmas, knowledge about the plasma current is of essential importance. The theory of current drive in plasmas is described in section 2.3 and 2.4. In order to compare the different concepts the current drive efficiency is introduced in 2.4.1. By additional use of the Spitzer resistivity, explained in section 2.5, access to an average electron temperature is given.

### 2.1 Diamagnetism in Plasmas

Due to the directed particle movement, diamagnetism as well as paramagnetism can occur in plasmas. However, the latter plays a less significant role. Therefore, cases of paramagnetism are explained at the end of this section. Plasma diamagnetism represents a reduction of externally created magnetic field inside the plasma compared to the case where no plasma exists. The derivation of a magnetic field which opposes the external field can be realized for the single particle description as well as within the fluid theory. The second case is presented here. In order to create the internal opposing magnetic field, a current with a certain direction inside the plasma is needed. This current is referred to as diamagnetic current. The point of origin for the derivation is the fluid equation of motion for the charged particle species  $k$ .

$$m_k n_k \left( \frac{\partial \vec{v}_k}{\partial t} + (\vec{v}_k \cdot \vec{\nabla}) \vec{v}_k \right) = \underbrace{q_k n_k (\vec{E} + \vec{v}_k \times \vec{B})}_1 - \underbrace{\vec{\nabla} p_k}_2 - \underbrace{\vec{\nabla} \cdot \vec{\pi}_k}_3 + \underbrace{m_k n_k \vec{g}}_4 + \underbrace{\vec{P}_{ei,ie}}_5 \quad (2.1)$$

The whole derivation of this formula can be seen in [Che74]. The term on the left hand side is the convective deviation describing the motion of the fluid element. The first term on the right hand side of equation (2.1) results from the interaction of the fluid with an electric or magnetic field, analog to equation (1.3). Term 2 and 3 exist due to the stress tensor, which has to be introduced since a momentum transfer takes place between the particles and the fluid element. In the simplest case the tensor can be separated into a pressure term and a viscosity term. Term 4 represents the influence of the gravitation force which is neglected in most cases since its small value compared to term 1. But for an ideal consideration this term also has to be taken into account. The resistivity reveals the momentum loss or gain due to collisions between electron and ion fluid elements or vice versa. Considering the plasma as a single fluid the resistivity term 5 for electrons and ions will cancel each other out

$$P_{e,i} = -P_{i,e} \quad (2.2)$$

since the loss of one fluid element is the gain of the other one, which are part of a common fluid element now.

As shown later, only the perpendicular fluid motion  $v_{\perp,k}$  with respect to the direction of the magnetic field lines makes a contribution to diamagnetism. Therefore, only this velocity component is of interest for the derivation. For time scales which are large compared to the gyration frequency, the time dependent part on the left hand side of equation (2.1) can be set to (0). The result will show later, neglecting of the full convective term will also be justified in the case that  $E = 0$  or  $\vec{E}$  is in the opposite direction to  $\vec{\nabla}p$ . Taking all these approximations into account, equation (2.1) multiplied by  $\times \vec{B}$  can be rewritten as

$$0 = q_k n_k \left( \vec{E} \times \vec{B} + \left( \vec{v}_{\perp,k} \times \vec{B} \right) \times \vec{B} \right) - \vec{\nabla} p_k \times \vec{B} \quad (2.3)$$

Rearranging this equation for the perpendicular velocity, the outcome is

$$\vec{v}_{\perp,k} = -\frac{\vec{\nabla} p_k \times \vec{B}}{q_k n_k B^2} + \frac{\vec{E} \times \vec{B}}{B^2} \quad (2.4)$$

The first terms represents the diamagnetic drift and the second the  $\vec{E} \times \vec{B}$  drift, which does not depend on charge and density. To get the total diamagnetic current density, ions and electrons will be considered at the same time. For this case, the general result is

$$\begin{aligned} \vec{j}_{Dia} &= \sum_k q_k n_k \vec{v}_{Dia,k} \\ &= \frac{\vec{B} \times \vec{\nabla} p}{B^2} \quad (2.5) \end{aligned}$$

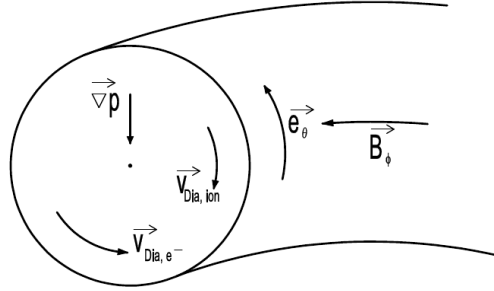


**Figure 2.1:** Diamagnetic particle drift leads to a current perpendicular to the magnetic field and pressure

Using the equation of state

$$p = C\rho^\gamma = C(mn)^\gamma, \quad (2.6)$$

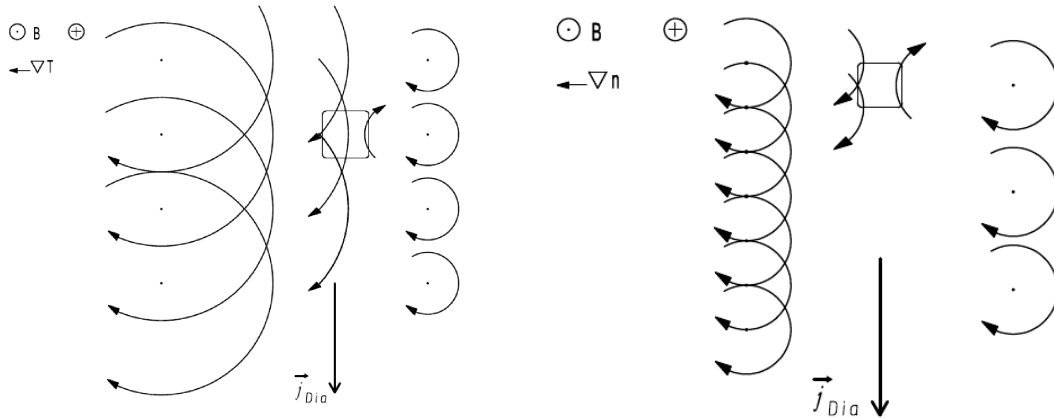
where  $C$  is a constant and  $\gamma$  the ratio of specific heats  $C_p(T)/C_V(T)$ , the diamagnetic current density can be associated with the gradient in density and temperature in the plasma. For the special case of singly charged ions and isothermal compression ( $\gamma = 1$ ), the diamagnetic current is

$$\vec{j}_{Dia} = k_B (T_e + T_i) \frac{\vec{B} \times \vec{\nabla}n}{B^2} \quad (2.7)$$

where  $\vec{\nabla}n$  represents the density gradient for ions and electrons, respectively. Therefore, the diamagnetic current always flows perpendicularly to a pressure gradient and the ambient magnetic field. Thus, the magnetic field created by the diamagnetic current  $B_{dia}$  opposes the external magnetic field created by the field coils. Consequently, under stationary conditions the Lorentz force resulting from  $\vec{j}_{Dia} \times \vec{B}$  will balance the opposite force arising from the pressure gradient.

The outcome of the description of diamagnetism in the single particle model is that the opposing magnetic field will be determined on the one hand through the gyration of particles and on the other hand through the current resulting from the  $\nabla B$ - and the curvature drift of the particles [WC87].

Equation (2.5) can be understood by means of figure 2.2(a), where a temperature gradient leads to a gradient in the gyration velocity causing a change of the Larmor radius at a constant magnetic field. Therefore, a net current density flows perpendicularly to the temperature gradient. On the other hand, a current density can also exist due to a gradient in density, as shown in figure 2.2(b) Here, the different numbers of particles gyrating perpendicular to  $\vec{\nabla}n$  leading to a current in the direction of  $\vec{B} \times \vec{\nabla}n$ . Now the thermal energy of the plasma can be derived by the impact of the diamagnetic current. However, the diamagnetic effect is not the only process leading to a change in the magnetic field. Therefore, a theoretical investigation of contributions from different effects will be presented in the following.



(a) Change of gyration velocity at a constant temperature gradient (b) Density gradient leading to net current in perpendicular direction

**Figure 2.2:** Resultant diamagnetic current in the single particle model due to temperature gradient (a) and density gradient (b)

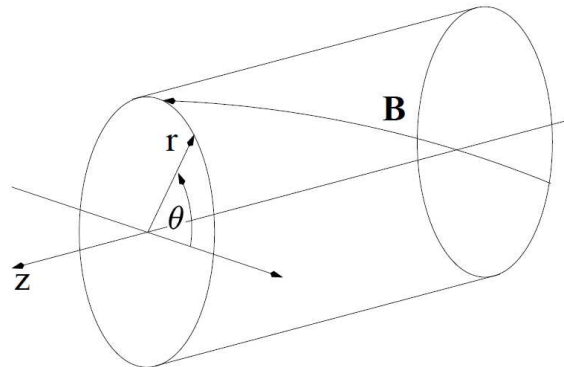


**Figure 2.3:** Coordinate system used for screw pinch symmetry

Due to the three dimensional geometry of stellarators it is not possible to solve the equation for diamagnetic effects and the related plasma energy analytically. Only numerical codes (e.g. NEMEC) offer the chance to get qualitative results for these experiments [HRM86]. Nevertheless, in first order it is possible to solve the equations for a screw pinch, assuming a toroidal ( $\phi \rightarrow z$ ) and poloidal symmetry. Figure 2.3 depicts the transformation from stellarator topology to the cylindrical coordinate system.

The poloidal component is denoted as  $\theta$  in both systems. The magnetic field for a screw pinch is given by

$$\vec{B}(r) = B_\theta(r)\vec{e}_\theta + B_z(r)\vec{e}_z \quad . \quad (2.8)$$

Especially for experiments with a large aspect ratio, given by

$$A = \frac{R}{a} \quad , \quad (2.9)$$

where  $R$  is the major radius of the torus and  $a$  is the plasma radius, equation (2.8) is a good approximation. The total flux reduction measured by a magnetic loop is

$$\Delta\Phi = \Phi - \Phi_0 = 2\pi \int_0^b B_z r \, dr - \pi b^2 B_{0z} \quad (2.10)$$

where  $b$  is the radius of a diamagnetic loop, described in chapter 3.1.2, and  $B_{0z}$  is the vacuum magnetic field in  $z$ -direction. Now Ampere's law is taken into account in the differential form with

$$\vec{\nabla} \times \vec{B} = \mu_0 \vec{j} \quad . \quad (2.11)$$

For the screw pinch field this can be rewritten as

$$\mu_0 j_\theta = -\frac{\partial B_z}{\partial r} \quad (2.12)$$

$$\mu_0 j_z = \frac{1}{r} \frac{\partial(r B_\theta)}{\partial r} \quad . \quad (2.13)$$

As a consequence the first part of equation (2.10) yields

$$\begin{aligned} \int_0^b B_z r \, dr &= \frac{1}{2} [r^2 B]_0^b - \frac{1}{2} \int_0^b \frac{\partial B_z}{\partial r} r^2 \, dr \\ &= \frac{b^2 B_z(b)}{2} + \frac{\mu_0}{2} \int_0^b j_\theta r^2 \, dr \\ &= \frac{b^2 B_z(b)}{2} + \frac{\mu_0}{2} \int_0^a j_\theta r^2 \, dr \end{aligned} \quad (2.14)$$

since the poloidal current density is  $j_\theta(r > a) = 0$  outside the plasma determined by the plasma radius  $a$ . Hence, the flux change is

$$\Delta\Phi = \pi b^2 (B_z(b) - B_{0z}) + \pi \mu_0 \int_0^a j_\theta r^2 \, dr \quad . \quad (2.15)$$

For the next step, the radial component of the force balance equation which is generally given by

$$\vec{\nabla} p = \left( \vec{j} \times \vec{B} \right) \vec{e}_r \quad , \quad (2.16)$$

is used to determine the current density in  $\theta$ -direction

$$j_\theta = \frac{1}{B_z} \frac{dp}{dr} + j_z \frac{B_\theta}{B_z} \quad . \quad (2.17)$$

Hence, the reduction of the flux is given by

$$\Delta\Phi = \underbrace{\pi b^2 (B_z(b) - B_{0z})}_1 + \underbrace{\pi\mu_0 \int_0^a \frac{r^2}{B_z} \frac{dp}{dr} dr}_2 + \underbrace{\pi\mu_0 \int_0^a j_z \frac{r^2 B_\theta}{B_z} dr}_3 \quad . \quad (2.18)$$

Here, the first term describes the reduction of the vacuum magnetic flux for  $r > a$ . In a screw pinch this term is (0), since the vacuum axial (toroidal) magnetic field is constant  $B_z = B_{z0}$  for this geometry. Of course, in magnetic confinement devices this term is nonzero. Thus, different methods in determining  $B_z(b)$  and  $B_{0z}$  are presented in chapter 3.2, which are used in order to get the flux change. The second term is partially integrated so that the result is

$$\begin{aligned} \pi\mu_0 \int_0^a \frac{r^2}{B_z} \frac{dp}{dr} dr &= \frac{\pi\mu_0}{B_z} [r^2 p]_0^a - \frac{2\pi\mu_0}{B_z} \int_0^a r p dr \\ &= -\frac{2\pi\mu_0}{B_z} \int_0^a r p dr \quad . \end{aligned} \quad (2.19)$$

The pressure at  $a$  is defined as zero here. For the poloidal field in term 3 of equation (2.18) different contributions have to be considered - on the one hand the vacuum field and on the other hand the field due to the plasma current

$$B_\theta = B_{\theta, I_z} + B_{\theta, vac} \quad . \quad (2.20)$$

The intermediary result is

$$\Delta\Phi = \underbrace{-\frac{2\pi\mu_0}{B_z} \int_0^a r p dr}_a + \underbrace{\frac{\pi\mu_0}{B_z} \int_0^a j_z r^2 B_{\theta, I_z} dr}_b + \underbrace{\frac{\pi\mu_0}{B_z} \int_0^a j_z r^2 B_{\theta, vac} dr}_c \quad . \quad (2.21)$$

It is obvious that the first term on the right hand side of equation (2.21) decreases the flux, whereas the next two terms increase the flux. In the case of circular flux surfaces, the term b of equation (2.21) can further be simplified by the means of Ampere's law

$$\oint_C \vec{B} \cdot d\vec{l} = \mu_0 I \quad (2.22)$$

where  $C$  is a closed loop around the area carrying the current

$$I(r) = 2\pi \int_0^r j(r') r' dr' \quad . \quad (2.23)$$

Hence, the magnetic field due to the toroidal plasma current is determined by

$$B_{\theta, I_z}(r) = \frac{\mu_0 I_z(r)}{2\pi r} \quad . \quad (2.24)$$

In combination with

$$j_z(r) = \frac{1}{2\pi r} \frac{dI_z(r)}{dr} \quad (2.25)$$

the second term denoted by  $b$  in equation (2.21) yields

$$\begin{aligned} \frac{\pi\mu_0}{B_z} \int_0^a j_z r^2 B_{\theta, I_z} dr &= \frac{\mu_0^2}{2B_z} \int_0^a j_z r I_z(r) dr \\ &= \frac{\mu_0^2}{4\pi B_z} \int_0^a \frac{dI_z}{dr} I_z dr \\ &= \frac{\mu_0^2 I_z^2(a)}{8\pi B_z} . \end{aligned} \quad (2.26)$$

Thus, by using the total plasma current with

$$I_{pl} = 2\pi \int_0^a j_z r dr = I_z(a) \quad (2.27)$$

the result is

$$\Delta\Phi = -\frac{2\pi\mu_0}{B_z} \int_0^a r p dr + \frac{\mu_0^2 I_{pl}^2}{8\pi B_z} + \frac{\pi\mu_0}{B_z} \int_0^a j_z r^2 B_{\theta, vac} dr \quad . \quad (2.28)$$

Now the plasma energy  $W$  is taken into account additionally. For a toroidal symmetry ( $z \rightarrow \phi$ )  $W$  can be written as

$$\begin{aligned} W &= \frac{3}{2} \int_V p d^3r = \frac{3}{2} \langle p \rangle V \\ &= \frac{3}{2} \int_{r=0}^a \int_{\theta=0}^{2\pi} \int_{\phi=0}^{2\pi} p r (r \cos(\phi) + R) d\phi d\theta dr \\ &= 6\pi^2 R \int_0^a r p dr \quad . \end{aligned} \quad (2.29)$$

Together with the rotational transformation given by

$$\iota_{vac} = \frac{R}{r} \frac{B_{\theta, vac}(r)}{B_{\phi, vac}} \approx \frac{R}{r} \frac{B_{\theta, vac}(r)}{B_\phi} \quad (2.30)$$

where  $B_\phi$  corresponds to  $B_z$  now, the flux change is

$$\Delta\Phi = -\frac{\mu_0 W}{3\pi B_\phi R} + \frac{\mu_0^2 I_{pl}^2}{8\pi B_\phi} + \frac{\pi\mu_0 \iota_{vac}}{R} \int_0^a j_\phi r^3 dr \quad . \quad (2.31)$$

The first term on the right hand side contributes to plasma diamagnetism whereas the other terms result in paramagnetism. Plasma paramagnetism can be reached by high plasma currents as well as peaked current density profiles if the plasma energy is low at the same time.



In order to evaluate the last term in equation (2.31), current profiles have to be assumed. Differently peaked current profiles can be described by

$$j_\phi(r) = j_0 \left(1 - \left(\frac{r}{a}\right)^2\right)^m \quad (2.32)$$

with a stronger peaking for larger components  $m$ . Therefore, the last integral can be modeled with

$$\int_0^a j_\phi r^3 dr = \frac{a^4 j_0}{2(m+1)(m+2)} \quad (2.33)$$

$$= \frac{I_{pl} a^2}{2\pi(m+2)} \quad (2.34)$$

Finally, by having knowledge of the flux change, the plasma current and the current profile, the plasma energy as well as the average plasma pressure can be calculated by means of equation (2.29) and (2.31). Now, the challenge is to measure  $\Delta\Phi$ . Different concepts are presented in section 3.1.2.

## 2.2 Plasma Pressure and $\beta$

The local pressure is generally defined by

$$p = nk_B T \quad (2.35)$$

with the particle density  $n$  and the thermal particle energy  $k_B T$ . In case of a system containing species with different temperatures  $T_j$ , the total pressure is given by the sum of the single pressures.

$$p = \sum_j p_j = \sum_j n_j k_B T_j \quad (2.36)$$

Now, the force balance equation (2.16), which could be derived by means of the fluid equation of motion (2.1), and Ampere's law (2.22) are combined and lead to

$$\vec{\nabla} \left( p + \frac{B^2}{2\mu_0} \right) = \frac{1}{\mu_0} (\vec{B} \cdot \nabla) \vec{B} \quad (2.37)$$

Using the screw pinch symmetry introduced previously the term on the right of equation (2.38) turns to zero. However, in the general case the term does not vanish, but it becomes quite small compared to the term on the left of the equation above [Che74]. Therefore, the sum of particle pressure and the magnetic field pressure is assumed to be constant.

$$p + \frac{B^2}{2\mu_0} = \text{const} \quad (2.38)$$

The ratio of both terms on the left of equation (2.38) is defined as plasma  $\beta$

$$\beta = \frac{p}{B^2/2\mu_0} \quad (2.39)$$

In case of having an anisotropic plasma, beta needs to be defined for every symmetry component. Considering equation (2.38) it can be seen, that an increasing plasma particle pressure necessarily leads to a reduction of  $B^2$ . This is realized by the diamagnetic current and leads to an increase of the plasma beta, as seen in figure 2.4. This relationship between the plasma current and plasma pressure is one of the most fundamental correlations in plasma physics. Both parts depend on each other and guarantee the magnetic confinement. In addition to the determination of the plasma pressure by measuring the flux change and therefore the magnetic field change given by equation (2.31), it is also possible to estimate the electron pressure by using Langmuir probes. Here, the pressure is calculated from the local  $n_e$  and  $T_e$  measurements.

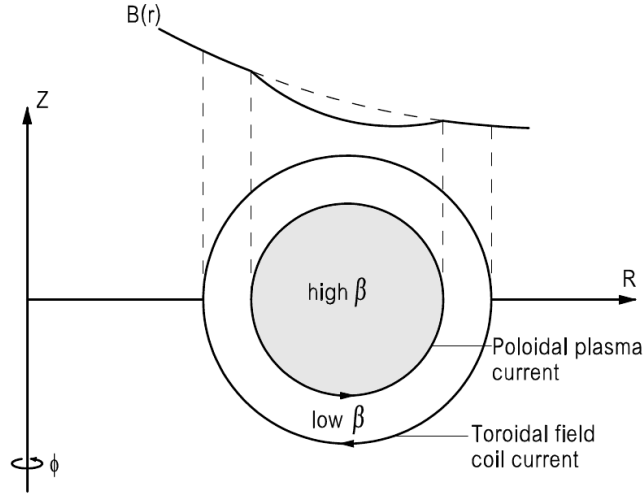


**Figure 2.4:** High plasma pressure leads to the increase of plasma beta and to a reduction of the inner magnetic field

Often also an averaged value of the plasma  $\beta$  is used with respect to equation (2.31).

$$\langle \beta \rangle = 2 \frac{\Delta\Phi}{\Phi} = \frac{2\mu_0 \langle p \rangle}{\langle B^2 \rangle} \quad (2.40)$$

Here,  $\Delta\Phi$  represents the measured flux change and  $\Phi$  the flux through the diamagnetic loop normalized to the plasma cross section.

## 2.3 Plasma Waves Relevant for Current Drive

In plasmas a wide variety of waves can exist. These are electrostatic, magnetic, electromagnetic and acoustic waves. The occurrence and the respective dispersion relation of the wave depend on the involved particle species and their density as well as the existence and the direction of ambient electric and magnetic fields compared to the propagation direction of the wave. These waves can propagate through the plasma, be absorbed, reflected and converted into other wave types according to the present plasma parameters.

Here, only the waves which are relevant for current drive experiments at WEGA will be introduced. Beside the electromagnetic electron cyclotron wave introduced in section 1.2.1, the Bernstein wave as well as the lower hybrid wave play a role for current drive in WEGA plasmas. An overview of all possible waves in plasmas is given in [Sti62].

### 2.3.1 Electron Cyclotron Wave

In a homogeneous magnetized plasma different modes of electromagnetic waves exist depending on their propagation and polarization direction with respect to the magnetic field. For electron cyclotron waves these modes differ in their interaction with the electrons. The electrical field vector oscillates at a frequency in the range of the electron cyclotron frequency  $\omega_{c,e}$ . Through the combination of the equation of motion for the electrons, the Maxwell equations, as well as a harmonic ansatz for the electric field, a dispersion relation in the form of

$$An^4 + Bn^2 + C = 0 \quad (2.41)$$

follows, which is called Appleton-Hartree-equation [Har07]. Ions are not considered here. For the investigation of possible solutions for the refraction index

$$n = \frac{c}{\omega}k \quad (2.42)$$

a differentiation between perpendicular and parallel propagation can be done. For parallel propagation ( $k \parallel B_0$ ) three possible solutions exist. These are the right (R) and the left (L) circular polarized electromagnetic waves as well as an electrostatic wave, which is called Landau oscillation. The interaction of electrons with the wave takes place in the form of resonances ( $n \rightarrow \infty$ ) at the electron cyclotron frequency or its harmonics and reflections ( $n \rightarrow 0$ ) at the so-called cut-off frequencies, which are defined by

$$\omega_L = \frac{1}{2} \left( -\omega_C + \sqrt{\omega_c^2 + 4\omega_p^2} \right) \quad (2.43)$$

$$\omega_R = \frac{1}{2} \left( +\omega_C + \sqrt{\omega_c^2 + 4\omega_p^2} \right) \quad (2.44)$$

The propagation of the L-wave is only possible above this frequency; however, the R-wave can also propagate underneath this limit.

For perpendicular propagation ( $k \perp B_0$ ) two modes exist in case of the cold plasma approximation. These are the ordinary (O) wave whose electrical field vector is polarized parallel with respect to the magnetic field and the perpendicular polarized extraordinary (X) wave [Sti62]. The O-mode behaves like a wave in a non-magnetized plasma so that a reflection occurs for frequencies below the plasma frequency

$$w_{p,k} = \left( \frac{Z_k^2 |q^2| n_k}{m_k} \right)^{1/2} . \quad (2.45)$$

For the X-mode the equivalent reflection occurs at the so-called upper X-cutoff frequency, which equals  $\omega_R$  and is therefore higher than the plasma frequency. Above this frequency, only the so-called fast-X-wave with a phase velocity above the speed of light can propagate. Additionally, there exists a frequency range below the upper X-cutoff where the so-called slow-X-wave can propagate. However, this wave propagation is limited by the lower X-cut-off frequency, which equals  $\omega_L$ , and the upper hybrid-resonance frequency  $\omega_{UH}$

$$w_{UH} = (w_{c:e}^2 + \omega_{p:e}^2)^{1/2} . \quad (2.46)$$

### 2.3.2 Electron Bernstein Wave

If a finite temperature of the plasma is considered, a third electrostatic electron cyclotron mode, the so-called Electron-Bernstein-wave (EBW) occurs additionally. This mode is based on a coherent movement of the electrons along the magnetic field lines which leads to a charge separation perpendicular to the field lines and therefore to a longitudinal electric field with respect to the propagation direction [LEH<sup>+</sup>97]. The additional conditions which lead to the dispersion relation of the EBW are a finite electron temperature causing a finite electron thermal velocity and finite Larmor radius. Another boundary condition is the achievement of a lower density limit for EBWs. In this way the local cyclotron frequency is higher than the upper hybrid frequency. Regarding the propagation of EBWs no upper density limit exists making over-dense plasma heating possible [LMV<sup>+</sup>03].

### 2.3.3 Lower Hybrid Wave

With respect to current drive by means of lower hybrid waves described in chapter 2.4.4, this chapter will shortly explain the origin of lower hybrid waves, their accessibility and therefore the chosen wave parameters. First of all the conventional lower hybrid wave represents an electrostatic ion wave, defined through an interaction of the electron and ion movement, where a propagation direction perpendicular to an outer magnetic field is considered. The dispersion relation is well known with a

resonance at the lower hybrid frequency

$$w_{LH} = \left( \frac{1}{w_{c;e}\omega_{c;i}} + \frac{1}{\omega_{p;i}^2} \right)^{-1/2}. \quad (2.47)$$

For low density the second term in equation (2.47) dominates. The whole derivation can be found in [Sti62].

Originally the use of lower hybrid waves has been proposed for ion heating. However, it has been shown that this kind of plasma heating is problematic [WC87]. Nevertheless, it was found that waves in the lower hybrid regime

$$w_{c;i} < w < w_{c;e} \quad (2.48)$$

can be used to drive substantial plasma currents up to almost the total plasma current for a successful tokamak operation [Glt99].

Now the dispersion relation will be solved for the general case with a wave frequency in the range  $\omega_{LH}$  as well as an existing parallel wave number leading to a finite  $n_{\parallel}$ . In this case the electric field of the wave is a combination of ordinary and extraordinary components, where the  $E_{\parallel}$  part is responsible for the later Landau damping leading to the acceleration of electrons. The solution of the dispersion relation can be expressed as

$$n_{\perp}^2 = -\frac{K_{\parallel}}{2K_{\perp}} \left( n_{\parallel}^2 - K_{\perp} + \frac{K_A^2}{K_{\perp}} \pm \left[ \left( n_{\parallel}^2 - K_{\perp} + \frac{K_A^2}{K_{\perp}} \right)^2 + \frac{4K_{\perp}K_A^2}{K_{\parallel}} \right]^{1/2} \right), \quad (2.49)$$

with

$$K_A = \frac{\omega_{p;e}^2}{\omega\omega_{c;e}} \quad (2.50)$$

$$K_{\perp} = 1 + \frac{\omega_{p;e}^2}{\omega_{c;e}^2} - \frac{\omega_{p;i}^2}{\omega^2} \quad (2.51)$$

$$K_{\parallel} = -\frac{\omega_{p;e}^2}{\omega^2}. \quad (2.52)$$

as components of the dielectric tensor [Fre08]. Thus, two solutions are possible - the slow lower hybrid wave, often only called “lower hybrid wave”, and a fast lower hybrid wave. In order to suppress an evanescent region  $n_{\perp}$  has to be greater than zero which equals  $K_{\perp} > 0$ . This is the lower boundary condition of the chosen wave frequency and can be expressed as  $\omega^2 > \omega_{LH}^2$ . Furthermore, in order to eliminate a mode conversion to the fast wave, which will be reflected to the plasma edge and does not reach the desired region,  $n_{\parallel}$  needs to be greater than a critical boundary condition defined by

$$n_{\parallel}^2 > \left[ K_{\perp}^{1/2} \left( -\frac{K_A}{K_{\parallel}} \right)^{1/2} \right]^2 \quad (2.53)$$

In order to get an efficient current drive,  $n_{\parallel}$  should not be too large [Fre08]. It is chosen slightly larger than the critical value in equation (2.53). Due to the fact that the parallel refraction index has to be  $n_{\parallel} > 1$  for the wave propagation,  $n_{\perp}^2$  is negative for the plasma edge since the density is low here. In order to avoid reflections in this low density region the launching antenna has to be positioned as close as possible to the plasma.

### 2.3.4 Doppler shift

A necessary condition for the positioning of a launching antenna with respect to current drive is the incident angle  $\phi$  of the launched wave with respect to the magnetic field lines. This affects the propagation direction of the wave types in a plasma explained before. In the case of an oblique propagating wave, electrons, which are moving towards the wave, observe an increased frequency. On the other hand, electrons, which are moving with the wave, experience a reduced frequency [Har07]. The amount of this Doppler shift results from the resonance condition, defined by equation (2.60), and does generally depend on the parallel velocity of the particles and the parallel component of the refractive index

$$\Delta\omega = \omega n_{\parallel} \frac{v_{\parallel}}{c} \quad . \quad (2.54)$$

In the special case of a non-refracted electromagnetic cyclotron wave, the parallel refraction index at the resonance can be simplified to

$$n_{\parallel} = \cos\phi \quad . \quad (2.55)$$

## 2.4 Plasma Currents in Toroidal Magnetic Confinement

Plasma currents play a crucial role in magnetic confinement experiments. On the one hand side in tokamak experiments a well defined plasma current is needed as it is indispensable for the magnetic confining field. On the other hand in stellarator experiments a compensation of plasma currents is desired as they provide a source of free energy, which may lead to instabilities, and change the vacuum magnetic field configuration. Therefore, different opportunities to generate currents independent of their use are presented in the next sections.

Besides the inductive current drive by use of a transformer described in section 2.4.2 it is also possible to drive a current in a plasma by means of wave-particle interaction, where different concepts exist. At WEGA it is possible to radiate a wave with a wave number component in magnetic field direction which is referred to as lower hybrid wave. Due to Landau damping the wave can transfer energy and momentum to plasma particles leading to a current (explained in chapter 2.4.4).

Additionally by resonant absorption of a launched wave a current can be driven in the plasma. A similar process can be realized by use of electron Bernstein waves at WEGA. These processes are described in section 2.4.3 and 2.4.5.

It is also feasible to use other waves to drive current in fusion experiments. An overview for wave driven plasma currents is given in [Fis87, WC87]. Furthermore, internal plasma currents can occur e.g. due to pressure gradients and neoclassical effects in toroidal devices. These currents are described in section 2.4.6 and 2.4.7.

Another opportunity to drive plasma currents is neutral beam injection (NBI). However, it should be mentioned that NBI is mainly used for plasma heating. Only a reference for further literature should be given here since current drive by NBI is not available at WEGA [Fis87, Hir80, OKAIa+01].

### 2.4.1 Plasma Current Drive Efficiency

In order to qualitatively compare the different current drive concepts, a current drive efficiency has to be introduced. This efficiency is defined by

$$\eta = \frac{I_{CD}}{P_{CD}} \quad , \quad (2.56)$$

the ratio of the driven current  $I_{CD}$  and its auxiliary power  $P_{CD}$ . In case of plasma currents caused by radiation of microwaves, it is possible to describe equation (2.56) in terms of plasma parameters

$$\eta = 0.061 \frac{T_e}{R \ln \Lambda} \frac{10^{20}}{n} \eta_0 \quad (2.57)$$

with the electron temperature  $T_e$  in units of keV, the density  $n$ , the coulomb logarithm  $\ln \Lambda$  which is described in section 2.5, the major radius  $R$  and a specific normalized current drive efficiency  $\eta_0$  defined in [FB80]. Furthermore, a convention which is often used in literature defines a figure of merit by

$$\gamma = \frac{RI\bar{n}_e}{P10^{20}} m^{-2} AW^{-1} \quad . \quad (2.58)$$

This is used when super thermal particles are mainly responsible for current drive [WC87].  $\bar{n}_e$  is the averaged density here.

Considering the cost of producing the power used for current drive, it can be shown that the current drive by use of frequencies in the lower hybrid wave regime of 1 - 8 GHz is the most favored concept for a steady state tokamak device beside using internal bootstrap currents [Fre08].

### 2.4.2 Inductive Current Drive

This concept of current drive in fusion experiments utilizes the principle of a transformer. The primary winding of an air or iron transformer is located at the toroidal symmetry axis. The secondary winding is given by the plasma itself inside the torus. A current change in the primary winding produces a change in magnetic flux which is penetrating the air or iron core of the transformer. The setup is illustrated in figure 2.5.

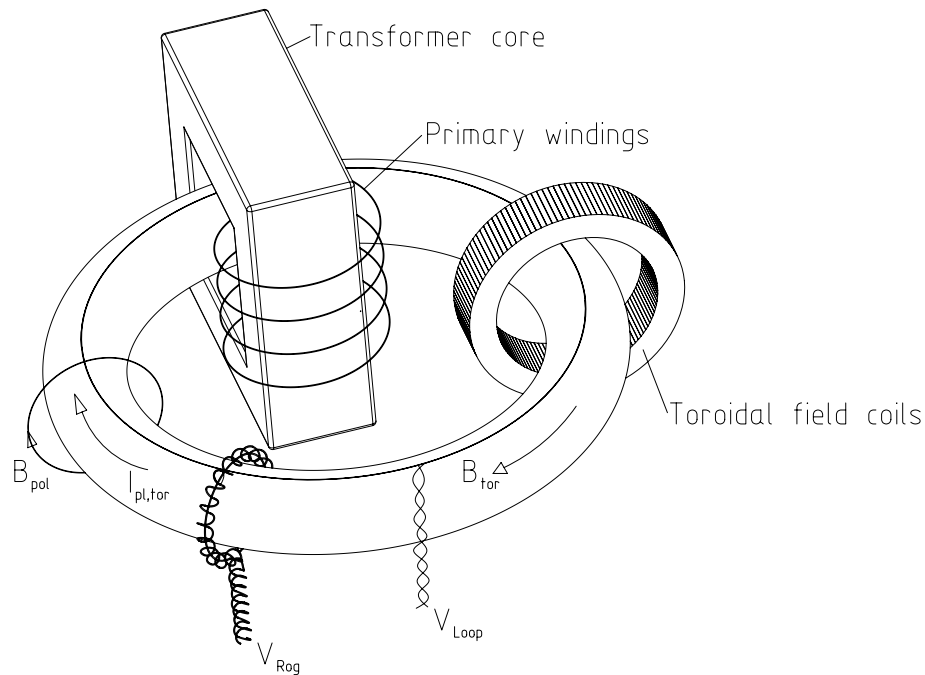


**Figure 2.5:** Transformer used for current drive in fusion device

This flux change results in a voltage which is applied to the plasma following by the induction law (described in chapter 3.1). Finally, this induced voltage, which is referred to as loop voltage, drives a current inside the plasma. This loop voltage is subject to equation

$$\frac{U_{trafo,ind}}{U_{loop}} = \frac{N_{trafo}}{N_{plasma}} = N_{trafo} \quad (2.59)$$

with the inductive component  $U_{trafo,ind}$  of the total transformer voltage  $U_{trafo}$  driving the current through the primary transformer coil.

The challenge is to generate a continuous flux change which necessitates a current change through the primary coil for plasma operation in a tokamak. Due to technical limitations in the current supply, much effort has been spent to find other ways to drive currents in a plasma. These concepts are explained in the next sections.

The plasma current can additionally be used for plasma heating. Here, the ohmic losses due to the finite plasma resistivity lead to an increase in the particle temperature. However, increasing the plasma temperature leads to a decrease in resistivity of the plasma which makes the heating mechanism more and more inefficient.



The plasma resistivity can be estimated by means of the Spitzer formula (2.71) which will be explained in section 2.5

### 2.4.3 Electron Cyclotron Current Drive

In comparison with LHCD described in section 2.4.4, electron cyclotron current drive (ECCD) only takes place at a resonant layer, leading to the opportunity to obtain a specific current drive profile. This is useful for changing the plasma current profile or local shear as well as to compensate for instance local bootstrap currents, which are described in section 2.4.6. For ECCD a wave is radiated into the plasma which is Doppler shifted with respect to the electron cyclotron frequency or harmonics.

The resonance condition for electron cyclotron damping is given by

$$\omega - \gamma\omega_{ce} = k_{\parallel}v_{\parallel} \quad (2.60)$$

with the electron cyclotron frequency  $\omega_{ce}$ , the relativistic factor  $\gamma$ , the parallel component (with respect to the magnetic field  $B$ ) of the wave vector  $k_{\parallel}$  and the parallel particle velocity  $v_{\parallel}$  of the wave [EG94]. Due to the non-zero  $k_{\parallel}$  spectrum of the wave, electrons with a well defined parallel velocity are heated and therefore accelerated stronger. This can be seen in figure 2.6, where the sphere of influence of the quasi linear diffusion operator is shown. The operator derived from the solution of the linearized kinetic equation is given by

$$\frac{\partial f}{\partial t} = \nu_{e0} \frac{v_{\parallel}}{v_{th,e}} f_{maxw} \quad (2.61)$$

with the electron collision rate  $\nu_{e0}$  the thermal and parallel particle velocities  $v_{th,e}$  and  $v_{\parallel}$ , respectively and the undisturbed Maxwellian distribution  $f_{maxw}$ . The operator describes which particles are shifted in phase space by radiation of a wave with  $\omega$  and  $k_{\parallel}$ . Here, in first order no current is generated, since only an increase of the perpendicular momentum takes place. However, for the resonantly heated particles the collision rate is reduced due to the increase in the particle temperature resulting in an asymmetry in the relaxation. This consequently leads to a slower relaxation to an isotropic distribution compared to the regime where the absorption took place. Thus, a net current results since the heated particles still exist preferably in one part of phase space but their origin regime is already isotropic again.

The normalized current drive efficiency by ECCD can be determined by

$$\eta_0 = \frac{3}{(5 + Z_{eff})} \left( \frac{v_{\perp}}{v_{Te}} \right)^2 \quad (2.62)$$

through investigating of the responsible collision processes regarding the change in

$v_{\perp}$  due to heating. The effective charge number is given by

$$Z_{eff} = \frac{\sum_k Z_{i,k}^2 n_{i,k}}{\sum_k Z_{i,k} n_{i,k}} \quad (2.63)$$

with  $n_{i,k}$  and  $Z_{i,k}$  for the density and charge number of the different ion species  $k$ , respectively.

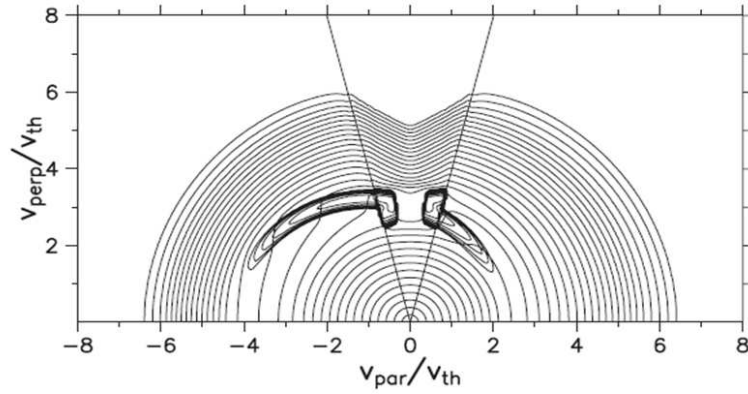


**Figure 2.6:** Influence of phase space by the diffusion operator [REG<sup>+</sup>97]

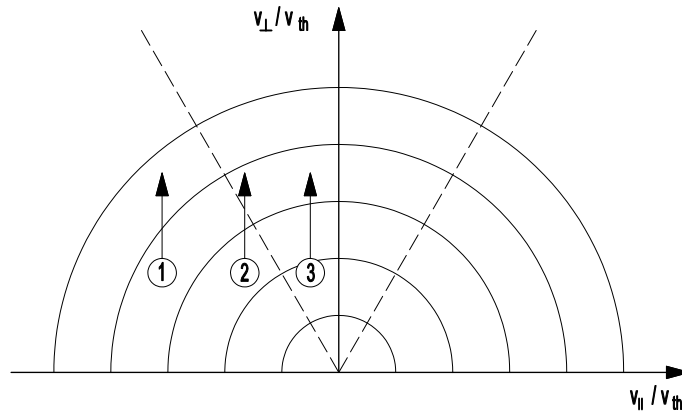


**Figure 2.7:** Influence of trapped particle cone for current drive

A further effect leading to a current drive by electron cyclotron damping exists due to the influence of the trapped particle cone. This resulting current component is referred to as Ohkawa current. If free particles are heated and shifted in phase space, these particles may reach the trapped particle cone. In figure 2.7 this is the case for particle 2. In the trapped particle cone the collision frequency is much higher compared to the passing particle regime, so that an isotropy in the cone is realized on a much faster time scale [WC87].

Anisotropy occurs since the trapped particles leave holes in the passing particle phase space regime (when they get trapped). This leads to a current drive in opposite direction compared to the previously described principle.

Depending on the power deposition it is also possible to drive currents with opposite directions by means of ECCD in plasmas. In case of weak single path absorption it is possible that the wave heats particles after passing the first resonant layer. In this case, considering equation (2.60), particles are heated, which have an opposite parallel velocity to compensate their higher cyclotron frequency due to the higher magnetic field. This process can take place several times for multi-path absorption in thin plasmas where the wave passes the plasma several times before being absorbed shown in figure 2.8. Therefore, the electron cyclotron current can flow in different directions at the magnetic high and low field side of the plasma resulting in a vanishing net current.

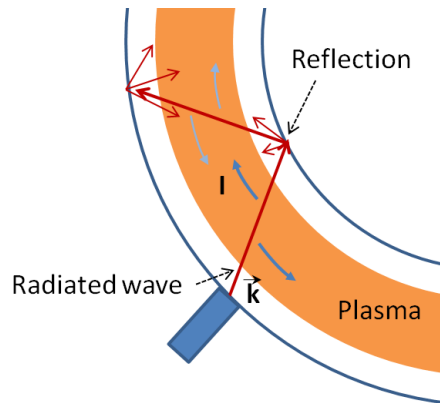


**Figure 2.8:** Generated current by means of multi pass absorption of the ECRH wave

#### 2.4.4 Lower Hybrid Current Drive

A further way to drive plasma currents is based on the radiation of waves in the direction of the magnetic field with a frequency close to the lower hybrid frequency. This method is referred to as lower hybrid current drive (LHCD). By use of a wave guide waves with a phase velocity matching the parallel velocity of the electrons are coupled into the plasma. Momentum and energy can be exchanged between the wave and the particle when the Landau resonance condition

$$\omega - \vec{k} \cdot \vec{v} = 0 \quad (2.64)$$

with the wave frequency  $\omega$ , the wave number  $\vec{k}$  and the particle velocity  $\vec{v}$  is fulfilled. Consequently, an absorption process via Landau damping takes place and the electrons are accelerated. Under typical reactor conditions the launched wave is

completely damped after a short path. Thus, only in this region a current will be driven.

The resulting current is determined by several factors. On the one hand the current is balanced by the momentum transfer (between the wave and the electrons) and the momentum loss due to collisions between accelerated electrons and ions. On the other hand, the collision frequency between the accelerated electrons and cold ions decreases since the collision cross section becomes smaller with increasing particle velocity. As a consequence the momentum loss of the accelerated electrons becomes slower resulting in an asymmetric conductivity [FB80]. As an approximation, three quarter of the total lower hybrid current originate from the change of the collision rate of the accelerated particles. Since all electrons which satisfy equation (2.64) gain momentum independently of their perpendicular velocity the resulting phase space normalized to the thermal velocity  $v_T$  obtains a broad asymmetry as seen as in figure 2.9. A normalized current drive efficiency  $\eta_0$  can be determined analog to equation (2.62) by the ratio of the normalized current and power density

$$\eta_0 = \frac{4}{(5 + Z_{eff})} \left( \frac{v_{\parallel}}{v_{th,e}} \right)^2 \quad (2.65)$$

with the thermal velocity  $v_{th,e}$  and a phase velocity  $v_P$  which correspond to the parallel particle velocity  $v_{\parallel}$  scaling with  $\nu^{-1/3}$  here [WC87]. The difference compared to (2.62) results from the distinction in the direction of the momentum change of the particles caused by the interaction with the wave. In case of non-reactor like cold plasmas, LHCD can be used to adjust the current profiles by changing the power deposition profile [Fre08]. In this way centrally peaked current profile can be generated by means of waves with high parallel phase velocity which leads to a deep penetration into the plasma. This effect becomes stronger with a higher magnetic field and a lower density [WC87].

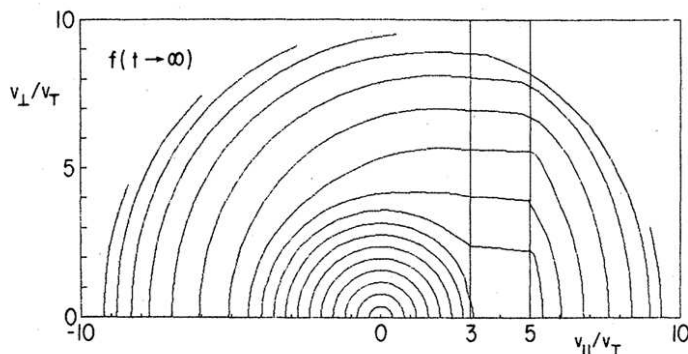


**Figure 2.9:** Velocity distribution of the electrons by using lower hybrid waves with a parallel phase velocity between 3 and 5 times the thermal velocity for current drive [Fis87]

### 2.4.5 Electron Bernstein Wave Current Drive

The concept of current drive by means of electron Bernstein waves (EBW) gives an opportunity to generate plasma currents with a higher efficiency compared to ECCD [LST94].

As described in section 2.3.2. Bernstein waves are generated inside the plasma by means of a mode conversion of the incident electromagnetic wave. Here, a parallel refraction index  $n_{\parallel} > 1$  can occur due to the electrostatic behavior of EBWs. However, it should be mentioned that  $n_{\parallel}$  depends on the magnetic field and can be changed by the magnetic shear, curvature and gradient [LMM<sup>+</sup>03].

Nevertheless, due to this refraction index  $n_{\parallel}$  and the related stronger Doppler shift, electrons with a preferred  $v_{\parallel}$  are heated and gain momentum and energy. This can be seen by the quasi linear diffusion operator which is shown in figure 2.10 and where  $n_{\parallel} = 1$  leads to a parabolic resonance curve.

Here, the heated particles rarely interact with the loss cone causing a smaller or even vanishing Ohkawa current. The improvement in the current drive efficiency results from avoiding Ohkawa currents, which point in the opposite direction with respect to the current produced by the microwave and may therefore compensate these.

Moreover, the perpendicular refraction index  $n_{\perp}$  can lead to wave lengths smaller than the gyro radius. This gives the opportunity for interaction of super thermal particles with EBWs as seen in figure 2.10 through the occurrence of the different grey regions for an increasing  $v_{\perp}$ .

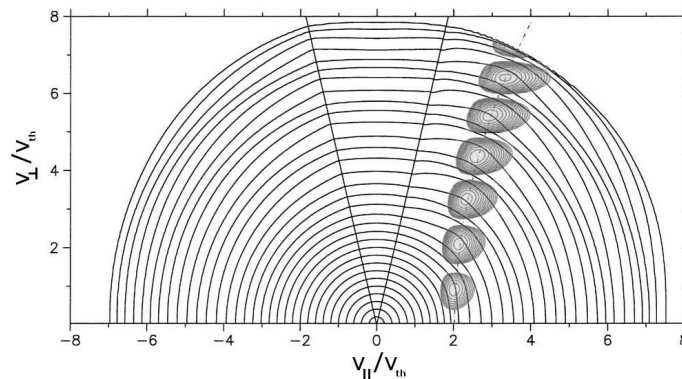


**Figure 2.10:** Influence of phase space by the diffusion operator for electron Bernstein waves [LMM<sup>+</sup>03]

### 2.4.6 Bootstrap Current

Bootstrap currents are the consequence of pressure gradients in plasmas as well as the existence of neoclassical particle orbits. In order to explain the concept two electrons at the point P with the same  $v_{\parallel}$  but different direction are considered. Both electrons follow neoclassical orbits which are referred to as banana orbits as seen for one particle in figure 2.11(a).

They are trapped in a magnetic bottle caused  $1/R$  dependence of the toroidal field<sup>1</sup>. Due to the  $\nabla B$  drift both particles will experience a drift. However, they are influenced different due to their different parallel velocity directions. The result is that both particles traverse different orbits as it is shown in figure 2.11(b).

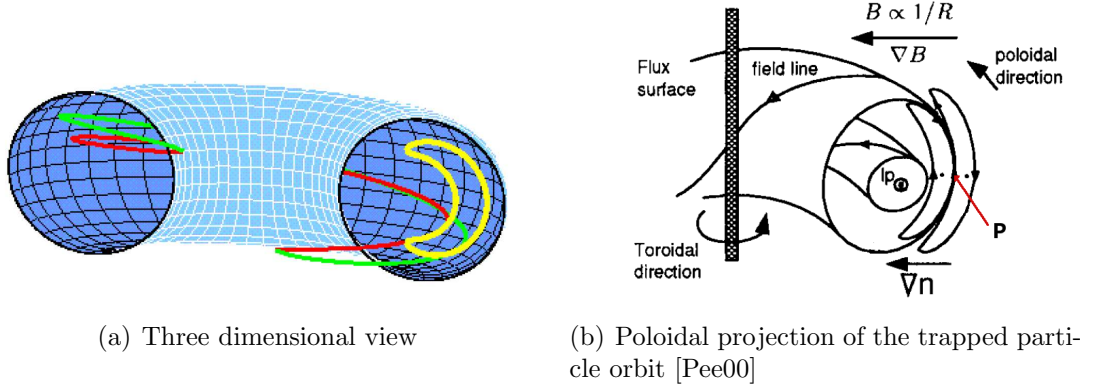


**Figure 2.11:** Banana orbit in a magnetically confined plasma

In presence of a density gradient more particles follow the inner orbit with a  $v_{\parallel,inn}(r = P)$  pointing opposite to  $v_{\parallel,out}(r = P)$  of the outer orbit. This leads to an asymmetry in the phase space which is shifted in opposite direction for electrons and ions.

Thus a net current from the trapped particles result which can be described by

$$j_T = -q \left( \frac{r}{R} \right)^{1/2} \frac{k_B T}{B} \frac{dn}{dr} \quad (2.66)$$

with the safety factor  $q$  which is the inverse of the normalized rotational transform  $t$  defined by equation 1.10.

A similar process occurs by means of the non-trapped particles since they have a drift depending on the direction of their parallel velocity [Fre08]. In presence of a pressure gradient these passing particle carry a net current given by

$$j_P = -q \frac{k_B T}{B} \frac{dn}{dr} \quad (2.67)$$

Additionally collisions between trapped and passing particles have to be considered. Collisions remove the discontinuity in phase space on the trapped-passing boundary. Here, an equilibrium in the momentum transfer between the trapped and the passing particles has to appear [Fre08].

<sup>1</sup>In case of a stellarator, particles can additionally be trapped in a mirror configuration caused by the helical coils

The required distribution of the passing particles leads to the collision driven part of the bootstrap current.

$$j_{BS} \approx -q \left( \frac{r}{R} \right)^{-1/2} \frac{k_B T n}{B r} \quad (2.68)$$

If a temperature gradient is also be considered, the total bootstrap current is given by

$$j_{BS} = -q \left( \frac{r}{R} \right)^{-1/2} \left( 2.44 k_B (T_e + T_i) \frac{dn}{dr} + 0.69 n \frac{d(k_B T_e)}{dr} - 0.42 n \frac{d(k_B T_i)}{dr} \right) . \quad (2.69)$$

The bootstrap current flows parallel to the toroidal field direction. Equation (2.69) has to be slightly adjusted for stellarator experiments [Pee00]. Here, precise knowledge about the magnetic field configuration is required.

### 2.4.7 Pfirsch-Schlüter Current

In order to reach a magnetic confinement of fusion plasmas a rotational transform of the magnetic field lines is necessary as shown in section 1.2. By means of the rotational transform a shorting of the vertical electric field arising from the charge separation caused by particle drifts occurs. The responsible equalizing currents flowing along the magnetic field lines are referred to as Pfirsch-Schlüter currents. For a large aspect ratio and a circular cross section the current density is defined by

$$j_{PS}(r) = -\frac{2r}{B_\theta R} \frac{dp}{dr} \cos\theta \quad (2.70)$$

with the poloidal magnetic field  $B_\theta$ , the radial pressure gradient  $dp/dr$  and the poloidal angle  $\theta$  [WC87]. The resulting magnetic field generated by these currents is directed vertically and leads to a shift of the flux surfaces - the Shafranov shift. The currents flow on the magnetic high field in opposite direction compared to the magnetic low field side. Thus, the net current in toroidal direction is zero.

## 2.5 Spitzer Resistivity

The plasma resistivity represents an essential value regarding the ohmic heating process and its efficiency. At the same time by means of knowledge of the loop voltage/current characteristic the electron temperature can be estimated. For this aim the parallel resistivity with respect to the magnetic field of a fully ionized gas can be described by means of the Spitzer-resistivity formula [Spi62].

$$\eta = \frac{Z_{eff}}{\gamma_E} \frac{\pi^{3/2} e^2 m_e^{1/2} \ln\Lambda}{2 (4\pi\epsilon_0)^2 (2k_B T_e)^{3/2}} \quad (2.71)$$

By using the electron temperature in units of eV the formula turns to

$$\eta = 3.04 \cdot 10^{-5} \frac{Z_{eff}}{\gamma_E} \frac{\ln \Lambda}{(T_e)^{3/2}} \Omega m \quad . \quad (2.72)$$

Here, the Fokker-Planck-Equation was numerically solved for electrons in a steady-state plasma. The velocity distribution of the electrons was assumed to be Maxwellian with a small perturbation. In the first step only interaction of electrons with ions have been considered [CSR50]. However, Spitzer found that electron-electron collisions cannot be neglected [SH53].

In equation 2.71  $\ln \Lambda$  represents the so called Coulomb logarithm. For the case that the electron temperature is greater than the ion temperature ( $T_e > T_i$ ) and an ion charge of  $Ze$  an approximation of the Coulomb logarithm is given by

$$\ln \Lambda \approx \begin{cases} 29.9 - \frac{1}{2} \ln \left( \frac{n_e}{m^{-3}} \right) + \frac{3}{2} \ln \left( \frac{T_e}{eV} \right) + \ln(Z), & \text{if } T_i m_e / m_i < 10 Z^2 eV < T_e \\ 30.9 - \frac{1}{2} \ln \left( \frac{n_e}{m^{-3}} \right) + \frac{1}{2} \ln \left( \frac{T_e}{eV} \right), & \text{if } T_i m_e / m_i < T_e < 10 Z^2 eV \end{cases} \quad (2.73)$$

with the electron density  $n_e$ . An overview for different parameters is given in [NRL]. It can be seen, that the Coulomb logarithm is a weak function of  $n_e$  and  $T_e$ . For WEGA plasmas  $\ln \Lambda \approx 14$ . For a fusion reactor  $\ln \Lambda \approx 16$ .

The term  $\gamma_E$  has been introduced since the electron-electron collision cross-section depends on the ionic charge of the plasma.  $\gamma$  is listed for different values in table 2.1.

**Table 2.1:** Ionic charge dependence on  $\gamma_E$

$Z_{eff}$	1	2	4	16	$\infty$
$\gamma$	0.5815	0.6833	0.7849	0.9225	1

By knowing the plasma current and the loop voltage the integral plasma resistance is given by

$$\begin{aligned} R &= \frac{U_{loop}}{I_{Pl}} \\ &= \eta \frac{2\pi R}{\pi a^2} \end{aligned} \quad (2.74)$$

for a circular cross-section. Therefore, by using equation (2.72) and (2.74) the flux surface averaged electron temperature is given by

$$T_e = 1.55 \cdot 10^{-3} \left( \frac{Z_{eff} \ln \Lambda}{\gamma_E} \frac{I_{Pl}}{U_{loop}} \frac{R}{a^2} \right)^{2/3} eV \quad . \quad (2.75)$$





## 3 Magnetic Diagnostics

Magnetic diagnostics are a basic module in all fusion experiments. They provide access to base parameters of high temperature plasmas, which are indispensable for magnetic confinement experiments. Magnetic diagnostics can be divided in inductive and non inductive sensors. The first are exclusively used in this thesis and will be explained in the next chapters. An overview of non-inductive sensors can be found e.g. in [SFMT08, HKW06].

### 3.1 Inductive Magnetic Diagnostics

The basic principle of the measurements is the same for all inductive magnetic diagnostics - the induction law. Loops and coils that are pervaded by a magnetic field are used. The induced voltage at the ends of the loop is measured. The amplitude of the voltage

$$V = \oint_C \vec{E} \cdot d\vec{l} = -\frac{d}{dt} \int_S \vec{B} \cdot d\vec{A} \quad (3.1)$$

is determined by the line integral along the curve  $C$ , which encloses the surface  $S$ , in the electric field that exists due to the temporal change in flux  $\vec{B} \cdot \vec{A}$ . The pervaded flux area  $A$  is constant in most diagnostically applications. Thus, the measured signal is proportional to magnetic field change. Since only inductive magnetic diagnostics are used in this thesis, the term inductive will be skipped subsequently. By integration of the measured signal, the magnetic field, as well as the related current producing the magnetic field, can be determined. Different types of flux loops have to be distinguished with respect to the different magnetic fluxes measured in an experiment.

#### 3.1.1 Rogowski Coil

A Rogowski coil (named after Walter Rogowski's work in 1912 [Rog12]) can be used to measure a current flowing within a conductor. Due to the existence of free charged particles a plasma also depicts a conductor.

The magnetic field along an arbitrary closed contour  $C$ , which encircles the conductor, is related to the current  $I$  in the conductor by

$$\oint_C \vec{B} \cdot d\vec{l} = \mu_0 I \quad . \quad (3.2)$$

Here,  $d\vec{l}$  is a line element of the arc length along  $C$ . In order to measure this flux, a coil has been designed whose axis follows the curve  $C$ . If the space for construction is limited, one way to accurately measure the flux is through the use of segmented Rogowski coils that have been connected in series [WEGK08]. As seen by equation (3.1) the magnetic flux passing through one of the windings only gives information about an average magnetic field due to the surface integral. Therefore, the windings of a Rogowski coil should be small so that the magnetic field does not vary significantly in direction and magnitude. The condition becomes of less importance if the Rogowski coil has the shape of a toroid and the plasma current density is symmetric and flows on the axis of the toroid. In this case, every winding measures the same flux.

Furthermore, in case of a non toroidal shape, the winding area has to be perpendicular to  $\vec{B}$  created by the current  $I$  in order not to measure any unintentional flux. Additionally, the Rogowski coil needs to have a return winding, otherwise a field that is perpendicularly passing through the area  $C = \pi r_{Rog}^2$  will also be measured. In the simplest case, one end is returned through the coil itself - without any windings - to the beginning. It is also possible to make a second layer of windings in order to lead one cable end back to the beginning. Here, the direction of the winding rotation has to be contrary to the first layer. Now, only the area spanned by the windings  $N$  seen in figure 3.1 contributes to the flux area.

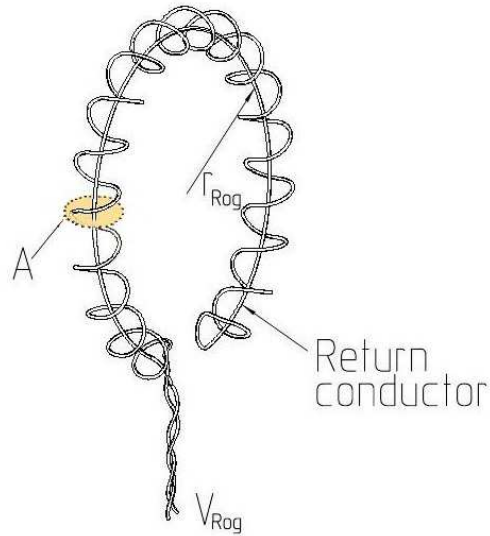


**Figure 3.1:** Rogowski coil

In case of a toroidal Rogowski coil that has a major Radius  $R$  and lies in a poloidal plane of the vessel, the measured flux is given by

$$\Phi = \sum_{i=1}^N \int_S \vec{B} \cdot \vec{e}_\theta dA \quad . \quad (3.3)$$

Based on a homogenous winding density  $n$  along  $\vec{l}$ ,  $\vec{e}_\theta$  can be expressed by

$$\begin{aligned}\vec{e}_\theta &= \frac{d\vec{l}}{Rd\theta} \\ &\approx \frac{N\Delta\vec{l}}{2\pi R} .\end{aligned}\quad (3.4)$$

Thus the flux through the Rogowski coil is

$$\begin{aligned}\Phi &= \int_S \frac{N}{2\pi R} \left( \sum_{i=1}^N \vec{B} \cdot \Delta\vec{l} \right) dA \\ &\approx \int_S \frac{N}{2\pi R} \left( \oint_C \vec{B} \cdot d\vec{l} \right) dA \\ &= \frac{NA\mu_0 I}{2\pi R}\end{aligned}\quad (3.5)$$

where  $A$  the area of one winding. By means of the induction law, the measured signal is

$$V = -\dot{\Phi} = -\frac{NA\mu_0 \dot{I}}{2\pi R} .\quad (3.6)$$

An integration is still required in order to get a signal proportional to the current.

### 3.1.2 Diamagnetic and Compensation Loop

In order to determine the diamagnetic effect, and thus the plasma pressure, so called diamagnetic and compensation loops are used. These loops lie in a poloidal plane and measure the toroidal flux change. The mean magnetic field is again determined by integrating the measured voltage and having a constant flux area. Both systems can be located inside or outside of the plasma vessel whose consequences are discussed in section 4.1.1. The difference between the different loops is that the diamagnetic loop fully encloses the plasma while the compensation loop only measures the vacuum magnetic field flux, since no plasma reaches the area between the windings. This can be seen in figure 3.2.

In order to determine the diamagnetic effect, the diamagnetic loop measures the flux

$$\Phi_{\text{dia}} = \Phi_{\text{dia,vac}} + \Delta\Phi \quad (3.7)$$

$$= \langle \vec{B}_{\text{dia,vac}} \rangle \cdot \vec{A}_{\text{dia}} + \Delta\Phi \quad (3.8)$$

consisting of the vacuum flux  $\Phi_{\text{dia,vac}}$  and the change of flux  $\Delta\Phi$  due to the diamagnetic current, the plasma current and its profile as shown in chapter 2.1.

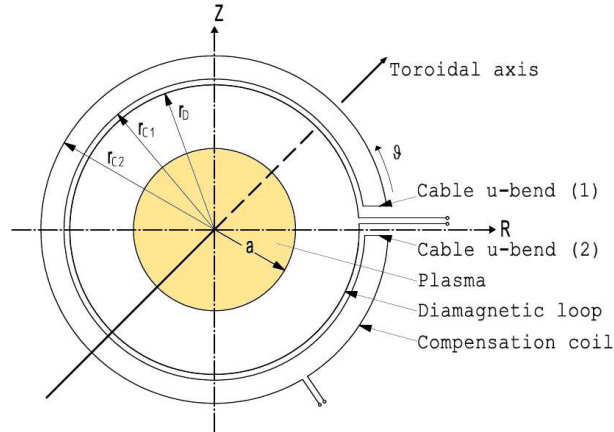


**Figure 3.2:** Flux area of a diamagnetic and compensation coil

On the other hand the compensation loop only measures the vacuum magnetic flux.

$$\Phi_{\text{comp}} = \Phi_{\text{comp,vac}} \quad (3.9)$$

$$= \langle \vec{B}_{\text{comp,vac}} \rangle \cdot \vec{A}_{\text{comp}} \quad (3.10)$$

### 3.1.3 Toroidal Flux Loop

In tokamak experiments the use of a toroidal flux loop is an easy way to get access to the electron temperature. A toroidal flux loop is located in a toroidal plane and encloses the transformer core, as seen in figure 2.5. A loop voltage is then induced by a vertical magnetic flux. This flux can be generated by a transformer, vertical field coils used for shifting the plasma radially and lastly by the plasma current itself. Therefore, one has to distinguish between the causes of the flux change. In the instance that a transformer is used (described in chapter 2.4.2) and there are stationary plasma conditions, the loop voltage given by equation (2.59) corresponds to the voltage driving the plasma current.

By knowing the plasma current, as well as the loop voltage, the average electron temperature can be determined by using equation (2.75).

In case of a non-stationary plasma current, the loop voltage is altered by the plasma acting as well as by the transformer primary winding. Furthermore, if the plasma current is constant and no transformer is used, the loop voltage will be zero since no vertical magnetic flux change is generated. The use of equation (2.75) is not possible in under these conditions.

## 3.2 Systems for Determination of the Diamagnetic Effect

In literature, different systems that measure the diamagnetic effect by means of diamagnetic loops can be found for [TCK86, JD02, MBT03, SWZ04, Ba01]. Two of them were used in this work and will be presented in the following. The first system based on the opportunity to determine the influence of the vacuum magnetic field described by the second term in equation (2.10) as a compensation method for signal measured by the diamagnetic loop. The second system relies on a relative measurement between two diamagnetic loops and is described in chapter 3.2.2. The construction of the different systems at WEGA is specified in chapter 4. The results and comparisons between the different systems are shown in chapter 5.6.

### 3.2.1 Diamagnetic and Compensation Loop System

The first system to determine flux changes is comprised of a combination of both a diamagnetic and compensation loop. Due to the difference in the flux area of both loops a calibration factor  $D$  has to be introduced.  $D$  can be determined from vacuum field measurements.

$$D = \frac{\Phi_{\text{dia,vac}}}{\Phi_{\text{comp,vac}}} \quad (3.11)$$

By using this factor and equation (3.7) as well as (3.9), the diamagnetic flux change can be determined by

$$\Delta\Phi = D \cdot \Phi_{\text{comp}} - \Phi_{\text{dia}} \quad (3.12)$$

### 3.2.2 Two Loop System

The two loop system consists of two diamagnetic loops with different flux areas. The loop with a smaller area is called the inner loop whereas the other loop is called the outer loop. The formula index is 'inn' and 'out', respectively. Both loops are located in the same poloidal plane as illustrated in figure 3.3. The system is determined by

$$\Phi_{\text{inn}} = \Phi_{\text{inn,vac}} + \Delta\Phi \quad (3.13)$$

$$\Phi_{\text{out}} = \Phi_{\text{out,vac}} + \Delta\Phi \quad (3.14)$$

where the index (vac) describes the influence of the vacuum field. Since their flux ratio does not change during the shot, the ratio parameter  $k$  is introduced.

$$k = \frac{\Phi_{\text{out,vac}}}{\Phi_{\text{inn,vac}}} \quad (3.15)$$

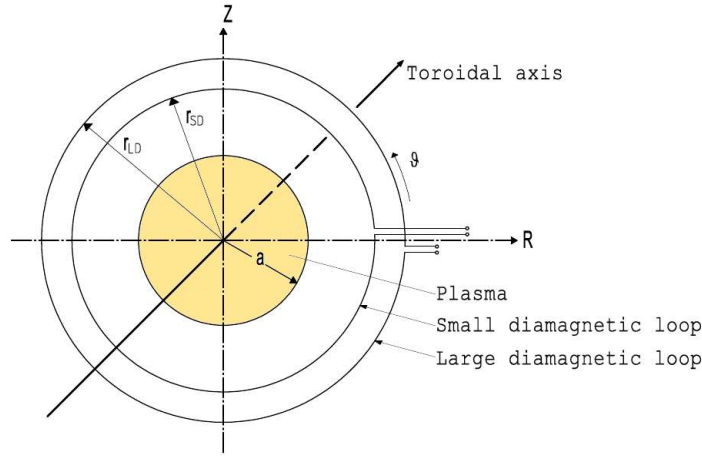


**Figure 3.3:** 2-loop system used to measure the plasma energy

Combining equation (3.13), (3.14) and (3.15) leads to

$$\Delta\Phi = \frac{1}{1-k} (\Phi_{\text{out}} - k \cdot \Phi_{\text{inn}}) \quad . \quad (3.16)$$

The parameter  $k$  can be measured by two ways. The first of these ways is to use a vacuum field pulse where  $\Delta\Phi = 0$  so that  $\Phi_{\text{out}} = \Phi_{\text{out,vac}}$  and  $\Phi_{\text{inn}} = \Phi_{\text{inn,vac}}$ . In this case  $k$  can be determined by means of (3.15). The second way uses the approximation of the magnetic field

$$\langle B_{\text{out,vac}} \rangle \approx \langle B_{\text{inn,vac}} \rangle \quad (3.17)$$

which is justified due to the small difference in the flux area of both loops. In this case  $k$  is described by

$$\begin{aligned} k &= \frac{\langle B_{\text{out,vac}} \rangle \cdot A_{\text{out}}}{\langle B_{\text{inn,vac}} \rangle \cdot A_{\text{inn}}} \\ k &\approx \frac{A_{\text{out}}}{A_{\text{inn}}} \end{aligned} \quad (3.18)$$

and can be determined by measuring the flux area.

### 3.3 Integrators

In order to evaluate the raw signals coming from the magnetic diagnostics, a temporal integration of these signals has to take place. This is due to the fact that only the change of the magnetic flux  $\Phi$  is measured by inductive magnetic diagnostics. Different concepts of integrators are available for the desired integration. The most widespread implementation uses analog integrators. The raw signal is picked up by an integrating electric circuit with integration time  $\tau$  making the integrated signal immediately available.

$$U_{int}(T) = -\frac{1}{\tau} \int_0^T U_{raw} dt \quad (3.19)$$

This concept is only briefly represented in the following. The second option is the digital integration of the signal, which is explained in section 3.3.2.

#### 3.3.1 Analog Integrators

Analog integrators can be divided into active and passive integrators. The latter are suited for the integration of signals on a short time scale. Circuits of passive integrators are shown in figure 3.4. The related complex transfer function is

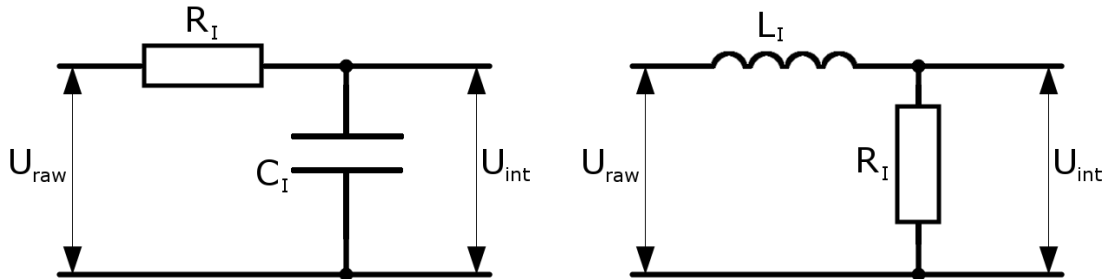


*Figure 3.4: Passive RC-integrator and RL-integrator*

$$U_{int} = \frac{1}{1 + i\omega\tau} U_{raw} \quad (3.20)$$

with  $\tau = R_I C_I$  and  $\tau = L_I / R_I$ , respectively. In the range of  $\omega\tau \gg 1$  equation (3.20) corresponds to equation (3.19). However, for small frequencies this is not the case. If  $\tau$  is increased as a countermove, the output amplitude will be reduced due to the inappropriate voltage ratio. This effect is increased by using the analog integrator in on-load operation. This condition limits the operational range of a passive integrator.

In comparison to a passive integrator an active integrator does not have this type of drawback. The fundamental difference is that an active integrator contains a operational amplifier stage, shown in Figure 3.5.



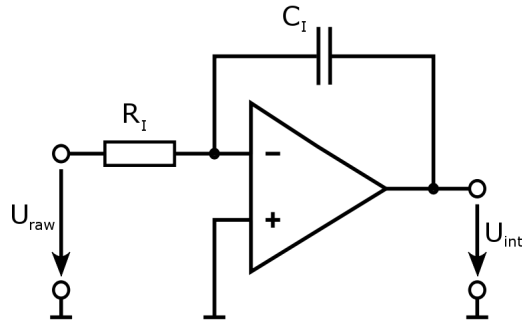


**Figure 3.5:** Active integrator

The output voltage is given by

$$U_{int}(T) = -\frac{e^{-T/\tau G_\infty}}{\tau} \int_0^T e^{-T/\tau G_\infty} U_{raw} dt \quad (3.21)$$

with  $G$  as the finite high open loop gain of the amplifier ( $G_\infty > 140$  dB) and  $\tau = R_I C_I$ .  $R_I$  is the input resistance and  $C_I$  the feedback capacitance. Thus, the output signal dependence on the load at  $U_{int}$  is reduced by the operational amplifier. One of the biggest drawbacks in working with active analog integrators is the input offset voltage drift of the amplifying stage. This leads to the fact that in addition to the raw signal, an arbitrary perturbation value is continuously integrated. Moreover, this value depends on temperature due to the changing resistance of electronic components. Particularly in long term experiments the drift can lead to large errors in the integrated signal.

One opportunity to suppress this error is through the use of a feedback circuit, which adjusts the input during non-plasma operation in order to minimize the output signal. During plasma operation, this circuit is switched off and the last offset value is used for the whole plasma discharge.

At present, the best analog integrator is located at the tokamak KSTAR. A drift of 5 mV at the output stage could be demonstrated during a 100 s pulse (corresponding to an integrated drift of  $5 \mu\text{V} \cdot \text{s}$ ) [SFMT08, BLS04]. Further technical improvements and first results of magnetic measurements at KSTAR can be found in [KLBS08, LBK<sup>+</sup>08]. Another proposed method is that two analog integrators, which alternately measure and determine the offset, are used [AAK93].

### 3.3.2 Digital Integrators

The digital integrator that is exclusively used in this thesis has been developed for Wendelstein 7-X. In this thesis, the integrator has been tested for the first time in continuous experiment operation. One of their major advantages is that the output range of the integrated signal is not limited by the output stage itself.

Furthermore, a much better drift compensation compared to analog integrators could be realized [SFMT08, Wer06]. The principle of the integrator is shown in figure 3.6 and will be explained in the following.

In a simplest version of a digital integrator the measured signal is directly detected by an analog-to-digital (ADC) converter and the values are integrated via software. However, in order to suppress aliasing effects in the integrated signal resulting by non-consideration of the Nyquist-Shannon sampling theorem a low pass filter is necessary in front of the ADC [Sha98]. Additionally, an amplifier is required in order to make the measured values independent on the load at the output stage and furthermore amplifying these values. Since these electronic parts will lead to drift which influences the integrated signal a suppression of the drift is necessary.

For this purpose, the raw signal of the magnetic diagnostic is chopped by an electronic switch which is driven by a clock signal. Here, - in a simple model - a polarity change of the raw signal is realized at the first amplifier input stage. The amplified and chopped signals as well as the clock signal are detected by an ADC. Using these time traces, a software reconstruction of the raw signal is performed where the drift of the amplifier stage averages out due to the prior chopping process. This is the essential factor in performing long time integration of a signal where a minimal drift or error voltage will lead to large errors in the integrated signal. After the reconstruction, an integration is realized.

Using this technique, a maximum drift of  $70 \mu V / 1000 s$  (equals an integrated drift of  $0.07 \mu V \cdot s$ ) has already been demonstrated [Wer06]. Moreover, an improved common mode rejection has been shown.

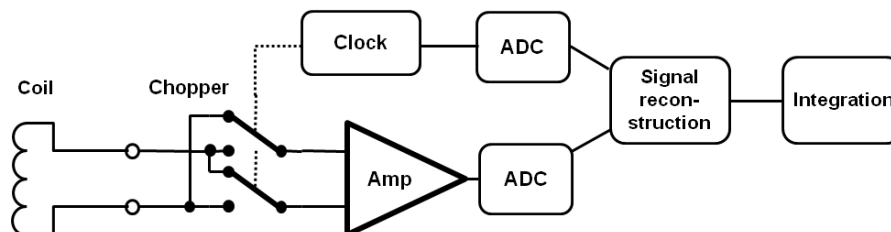


**Figure 3.6:** Principle of the digital integrator

During this thesis, a new algorithm performing the reconstruction and integration has been developed. This algorithm, as well as its performance, will be explained in section 4.2.1. Additional improvements concerning the suppression of beat frequencies could be realized, which are described in section 4.2.3.



## 4 Diagnostic Setup at the WEGA Stellarator

The principle of measurements by means of magnetic diagnostics has been described in section 3.1. In section 4.1 the assembling of the different magnetic loops is described. Within this work a diamagnetic loop, a compensation coil and a two-loop system, consisting of two further diamagnetic loops, have been build up. Furthermore, two Rogowski coils for plasma current measurements as well as three Rogowski coils for measuring the magnetic field coil current has been constructed and put into operation, respectively.

The received raw signal from the diagnostics is chopped by the integrator board (also referred to as chopper) and detected by an analog-to-digital converter, which can be seen in the signal path shown in figure 4.1. These values are saved in the Objectivity database developed for W7-X. By means of an appropriate software algorithm the chopped signal can be reconstructed and integrated later on. Here, an integration algorithm, which is explained in section 4.2.1 has been developed which allows the implementation into the online data processing system planned for W7-X.

During the development phase of this work data were integrated offline. The algorithm and the data evaluation program was implemented in IDL; in an application called MagPlot. The integrated signals are saved as netCDF files, which is the default file type used for WEGA diagnostics. This permits a synchronous comparison of the results with other diagnostics.

### 4.1 Assembling of Magnetic Loops

This section describes the assembly of the different magnetic diagnostics at WEGA. At first the diamagnetic loops and compensation coils will be specified before the setup of Rogowski coils is characterized. In order to comprehend the complicated construction, the diagnostic requirements will be illustrated in the following.

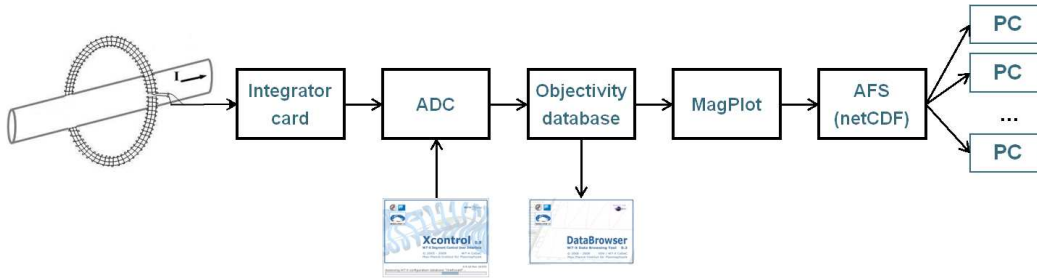


**Figure 4.1:** Signal path for the evaluation of magnetic diagnostic measurements at WEGA

### 4.1.1 Diagnostic Requirements

One of the main tasks of this thesis was to build up a system of fast magnetic diagnostics. Here, the term “fast” corresponds to the fact that a magnetic flux signal is damped by the skin effect which leads to a time delay if magnetic fields have to penetrate a conducting body before they can be measured by loops. In order to reduce this effect all diamagnetic diagnostics and one Rogowski coil had to be designed for inside of the vessel. This leads to two secondary conditions.

First, the diagnostics were not allowed to touch or disturb the plasma. This limits the width of the diagnostics. Furthermore, the mounting can only be realized through the existing ports. The second condition is that all cables needed an additional metal shielding in order to protect them from microwave stray radiation. This increases the challenge of mounting a completely shielded system surrounding the plasma through ports with a maximum diameter of 92 mm. The solution and implementation will be described in the following.

A further requirement for the diagnostics follows by the wide range of expected plasma parameters. For example, the dynamic range of current measurements should cover at least 3 orders of magnitude (1 - 2000 Ampere). On the other hand, flux changes have to be detected which are 5 orders smaller than the stationary flux signal itself. Furthermore, these measurements have to be realized for a discharge time of 1 - 60 seconds. These conditions require optimizations of the digital integrator, described in section 4.2.

### 4.1.2 Diamagnetic Loop

A diamagnetic loop, whose principle is explained in section 3.1.2, of 16 windings has been installed at the WEGA stellarator. The required shielding of the windings against microwave stray radiation could be realized by stainless steel pipes surrounding the wires. The inner diameter of these pipes was the limiting factor for the winding number. The setup is presented in figure 4.2 and the dimensions of the used pipes are listed in table 4.1.

A system consisting of different pipes for shielding the cable had to be used since otherwise the mounting through the port could not be realized. Here, 4 pipes have been utilized.

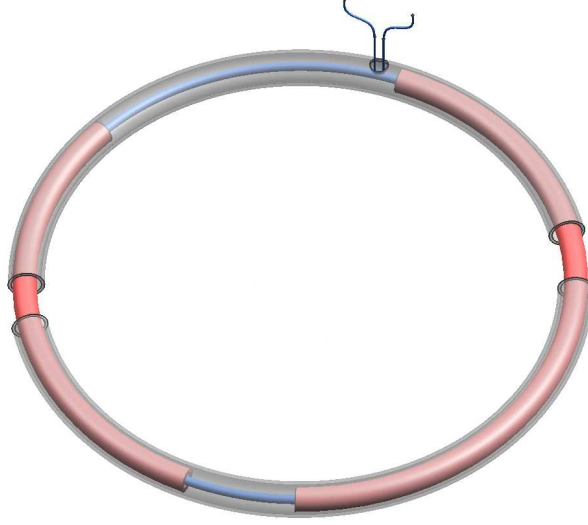


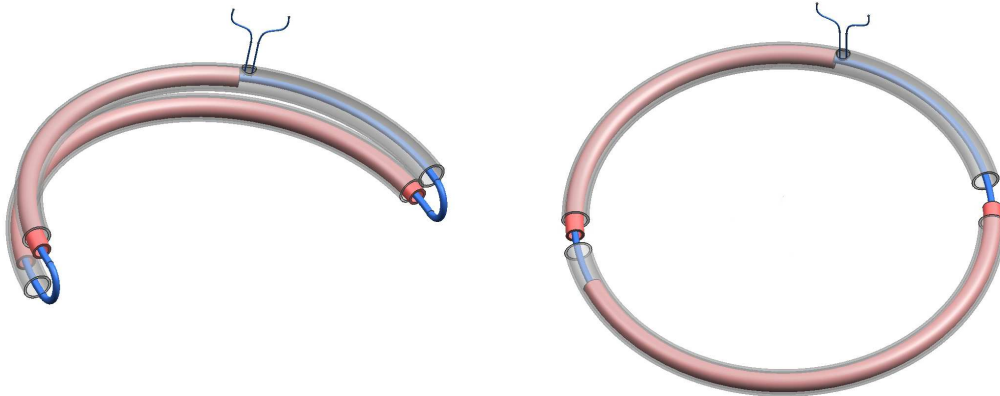
**Figure 4.2:** Setup of the diamagnetic loop consisting of 4 stainless steel pipes

**Table 4.1:** Dimensions of the used pipes for construction the diamagnetic loop

Identifier	$r_{curv}/[mm]$	$\alpha/[^{\circ}]$	$r_{inn}/[mm]$	$r_{out}/[mm]$
$Dia_{inn1}$	181	160	3	4
$Dia_{inn2}$	181	110	3	4
$Dia_{out1}$	181	163	5	6
$Dia_{out2}$	181	167	5	6

Two of the four pipes have an outer diameter which is slightly smaller than the inner diameter of the other pipes. Therefore, the pipes could be telescoped (open state) so that the top and bottom pipe bow could be folded. With both pipe bows lying side by side (figure 4.3(a)), it was possible to lead the whole construction through a free WEGA port having a diameter of 89 mm. In the next step the bows were flipped back so that they lie in a poloidal plane inside the vessel (figure 4.3(b)). In the last step the outer pipes were shifted, so that they overlap parts of the inner pipes (closed state), as shown in figure 4.2. Marks at the inner pipes, which could be scanned by the fingers, serve as identification for the required shift of the outer pipes. Due to the overlapping pipes the cable windings were totally shield against the plasma and microwaves. Furthermore, in the closed state the construction is sufficiently mechanically stable inside the vessel.

Pulling the cable through the pipes has been performed at a self constructed mounting device (figure 4.4). This device kept the pipes in the open state. The cable was launched into the pipe system through a hole in one of the inner pipes. At the accessible points marked with A and B in the figure 4.4 the cable could be pulled in order to realize 16 windings. Then, the cable end was lead back through the hole again.



(a) Folded diamagnetic loop for leading through the WEGA port

(b) Open state of the diamagnetic loop

**Figure 4.3:** Change of the position of the pipes in order to implement the shielded loop inside the WEGA torus

Outside of the pipes the cable pair has been twisted in order to prevent parasitic flux areas. The further cable route to the port could be shielded by a flexible corrugated stainless steel tube which was attached to the hole in the pipe. A Teflon isolated cable was used due to their high thermal temperature stability and sufficient vacuum capability.



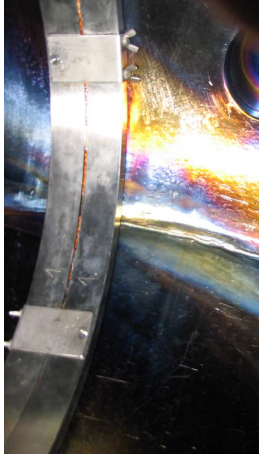
**Figure 4.4:** Mounting device for diamagnetic loop

The average radius of the winding packet is 181 mm. Although possible misalignment of the cables inside the pipes might introduce a small systematic error, which is was determined in the appendix, an average flux area per winding of

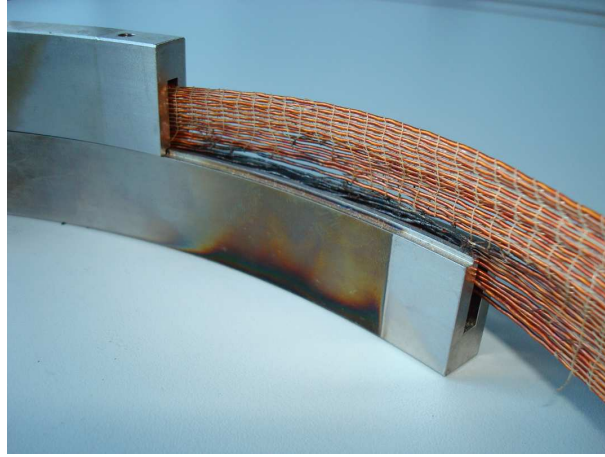
$$A = 1029.2(\pm 20.7) \text{ cm}^2 \quad (4.1)$$

has been estimated. The problem in shielding the winding packet should be shortly shown by a previously used diamagnetic loop in WEGA. This diagnostic consisted of two U-profiles, which were plugged into each other.

The cable packet was located in the slip which can be seen in figure 4.5(b). Each of the U-profiles was made by 3 poloidal sections of  $120^\circ$ , which were connected inside the vessel. However, during plasma operation the cable burned in the region of the gaps of the U-profiles so that the diagnostic had to be removed.



(a) Diamagnetic loop of 2006 inside the WEGA torus



(b) Insufficient cable shielding by two U-profiles leading to cable fire

**Figure 4.5:** Destroyed diamagnetic loop of 2006

### 4.1.3 Compensation Loop

The compensation loop developed for WEGA contains 19 windings with a flux area of

$$A = 184.3(\pm 36.2) \text{ cm}^2 \quad (4.2)$$

per winding. For this purpose pipes listed in table 4.2 are used.

**Table 4.2:** Dimensions of pipes used for construction of the compensation loop

Identifier	$r_{curv}$	$\alpha$	$r_{inn}$	$r_{out}$
$Com_{inn01}$	181	159	6	8
$Com_{inn02}$	181	117	6	8
$Com_{out01}$	181	138	10	12
$Com_{inn11}$	164	159	6	8
$Com_{inn12}$	164	170	6	8
$Com_{out11}$	164	163	10	12
$Com_{cor1}$	-	-	8.5	12
$Com_{cor2}$	-	-	8.5	12



Taking the cable path shown in figure 3.2 into account the inner bow was realized by pipes with a curvature radius of 164 mm. The connections between the inner and the outer bow were made by corrugated metal tubes, which could be flexibly bent. This was necessary to realize cable drawing inside the pipes performed at a mounting device which can be seen in figure 4.6. After the cable installation the pipes were connected by the corrugated tubes and bent into their final position. A former bending was not possible since the cable would get stuck at the places of the bended tubes during the cable drawing.



**Figure 4.6:** *Mounting structure for assembling the compensation coil*



(a) *Top view*



(b) *Bent corrugated tubes to realize the cable path of the compensation coil*

**Figure 4.7:** *System of diamagnetic (in front) and compensation loop (back)*

The cable shielding between the pipe system and the port feed through was realized analog to the diamagnetic loop by means of further corrugated tube. The

distance between both pipe bows was adjusted by clamps. Further clamps were used to connect the diamagnetic loop with the compensation loop to facilitate the later mounting inside the vessel seen in figure 4.7. This system has been inserted first into WEGA.

#### 4.1.4 Two Loop System

The theoretical concept of a 2-loop system is explained in section 3.2.2. Both diamagnetic loops used have 30 windings each with a flux area of

$$A_{out} = 1029.2(\pm 13.3) \text{ cm}^2 \quad (4.3)$$

$$A_{int} = 845.0(\pm 12.0) \text{ cm}^2 \quad (4.4)$$

per winding. The construction as well as the cable drawing for each loop took place analog to the diamagnetic loop described in section 4.1.2. Table 4.3 lists all used pipes for the 2-loop system. The distance between both diamagnetic loops has been adjusted by distance clamps. This system has also been installed through a WEGA port with a diameter of 89 mm. However, now four outer pipes had to be shifted in order to realize the overlap, making the installation more complicated.

**Table 4.3:** Dimensions of the pipes used for construction of the 2-loop system

Identifier	$r_{curv}/[mm]$	$\alpha/[^{\circ}]$	$r_{inn}/[mm]$	$r_{out}/[mm]$
$2LS_{inn01}$	164	69	6	8
$2LS_{inn02}$	164	171	6	8
$2LS_{out01}$	164	167	10	12
$2LS_{out02}$	164	171	10	12
$2LL_{inn01}$	181	69	6	8
$2LL_{inn02}$	181	171	6	8
$2LL_{out01}$	181	167	10	12
$2LS_{out02}$	181	171	10	12

### 4.1.5 Rogowski Coils

At the WEGA stellarator two Rogowski coils for plasma current measurements - one internal and one external - were put in operation. The external coil, shown in figure 4.8, was segmented in two parts. It was previously used at Wendelstein 7-AS and reinstalled at WEGA. Thus, the exact geometry and number of windings are unknown. But since Rogowski coils can be absolutely calibrated this knowledge is not necessary for the measurements.

The internal Rogowski consists of 850 windings isolated by Kapton<sup>®</sup>. The cable was wound on a Viton<sup>®</sup> tube. This coil was also put into a metal pipe construction to realize the plasma and microwave shielding. Therefore, the system could also be lead through the port in the vessel. The internal Rogowski coil was mounted together with the 2-Loop system. This can be seen in figure 4.9.

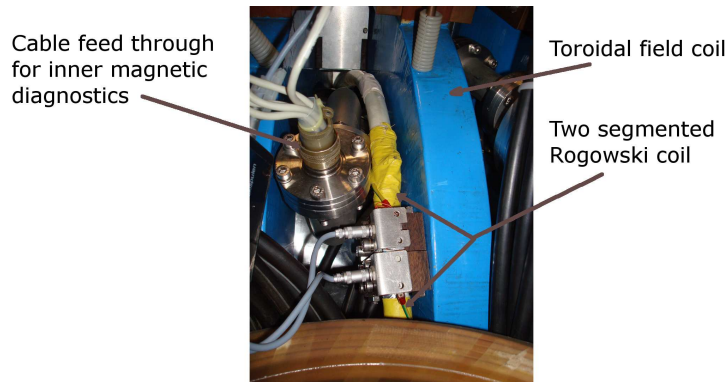


**Figure 4.8:** Two segmented external Rogowski coil for plasma current measurements

Three further Rogowski coils of the same type as the previously described outer one have been integrated in the WEGA experiment operation. They are used to measure the toroidal, helical and vertical field coil current. The first both are located at the current supplies of the field coils shown in figure 4.10 (a) and (b). The last encloses the lower vertical coil windings which can be seen in figure 4.10 (c).

### 4.1.6 Place of Location

With respect to the development of magnetic diagnostics system inside the WEGA vessel an estimation of the maximum radial extent was necessary. For this purpose the W7-Code was used [Wer09]. The code calculates the vacuum magnetic field configuration for WEGA. Figure 4.11 shows magnetic flux surfaces for WEGA. The place of the last closed flux surface (LCFS) was the decisive factor in designing the diagnostics. If the loops reached the LCFS they would act as an additional limiter with a continuous deposition of particles and heat at the diagnostics. This would probably lead to a breakdown of the system after some time.

Due to the fact that the magnetic loops are totally enclosing the plasma one has to look for the toroidal plane with the largest distance between the vessel and the



(a) Open state of the system to enable flipping of both bows ensuring the lead through in vacuum vessel (b) Zoomed figure showing cable route in the shielding pipes

**Figure 4.9:** 2nd magnetic diagnostic system consisting of two diamagnetic loops (white cables) and the internal Rogowski coil (red cable)

LCFS. At WEGA these are the toroidal positions of

$$\phi_C = 54^\circ + 72^\circ \cdot n \quad (4.5)$$

with  $n = 0..4$ . In each of these planes two ports having a diameter of 80 mm at the poloidal angle of  $\theta = \pm 45^\circ$  are located (C-ports). In the desired plane the flux surface show up as a vertical ellipse which can be seen in figure 4.12.

The LCFS in limiter configuration of WEGA is defined by the poloidal plane where the plasma ellipse lies horizontally. Here the flux surfaces touch the vessel on the magnetic high field side in the case that no other diagnostic or heating components hits the plasma. Due to the fivefold toroidal symmetry this plane is shifted by  $36^\circ$  in each field period with respect to the vertical ellipse. At WEGA 5 planes with a vertical plasma ellipse are existing. However, one is occupied by the Heavy-Ion-Beam-Probe, on by the ECRH, and further two by the vacuum pump system so that the selection was limited. In WEGA notation the chosen plane is port plane 14 with the C-ports 14(+) and 14(-) where a radial space of  $b = 42$  mm is available.

However, this radial space for the diagnostics is reduced by their finite toroidal extent. Or in other words radially larger diagnostics - these are the compensation coil and the 2-loop system - have to be mounted close to plane 14 whereas the other diagnostics can be installed in the vicinity on the left or right hand side of this plane. Thus, the available radial space for the farthest mounted diagnostic is reduced to  $b = 31$  m.

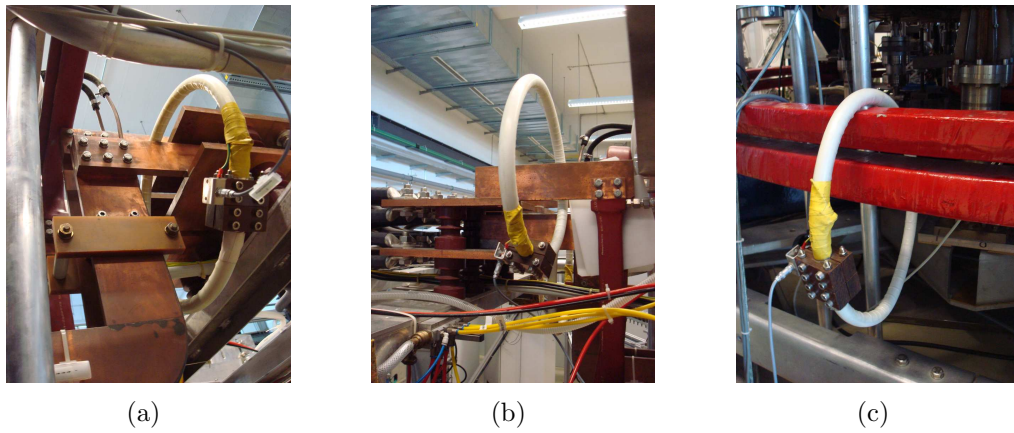


**Figure 4.10:** Rogowski coils to measure the toroidal (a), helical (b) and vertical (c) field coil current

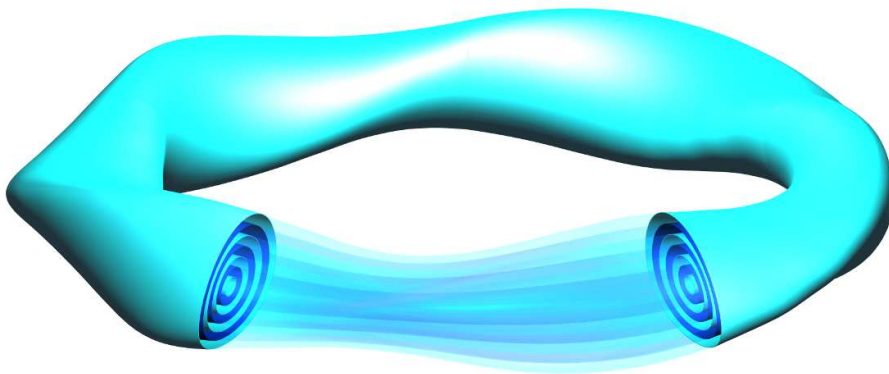


**Figure 4.11:** Example of magnetic flux surfaces at WEGA for  $\tau \approx 0.2$

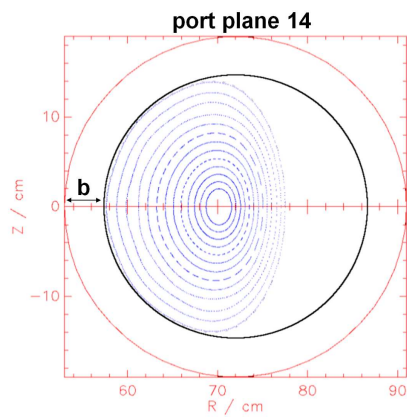


**Figure 4.12:** Magnetic flux surface including the LCFS for the planes with a vertical plasma ellipse

### 4.1.7 Alignment of Magnetic Diagnostic

In order to minimize the influence of plasma current and helical magnetic field on the diamagnetic loops as well as their compensation coil, it is necessary to mount these diagnostics exactly in a poloidal plane. In order to locate these planes, experiments without plasma have been performed with a pure helical field coil current to adjust the loops step by step until a minimum in the signal was achieved. In a poloidal plane of an ideal plasma currentless stellarator, the helical field components cancel out each other. In case of WEGA with its 4 helical coils the total flux should be zero since the current direction alternates between the individual coil packets. However, the winding law has to be considered, since the coils are squeezed on the high field side as well as slightly expanded on the low field side. The squeezing and expanding of conductor packets result in a finite net toroidal field of the helix. Thus, it was not possible to reach a zero flux with a pure helical magnetic field. The optimum alignment was determined using a pure toroidal field. Since the poloidal plane is perpendicular to the flux of a pure toroidal magnetic field, the signal coming from diamagnetic loops has to become a maximum in this case.

The influence of the finite permanent flux area at the port feed through, where the wires could not be twisted was negligible. To this end, the feed through was turned in different directions during measurements of the vacuum magnetic field.

After performing all these adjustments, the final setup of diagnostic inside the vacuum vessel can be seen in figure 4.13.



*Figure 4.13: Magnetic diagnostics mounted inside the vacuum vessel where the access is only possible through the existing ports. The picture was also made through one port.*

## 4.2 Digital Integrator

In the following chapters the different optimizations and performance improvements of the digital integrator are shown. These have been necessary since the wanted signals, e.g. for the determination of the diamagnetic flux, needs high resolution. Therefore, a totally new reconstruction and integration algorithm has been developed and is explained in 4.2.1. Furthermore, adjustments of the hardware settings have also been performed which are described in the sections 4.2.2 - 4.2.4.

### 4.2.1 Reconstruction and Integration Algorithm

Magnetic signals for the determination of the plasma energy or the plasma current are important for the control of discharges. Therefore, a digital integration which will also be used at W7-X needs to meet real-time requirements, i.e. requirements on accuracy and speed [HWM<sup>+</sup>08]. For this purpose the previous integration algorithm has been improved with respect to accuracy without the loss of speed. The newly developed algorithm which will also be utilized at W7-X is now continuously used for magnetic measurements at WEGA. The algorithm is described in the following.

The raw signal of a magnetic measurement is chopped in the earliest possible state. The clock frequency used is 373 Hz. The arguments for this choice are explained in section 4.2.3. The chopped signal will be referred to as pseudo signal in the following (top plot in figure 4.14). The polarity of the clock signal is used to generate a mask signal having the values (+1) and (-1). For the time period of the switching process it is set to zero (middle plot in figure 4.14). The start of the switching process is defined by the rising and falling edge of the clock signal. If one of these flanks is detected, a number of samples depending on the time period needed for the switching process will be set to (0). An analysis of the switching process and the following integration leads to the result that for a sample rate of 50 kHz and a maximum cycle time of 80  $\mu$ s four samples need to be set to (0). If a larger number of samples are set to (0), too much of the signal is lost and the interpolation performed later becomes more imprecise. On the other hand, a reduction of the number of samples has shown that in this case samples which are already influenced by the charge injection of the chopper stage would be used.

In the next step, a zero line needs to be determined to remove a linear drift later. Ideally, the chopping process of the raw signal mirrors the magnetic diagnostic signal along this zero line, when the polarity of the clock signal is (-1). Therefore, knowledge about this line is of importance for the reconstruction of the raw signal and the integration performed later. The line can be determined by considering the chopped signal before flux changes are induced from the experiment, e.g. before ramping up the main field. During this calibration period the chopped signal can be assumed to be equally distributed around an ideal zero. However, due to the signal path [Wer06] after the integration card (amplifier, ADC), the chopped signal may oscillate along a different value.

In order to compensate the linear drift of this offset value, a regression line using all

non-zero samples of the calibration period is determined. Then the determined regression line will be subtracted from the pseudo signal so that the zero line matches the x-axis.

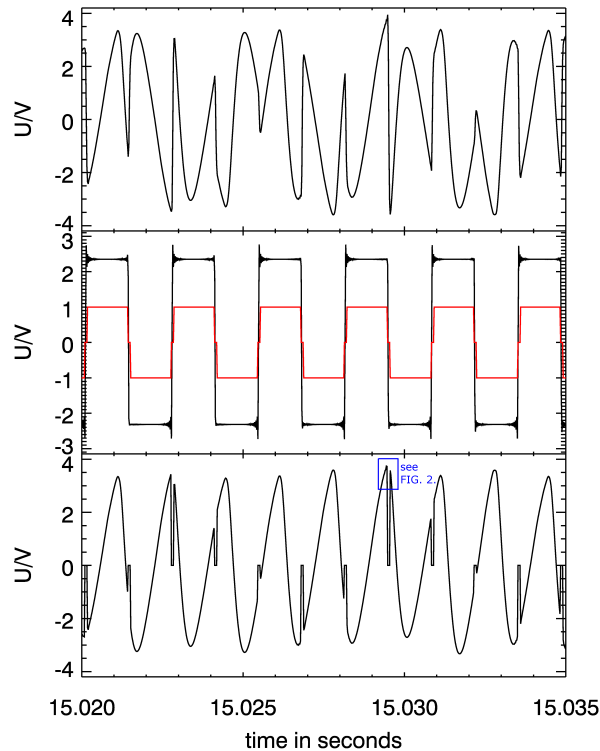


**Figure 4.14:** Top: raw signal coming from magnetic diagnostics after the chopping process; middle: integrator clock signal (black) and generated mask signal (red); bottom: raw signal multiplied by mask signal

In the next step, the pseudo signal is multiplied by the mask signal to reconstruct the original raw signal up to the samples which have been set to zero during the switching process (bottom plot in figure 4.14). These samples will be called switching gap in the following. An interpolation scheme needs to be used to recover the values lost by the switching process. In order to keep the calculation time for the interpolation small (real-time requirement for W7-X and other experiments), only linear regressions will be used (figure 4.15). Three regression lines are used, two constructed from points on the left and right of the switching gap and a third crossing the gap. The first regression line  $f_l$  is defined by the last three samples located before the switching gap and is denoted as left regression line, whereas the second straight line  $f_r$  is given by the first three samples after the switching gap (right regression line). An additional direct line  $f_d$  is created by connecting the two samples on the edge of the switching gap. Three cases have to be distinguished depending on the location of the point of time at which the regression lines  $f_l$  and  $f_r$  intersect. In the first two cases the intersection point is located on the left (before) and the right (after) of the switching gap, respectively.



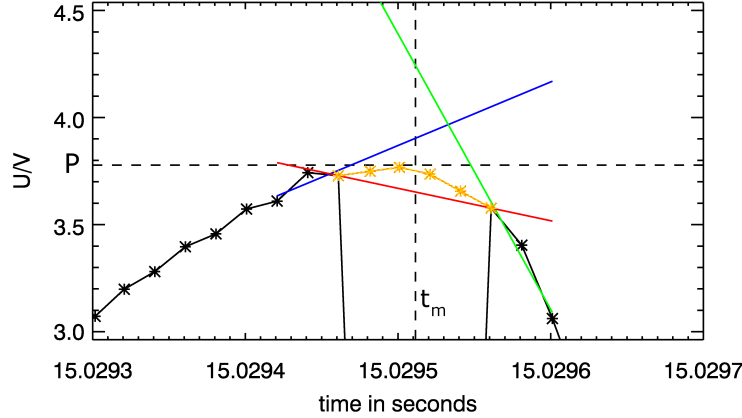


**Figure 4.15:** Interpolation (orange curve) of the missing samples due to the switching process of the digital integrator by means of a left  $f_l$  (blue) and a right regression line  $f_r$  (green) as well as a direct line  $f_d$  (red)

These cases result if the signal before the gap compared to the signal after the gap has a vertical shift or a different curvature. In the third case the left and the right regression line cut each other within the switching gap. For the first two cases and the third case different interpolation schemes will be used. In order to distinguish the cases and for using them in the interpolation scheme the midpoint  $t_m$  of the switching gap is considered (figure 2). The relation of the functional values of the three regression lines at  $t_m$  allows an easy distinction of the cases. This is described by the conditional function A.

$$A = \begin{cases} 1 & , \text{ if } \text{sign}(f_l(t_m) - f_d(t_m)) = \\ & \text{sign}(f_r(t_m) - f_d(t_m)), \text{ (crossing outside)} \\ 0 & , \text{ else (crossing inside)} \end{cases} \quad (4.6)$$

In the case of "outside-crossing" the direct line  $f_d$  is used for interpolation. In the other case a new interpolation function using a polygon with three points, defined by the last point before the gap, a point P at  $t_m$  and the first point after the gap, will be identified. The related function value of P is determined by the mean value at  $t_m$  of  $f_d$  and the regression lines  $f_l$  or  $f_r$  depending on which line is closer to  $f_d$  at  $t_m$  (figure 4.15). This defines the second condition given by

$$B = \begin{cases} 1 & , \text{ if } |f_l(t_m) - f_d(t_m)| \leq \\ & |f_r(t_m) - f_d(t_m)| \\ 0 & , \text{ else} \end{cases} \quad (4.7)$$

where B is (1) when the left regression line is closer to the direct line and B is (0) when the right line is closer, respectively. Therefore, the final condition for the point

P used for the interpolation is

$$P(t_m) = \begin{cases} \frac{1}{2}(f_l(t_m) + f_d(t_m)) & , \text{ if } B = 1 \\ \frac{1}{2}(f_r(t_m) + f_d(t_m)) & , \text{ if } B = 0 \end{cases} . \quad (4.8)$$

Under the conditions at the WEGA stellarator (sample rate of 50kHz, temporal magnetic field ripple of 600Hz), the use of three samples has been found to be sufficient for an accurate determination of the linear regressions for the lines  $f_l$  and  $f_r$ , and thus provides enough accuracy for the following interpolation. The scheme showed good robustness, in particular in cases of steep flanks at the switching gap. The values of the interpolated signal are summed to get the integral curve. A linear drift of this integrated signal may occur caused by continuous summation of an offset in the raw signal. As a zeroth order compensation, a straight line determined during the calibration period time is used, and their function values are continuously subtracted from the integrated signal. Figure 4.16 shows a comparison of the results of the old[[Wer06](#)] and new algorithm. As it could be seen, the old

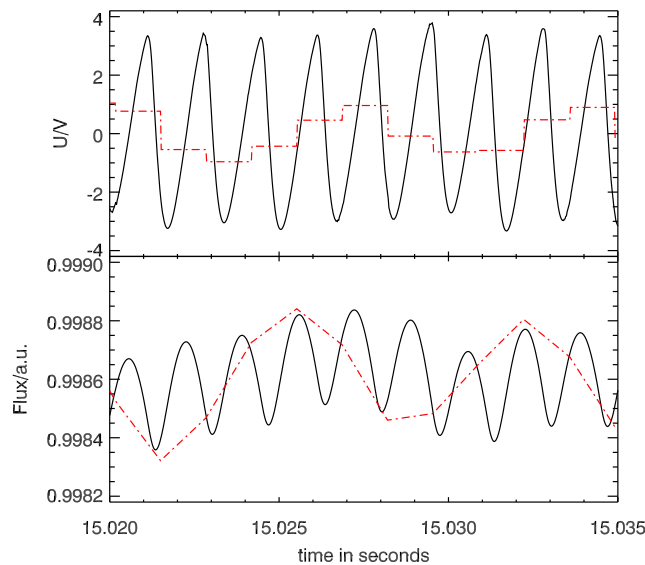


**Figure 4.16:** Comparison of the integrated (bottom) and reconstructed raw signal (top) between the newly developed code (black solid line) and the prior used code based on an average process (red dash dot line)[[Wer06](#)]

algorithm reduces the time resolution of the signal as it averages the raw signal with half of the clock frequency defined by the digital integrator to determine the missing samples. Therefore, spurious aliasing effects which occur with the old integration do not occur by using the new algorithm (figure 4.16 bottom). Figure 4.17 shows the resolution for a 0.5 T WEGA field pulse detected by a diamagnetic loop. The mentioned 600 Hz as well as a 100 Hz ripple can be identified.

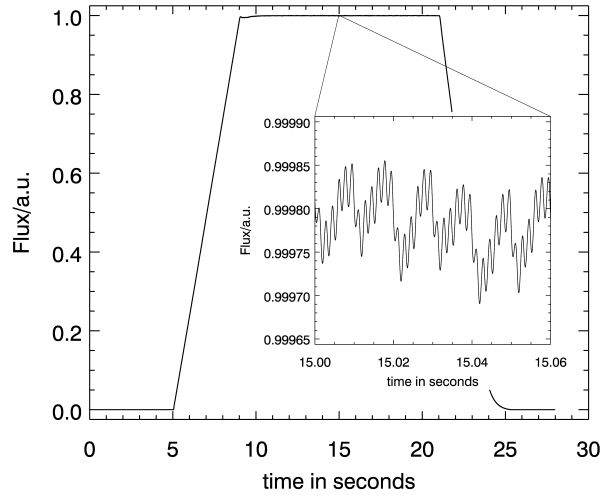


**Figure 4.17:** High temporal resolution of the integrated signal showing a WEGA field pulse and the temporal magnetic field ripple

### 4.2.2 Suppression of Leaking Voltages

The difference between the signals from diamagnetic loops and compensation coils representing the diamagnetic flux was estimated to be in the order of  $10^{-5}$  relative to signal itself. Therefore, minimal leaking effects, which were already detected in the order of  $10^{-3}$ , led to large errors.

In order to realize qualitative plasma energy measurements through determining the diamagnetic flux, two signals on one integrator board could not lie between each other. Hence, free intermediate channels needed to be introduced.

The chosen pin configuration of the different integrator boards is shown in figure 4.18. Here, channel 2 and 4 at the boards 1 and 2 are free (or have to skip since they have a technical fault) to avoid the possible leaking effects between signals measured by the diamagnetic loops or compensation coils.

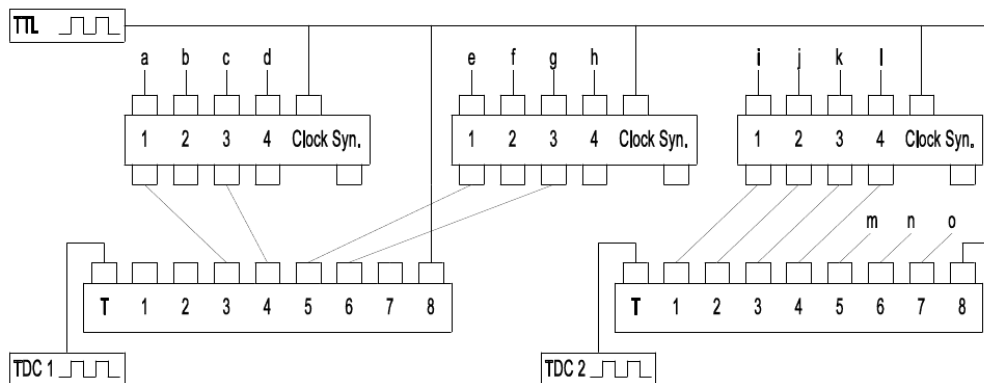


**Figure 4.18:** Pin configuration of the intergrator boards

**Table 4.4:** Signal at the different channels of the integrator board and ADC

Pin	Signal	Pin	Signal
a	Diamagn. loop	i	Rogowski coil for $I_{pl}$ (external)
b	free	j	Rogowski coil for $I_{pl}$ (internal)
c	Compensation coil	k	Rogowski coil for $I_{TF}$
d	free	l	Rogowski coil for $I_{HF}$
e	2-Loop (large dia. loop) 181	m	Loop voltage
f	defect	n	Gyrotron forward power
g	2-Loop (small dia. loop)	o	Sniffer signal
h	free		

### 4.2.3 Clock Frequency Optimization

As a consequence of the high temporal resolution the clock frequency with the period  $t_{clock}$  of the digital integrator has to be adjusted appropriately to avoid beat frequencies induced by the magnetic field ripple from the power supplies having itself a period of  $t_{mfr}$ . For this purpose the ratio

$$k = \frac{t_{mfr} - t_{clock}}{t_{mfr}} \quad (4.9)$$

has to be an irrational value.

In case of WEGA the magnetic field ripple has a frequency of 600 Hz. The quartz at the integrator boards allows clock frequencies of 100 Hz, 1 kHz, 10 kHz and 100 kHz resulting in rational values of  $k$ . Therefore, the digital integrator has been synchronized externally. The chosen frequency is 373 Hz.

The beat frequency may occur due to the interpolation process in the reconstruction and interpolation algorithm. This process is most error-prone when the interpolation takes place for time segments showing a maximum or a minimum in the signal with steep gradients on their edges. If the raw signal is continuously chopped at these periods the error in the integrated signal, e.g. in form of beat frequencies, becomes maximal. This fault will occur, if the clock frequency is an integer multiple of the field ripple frequency.

### 4.2.4 Amplifier Setting

Depending on the amplitude of the raw signal the amplifier in the digital integrator needs to be adjusted to use the dynamic range of the following 24 bit ADC.

It has to be taken into account that the output stage of the digital integrator cannot supply a signal with an amplitude higher than four volt. Above this value the amplifier saturates. Thus, a wrong amplification would occur, leading to a constant four volt signal at the output stage of the digital integrator. One consequence of this saturation can be seen in case of different long magnetic field ramps, used at the beginning and the end of a discharge, and hence a different flux change  $\dot{\Phi}$  leading to

different amplitudes in the flux signals is measured by the magnetic diagnostics. If the signal saturates during the ramp the integral flux curve does not reach the zero line after the discharge again, as shown in figure 4.19

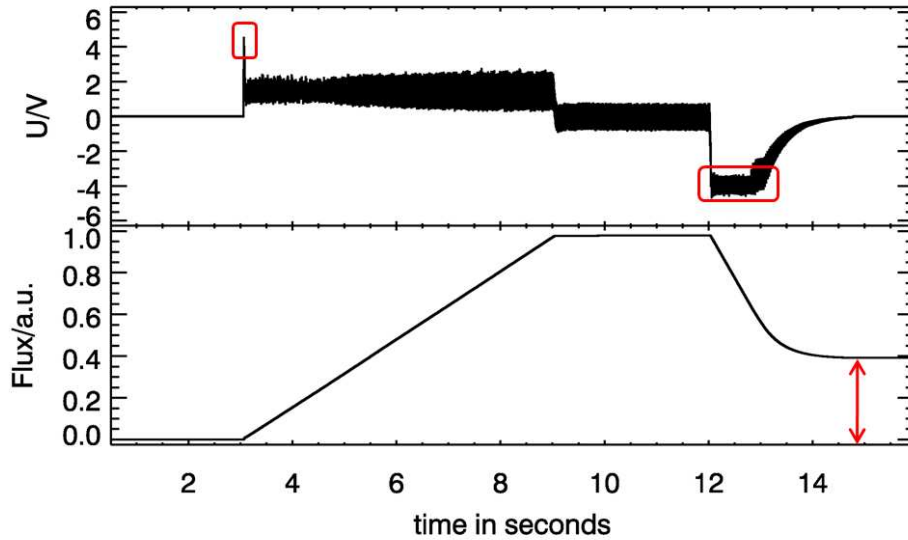


**Figure 4.19:** Saturation of the amplifier (red boxes in the top) leading to errors in the flux measurements (bottom)

But, nevertheless this kind of “ramp” saturation played a minor role since the signal at the flat top of the magnetic field was the important physical part. On the other hand, for the calibration of the diamagnetic diagnostics (determination of factor  $D$  and  $k$  for equation (3.11) and (3.15)) a saturation of the amplifier had to be obviated.

### 4.3 Data Acquisition and Processing

Concerning the data acquisition, the signal path displayed in figure 4.1 should be considered again. The values measured by the magnetic diagnostics and chopped by the digital integrator are detected by 24 bit analog-to-digital converter (National Instruments PXI-4472). The sample rate was chosen to 50 kHz so that processes in the range of tenths of milliseconds could be detected without producing too large data files. The technical data of the analog-to-digital converter can be found in [NI]. The detected values were saved in the already existing data base system developed for W7-X which is referred to as Objectivity data base [HWM<sup>+</sup>08].

The mayor difference compared to the conventional WEGA data archive system is that the discharges and hence the data base does not rely on discharge numbers anymore. The Objectivity data base system is based on absolute time stamps. Thus, the absolute time stamps have to be mapped to WEGA’s relative time stamps in order to allow comparison with other diagnostics.

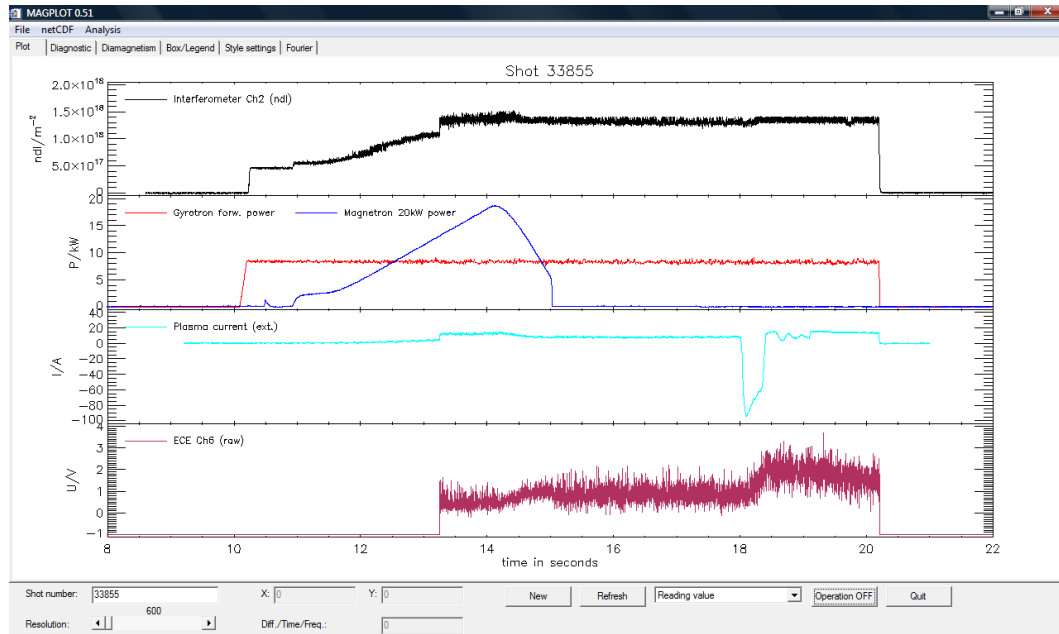


**Figure 4.20:** Interactive user interface of the program MagPlot used for data processing of the signal measured by the magnetic diagnostics as well as other diagnostics

For comparison and evaluation of the measured signals with other diagnostics an IDL program has been written. So far this program contains more than 9500 lines and works interactively. It involves among others the opportunity to perform a specific offset and drift compensation as well as a Fourier frequency filtering. Additionally, different signals can be simultaneously processed with each other. This is necessary for instance in determining the diamagnetic flux. The interactive user interface is shown in figure 4.20.

Furthermore, the program contains the function of reading out the data of the Objectivity data base system and doing, depending on the signal, different operations. These are for instance reconstruction if the signal is chopped, an integration or an offset compensation. The chosen data will be sorted regarding an allocation and saved in the particular netCDF files. The control interface is displayed in figure 4.21.

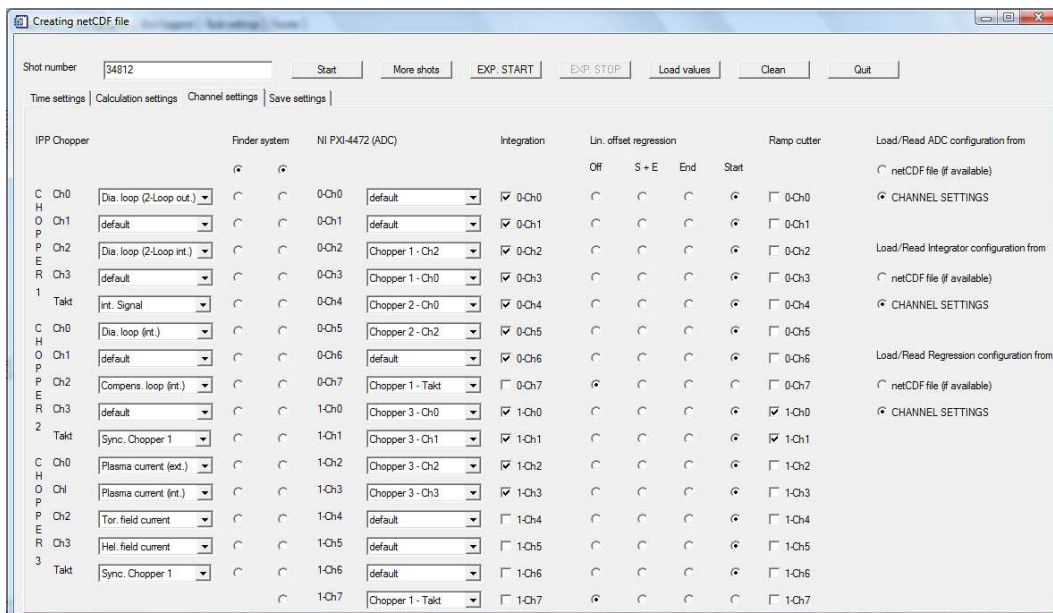


**Figure 4.21:** Interface to control the different digital integrator and analog-to-digital converter channels in order to convert the data, written in the Objectivity data bank system, into netCDF files

## 5 Experimental Results

After assembling the diagnostics a calibration was necessary for the different magnetic loops whose realization and results are described in section 5.1. The subsequent sections are categorized depending on the heating system and therefore the related current drive concept occurring during the discharge. In section 5.2 the influence of electron cyclotron waves with a frequency of 28 GHz on current drive are described. The results by additional use of a non-resonant microwave at 2.45 GHz are shown in section 5.3 followed by the influence of electrostatic Bernstein waves on current drive in section 5.4. In section 5.5 measurements utilizing the transformer are presented.

Lastly, experiments on the determination of the plasma energy and pressure in Bernstein wave heated plasmas are shown in section 5.6.

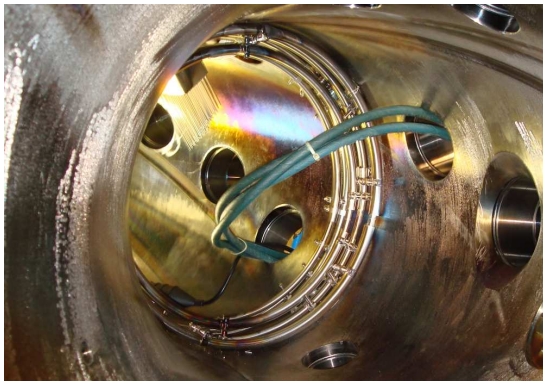


## 5.1 Calibration

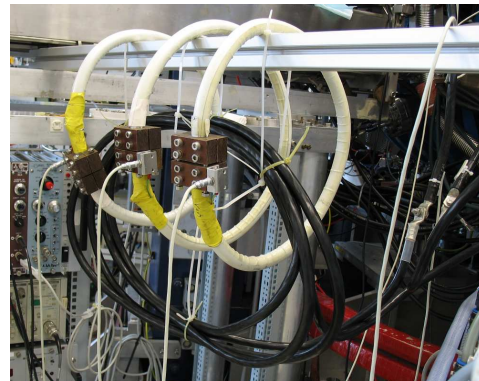
In chapter 3.1 it was shown that every magnetic flux pervading an inductive magnetic loops causes a voltage at the cable ends. Since the origin of the magnetic flux is different for the diamagnetic loops and the Rogowski coils two separate calibrations have been performed. For the first one, toroidal magnetic fields were generated and measured whose averaged value is well known from code calculations. In the second case the magnetic field caused by plasma current pervading both Rogowski coils in plasma operation has been simulated by use of a conductor with a known current driven by power supplies.

### 5.1.1 Setup for Calibration of Magnetic Diagnostics

Regarding the calibration of the diamagnetic loops and compensation coils no further setup was needed. However, in order to calibrate the Rogowski coils a conductor has been put into the vacuum vessel. For this purpose, the conductor has been lead through two free ports close to the plane where the Rogowski coils are located. This can be seen in figure 5.1(a).



(a) Calibration of the Rogowski coils by means of conductor in the vacuum vessel



(b) Calibration of the Rogowski coils used for measuring the toroidal, helical and vertical field coil current

**Figure 5.1:** Setup used for calibration of the different Rogowski coils

The current in the conductor was provided by two power supplies (REGATRON TopCon) connected in parallel series, which can produce a maximum dc current of 500 A. This conductor was also applied for the calibration of the external Rogowski coils used for measuring the toroidal, helical and vertical magnetic field coil current. Since these Rogowski coils are usually measuring magnetic fields caused by current changes of more than 3000 A/s the calibration conductor was lead through the coils several times to get flux changes similar to the standard operational regime. This setup is shown in figure. 5.1(b).

### 5.1.2 Results

For the calibration of the Rogowski coils the power supplies were used to generate a trapezoid current function leading to a magnetic field with the same trapezoid shape. Here, the difference between the plateaus  $B_{cal}$  (seen in figure 5.2) was determined. Knowing the amplitude of the calibration current, which can be given with accuracy of 1.0 % from the manufacturer values an absolute calibration factor can be determined for the different Rogowski coils. Here, data were averaged over 75 measurement cycles. The final calibration values are listed in table 5.1. A change in the position of the conductor inside of the vessel lead to a change in calibration factor by up to 2.9 percent, which may be caused by changes in the winding density along the coil.

**Table 5.1:** Calibration factors showing value for measured current per integrated unit for the different Rogowski coils

Rogowski coil for	Calibration factor
Plasma current (external)	3.14 ( $\pm 0.12$ ) A/i.u.
Plasma current (internal)	18.48 ( $\pm 0.72$ ) A/i.u.
Todoidal Field current	3.12 ( $\pm 0.12$ ) A/i.u.
Helical Field current	3.14 ( $\pm 0.12$ ) A/i.u.
Vertical Field current	3.02 ( $\pm 0.12$ ) A/i.u.

In order to determine the diamagnetic calibration factors  $D$  and  $k$  defined from equation (3.11) and (3.15) a toroidal magnetic field scan was performed at WEGA. The measured flux signal had the same trapezoid shape as during the Rogowski coil calibration.

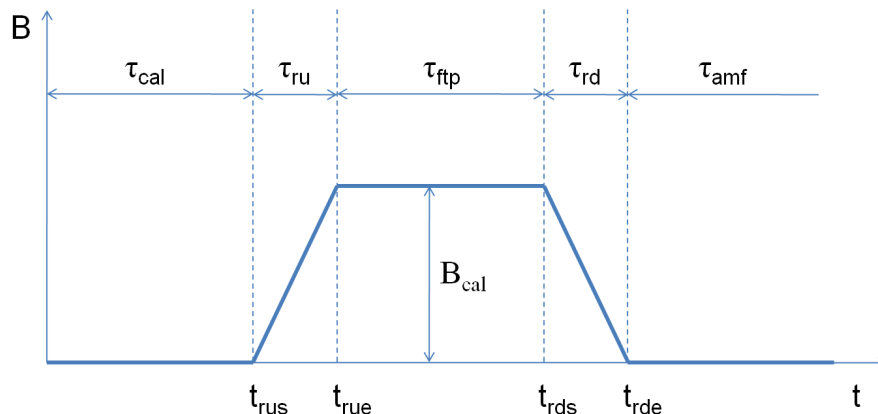


**Figure 5.2:** Time development of the magnetic field used for calibration of the inductive diagnostics

Here, the time period  $\tau_{cal}$  was used for offset calibration of the magnetic diagnostics. This time was chosen to 5 seconds to get a sufficient offset compensation.

The ramping up time  $\tau_{ru}$  as well as the ramping down time  $\tau_{rd}$  of the magnetic field were 4 seconds. The duration of the magnetic flat top phase was  $\tau_{ftp} = 4$  s.

If the signals of the diamagnetic loop and compensation coil as well as both diamagnetic loops from the two-loop system are divided by each other the calibration factors  $D$  and  $k$  can be determined. The difference in the flux is plotted for 200 mT for the conventional system consisting of the diamagnetic loop and the compensation coil. Here, using  $D = 4.03868$  both signals could be subtracted from each other with a relative resolution of  $3 \cdot 10^{-5}$ . The deviation during the ramping up and ramping down time may be caused by a different mutual inductance between the diagnostics and the field coils. However, this region is not necessary in order to detect flux changes during the magnetic flat top phase later.

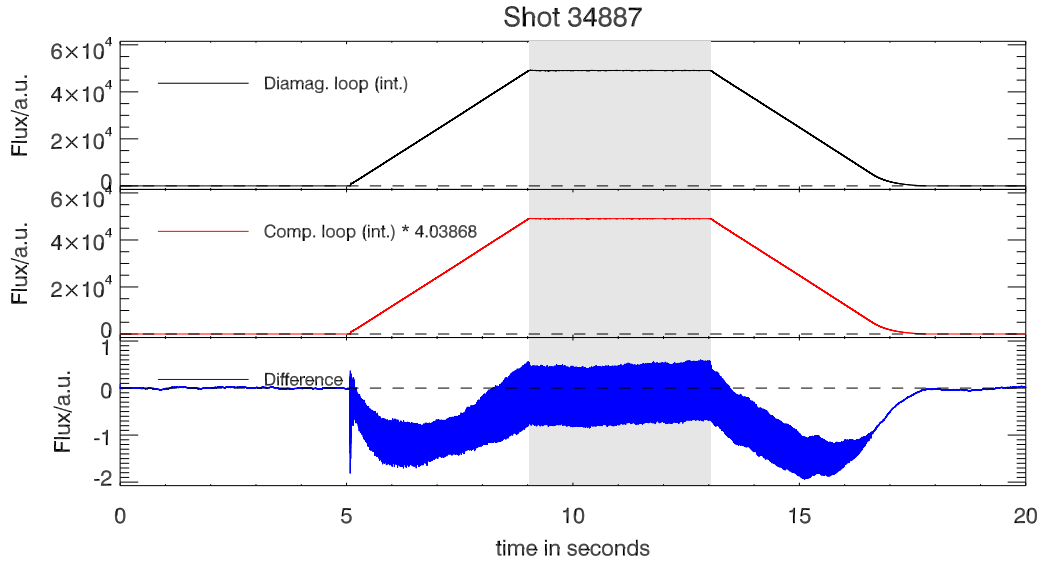


**Figure 5.3:** Difference of the flux signals of the diamagnetic loop and compensation loop allowing a relative resolution of  $3 \cdot 10^{-5}$

In figure 5.4 the compensation factors  $D$  and  $k$  are shown for a variation of the magnetic field. Here, a slight change could be observed which may be caused by a change in the force acting on the magnetic loops inside the torus. This force may lead to a movement of the loops and therefore to a change in their flux area. With increasing the magnetic field the force becomes stronger.

In this work discharges for pressure measurements were performed at 0.47 T. Thus, calibration factors of

$$D = 4.0390 \pm 0.0001 \quad (5.1)$$

$$k = 1.27706 \pm 0.00003 \quad (5.2)$$

are used.

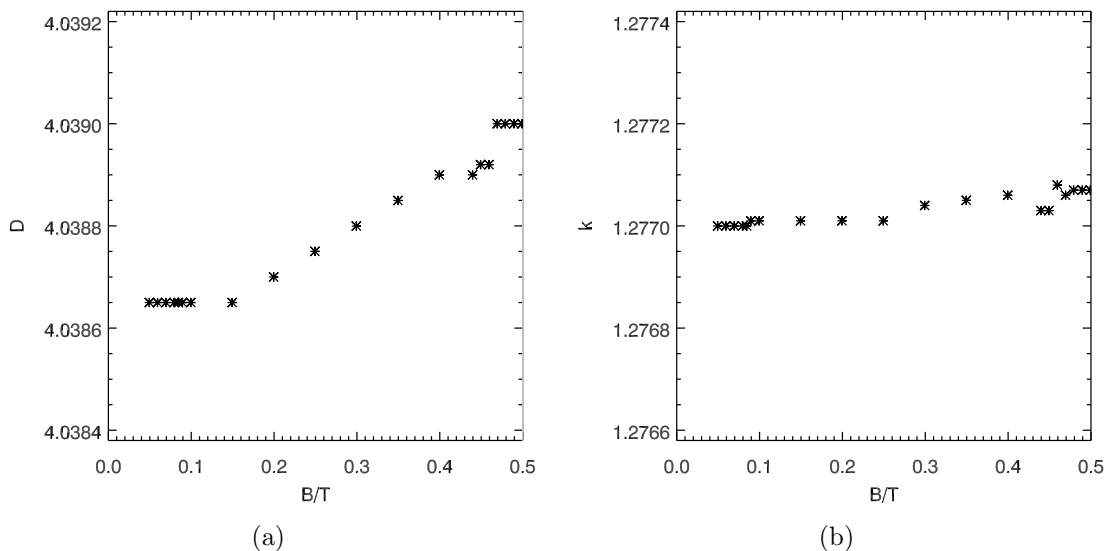


**Figure 5.4:** Change in the calibration factor  $D$  and  $k$  with respect to a change in the toroidal magnetic field

As mentioned in section 4.1.7 the winding law of WEGA's helical coils causes different influences on the diagnostic loops. Since the factor  $D$  and  $k$  were derived with respect to the toroidal magnetic field, the influence of the poloidal field through the helical coils leads to the fact that the subtracted signal of both diamagnetic systems differs from during the magnetic flat top phase. Consequently, in order to investigate flux changes caused by the plasma the subtracted curve needs to be shifted so that the signal vanishes during the magnetic flat top phase without plasma.

Furthermore, thermal drifts of measured signals of the internal diagnostics caused by their warming during plasma operation has to be considered. For example, due to the different warming of both diamagnetic loops in the two-loop system the difference signal will also drift. However, concerning diamagnetic measurements, as seen later in section 5.6, fast changes will be considered so that thermal drifts can be averaged out.

## 5.2 Plasma Currents in Resonantly Electron Cyclotron Heated Discharges

In this section the results from experiments on current drive in discharges using only resonant electron cyclotron waves for plasma ignition and continuous plasma heating are presented. Here, discharges have been performed using the gyrotron with an emission frequency of 27.92 GHz using helium as working gas. The resonant magnetic field was 0.4987 T on the magnetic axis corresponding to a field of 0.483 T on the torus axis. In consideration of figure 5.2 the calibration time  $\tau_{cal}$  was 3 seconds and the resonant magnetic field was stationary between second 7 s and 21 s. The plasma ignites at second 10.2 s and extinguishes at 20.2 s.

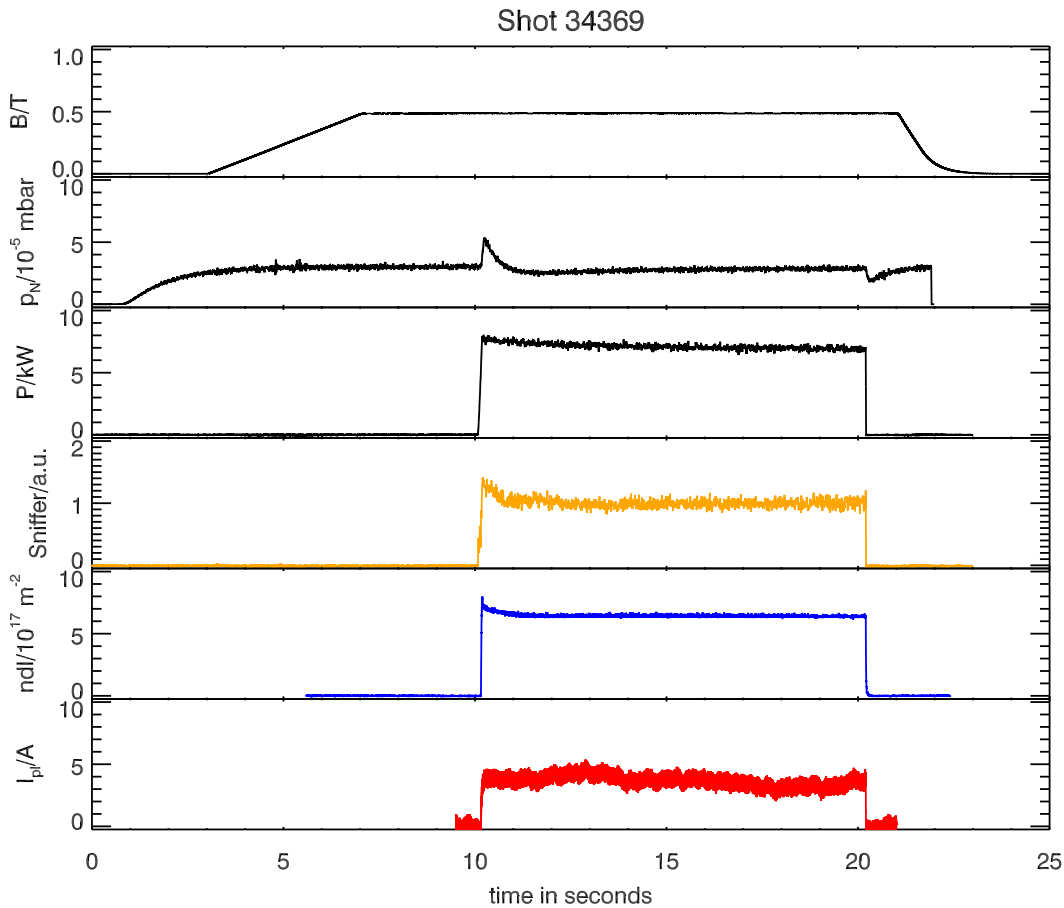


**Figure 5.5:** Time traces of a ECRH helium discharge. From top to bottom are shown: the magnetic field  $B$  on the torus axis, the neutral gas pressure  $p_N$ , the forward power of the gyrotron  $P$ , the sniffer signal, the line integrated density  $ndl$  and the plasma current  $I_p$

In figure 5.5 time traces of a typical helium discharge are shown. Here, with a resolution of  $\pm 0.5$  A determined by the influence of the magnetic field ripple a current could be detected with an amplitude of 4 A. In order to determine the source of this

current different parameter studies have been performed. First of all the influence of the ECRH power on the plasma current was examined. Here, the gas flow was kept constant which should ideally lead to a constant neutral gas pressure  $p_N$  in order to suppress changes in the driven current by a variation of  $p_N$ .

The power was varied from 3 kW, which was necessary for a reproducible plasma ignition and stable discharge, up to 8.5 kW, limited by the gyrotron. The results from this scan are shown in figure 5.6(a). The plasma current increased from 0.7 A to 5.1 A, almost following the development of the line integrated density. For these discharges the neutral gas pressure continuously decayed by about 20 %.

In a second scan,  $p_N$  was varied by changing the gas flow at constant forward power of  $P_{gyr} = 8 \pm 0.5$  kW. In figure 5.6(b) it can be seen that the plasma current as well as the density were almost constant for  $p_N \approx 1 \dots 3 \cdot 10^{-5}$  mbar. Thus, the decrease of  $p_N$  during the power scan can be neglected and the change of  $I_{pl}$  in figure 5.6(a) can be attributed to  $P_{gyr}$ .

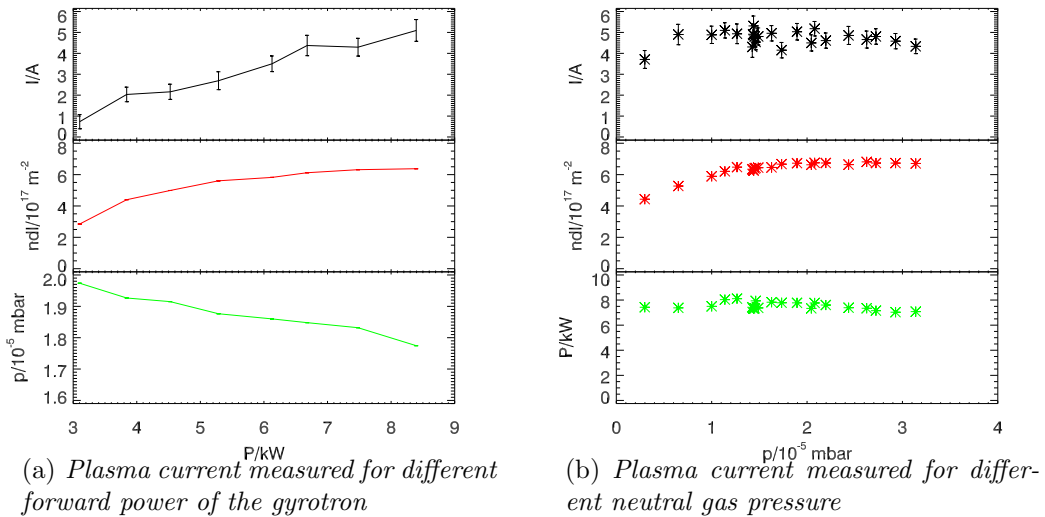


**Figure 5.6:** Neutral gas pressure and ECRH power scan for plasma current measurement

As the detected current was expected to be driven by ECCD, the influence of the radiation angle of the microwave was examined. Here, a variation of this angle at constant neutral gas pressure and forward power took place. The radiation angle could be varied between  $50.0^\circ$  and  $80.5^\circ$  limited by the technical setup of the heating mirror. Figure 5.7 shows the resulting current.

Variations of  $I_{pl}$  can be attributed to a change in the coupling efficiency of the microwave at the different angles. Therefore, the amount of absorbed power changes leading to a change in  $I_{pl}$  as shown before.

In case of an electron cyclotron driven plasma current a relative larger change in the plasma current had been expected, since with reaching a perpendicular radiation an effect of the loss particle cone leading to an Ohkawa current should become noticeable as described in section 2.4.3. With further increasing the angle - over

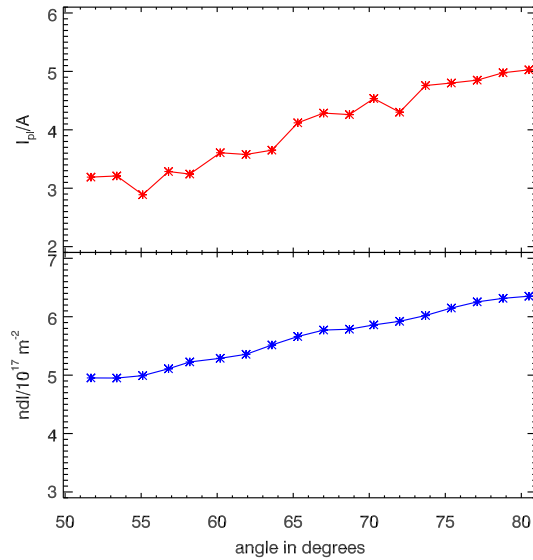


**Figure 5.7:** Plasma current measured for different radiation angles of the microwave

90 degrees - the direction of the ECCD should change. However, this could not be investigated through the limited movement of the heating mirror.

A possible reason for not having a strong radiation angle dependency on the plasma current with respect to the electron cyclotron current theory can be explained with the low single path absorption at WEGA due to small optical depth. Due to multi-path absorption of the ECRH wave no preferred ECCD direction exists. This is sketched in figure 2.8. Consequently, the measured current is assumed to be driven by internal sources as the pressure gradient driving the bootstrap current.

In order to verify this assumption the direction of the toroidal magnetic field was inverted keeping all other discharge parameters constant. The flux surface topology could also be kept constant by additionally inverting the helical coil currents. This inversion should have no influence on an EC current. However, a current with a reversed direction could be detected as shown in figure 5.8. This is a strong indicator for bootstrap currents.

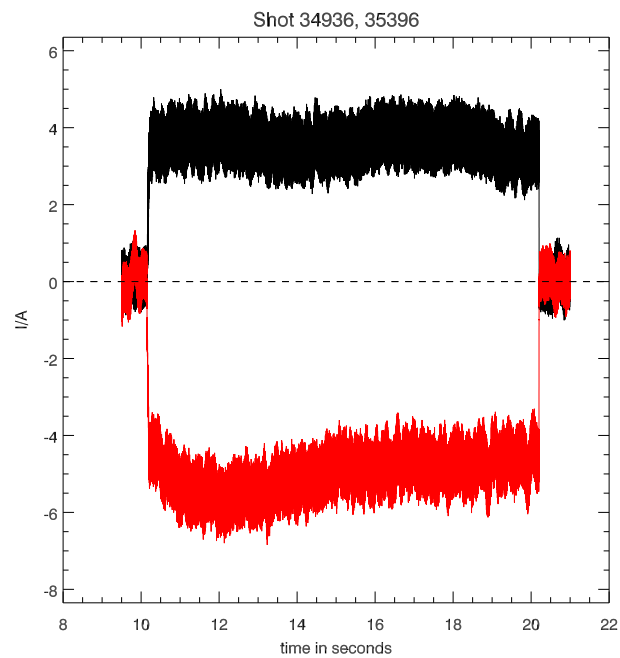


**Figure 5.8:** Influence of the bootstrap current by changing magnetic field direction from clockwise (black) to anti-clockwise (red) leading to change in plasma current direction



### 5.3 Lower Hybrid Current Drive Experiments

In this section the influence of microwaves at a frequency of 2.45 GHz on plasma current drive is examined. The temporal evolution of a standard discharge used for this consideration is shown in figure 5.9

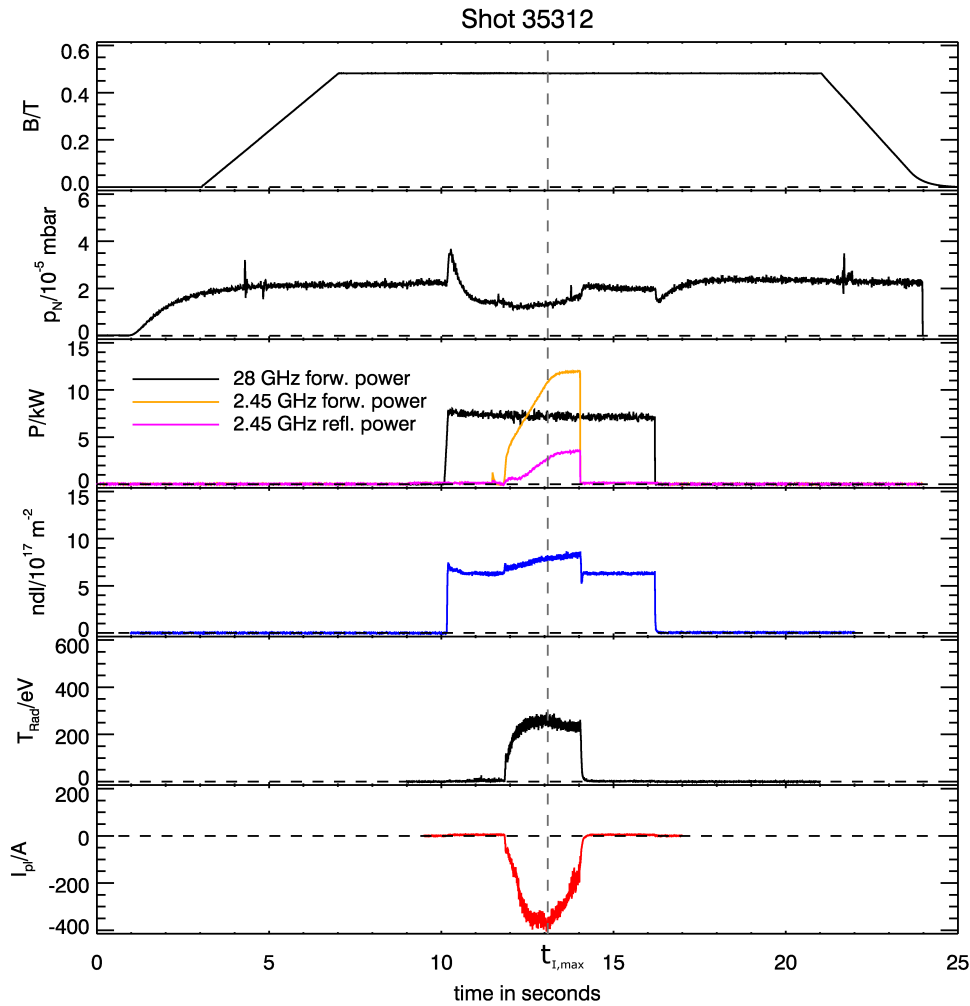


**Figure 5.9:** Time development of lower hybrid current drive discharge

Here, the plasma is ignited at 10.2s and continuously heated by the gyrotron till 16.2s with a forward power of 8 kW at a magnetic field of 0.483 T at the torus axis. From 11.5s till 14s the 2.45 GHz magnetron was additionally used for non-resonant heating and plasma current drive. The following experiments were performed using helium to avoid reaching the cut-off and the related back coupling of the resonant microwaves into the gyrotron. The stationary current of 5 A before and after the magnetron operation is the bootstrap current described previously. The influence of the magnetron emission can be seen in an increase of the plasma density. Additionally, the plasma current changes its direction, which is opposite to the main

toroidal field now. This follows from the preferential  $k_{\parallel}$  spectrum of the LH wave injected into the plasma [Pod06]. The absolute value of the plasma current rises to 386 A using a forward power of 12 kW.

In a first step in the examination of LHCD the forward power of the magnetron was varied at constant gas flow. The peak current  $I_{pl,max}$  reached at a time  $t_{I,max}$  during magnetron operation is plotted in figure 5.10 versus the injected power

$$P_{inj} = P_{for,2.45} - P_{ref,2.45} \quad (5.3)$$

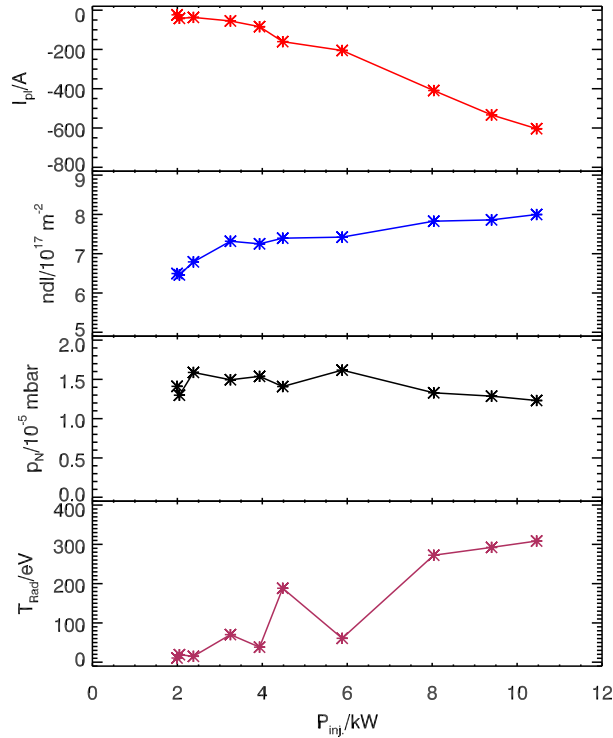


**Figure 5.10:** Plasma current dependence on injected power of radiated waves with a frequency of 2.45 GHz

resulting from the difference of the forward power  $P_{for,2.45}$  and the reflected power component  $P_{ref,2.45}$  coupled back into the magnetron wave guide. However,  $P_{inj}$  does not necessarily correspond to the power coupled into the plasma, since further components of  $P_{inj}$  can be reflected by the plasma and do not penetrate the wave guide again. Due to a lack of diagnostic for the determination of this coupling factor the injected power will be used for further discussions. The peak current at  $t_{I,max}$  was typically reached before  $P_{inj}$  reached its maximum. However, it was chosen since no stationary conditions on a timescale longer than 10 ms could be reached for the plasma current.

The results from this power scan from  $P_{for,2.45} = 2.5...16 kW$  ( $P_{inj} = 2.0...10.4 kW$ ) are shown in figure 5.10. An almost linear relation between the plasma current and the injected power could be determined. The change in the line-integrated and

neutral gas pressure at  $t_{I,max}$  are also shown in figure 5.10.

Before estimating a current drive efficiency from the values shown in figure 5.10 the influence of the neutral gas pressure and plasma density needs to be examined to estimate the boundaries of the efficiency as well as possible errors due to the change of these values during the power variation.

Thus, LHCD experiments were performed at different  $p_N$  realized by a change in the gas inlet. A constant forward power of the magnetron was used with a magnitude of 8 kW. However, due to the different gas inlet and the related changes in plasma parameters (e.g. in plasma density) the coupling of the wave into the plasma changed. This led to a change in the reflected power resulting in a variation of the injected power between 5.2 to 6.3 kW.

For this reason the plasma current, density and neutral gas pressure were measured when the injected power reached specific values in order to compare these parameters with each other. The results are shown in figure 5.11.

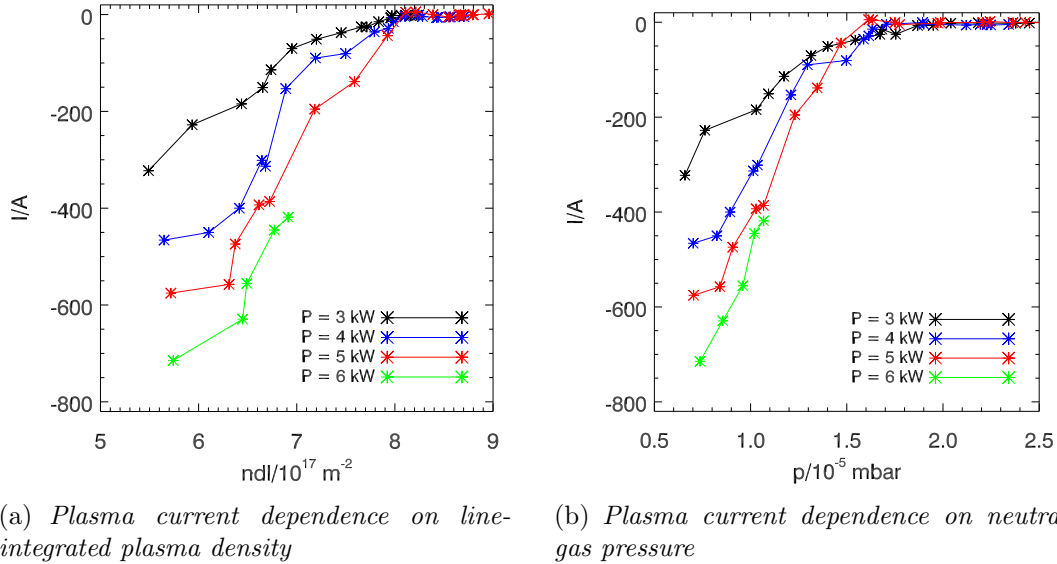


**Figure 5.11:** Plasma current driven by lower hybrid waves for different densities and neutral gas pressures. Different lines corresponding to values taken from different points during the power ramp up time

It can be seen, that the plasma current decreases up to a certain threshold, where it vanishes. The critical neutral gas pressure is  $1.5 \cdot 10^{-5} \text{ mbar}$  which correspond to a critical line-integrated density of  $8 \cdot 10^{17} \text{ m}^{-2}$ . Below this limit a power dependent rise of the plasma current could be measured up to a total current of 750 A for an injected power of 6 kW. A further reduction of the neutral gas pressure below  $0.7 \cdot 10^{-5} \text{ mbar}$  was not possible due to thermal load effects on the technical components inside the WEGA vessel. Here, for example an intensively glowing mirror of the ECRH system was observed during the discharge. Furthermore, the generated X-ray radiation limited experiments with higher plasma currents.

On the other hand above the critical limit no substantial current was driven and

only a slight change in density occurred as seen in figure 5.12 showing a discharge with a maximum in the injected power of 6.1 kW and line-integrated density of  $1 \cdot 10^{18} \text{ m}^{-2}$ .

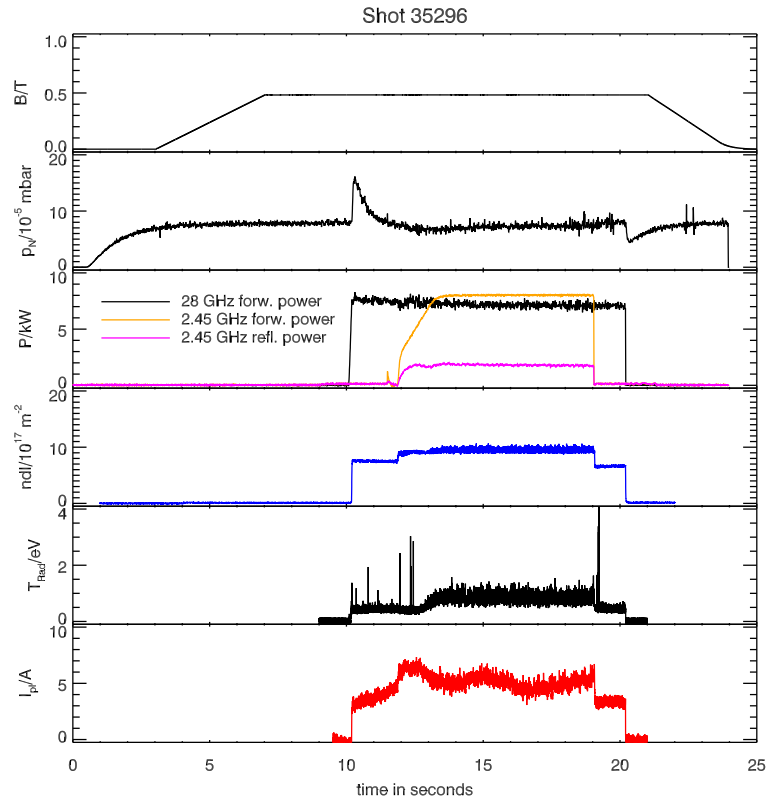


**Figure 5.12:** Plasma current developing for the case having a line-integrated density above  $8 \cdot 10^{17} \text{ m}^{-2}$  during the non-resonant heating phase

The origin of the LH current is - as predicted by theory - caused by the generation of super-thermal particles. This could be confirmed by means of soft X-ray measurements using a pulse-high-analyzer. Here, particle energies in the range of few ten keV were detected during a discharge with  $P_{inj} = 7.5 \text{ kW}$  at a line-integrated density of  $ndl = 7.4 \cdot 10^{17} \text{ m}^{-2}$  and a plasma current of  $I_{pl} = 370 \text{ A}$ . A further proof of super-thermal particles was given by ECE (electron cyclotron emission) measurements. Although these radiation temperature measurements give only access to the electron temperature in dense plasmas with a optical depth of  $\tau > 3$  the results in figure 5.10 can be seen as a qualitative indicator for the existence super-thermal particles [Sta09].

Taking equation (2.56) into account, the current drive efficiency for LHCD in WEGA can be estimated which depends on the plasma density. This has been done for all discharges with an injected power up to 10.4 kW. The results are shown in figure 5.13. Here, a linear decrease of the efficiency with increasing the plasma density was found. Regarding discharges which were performed for the power variation shown above a shift of the curve seems to occur. However, further examinations of

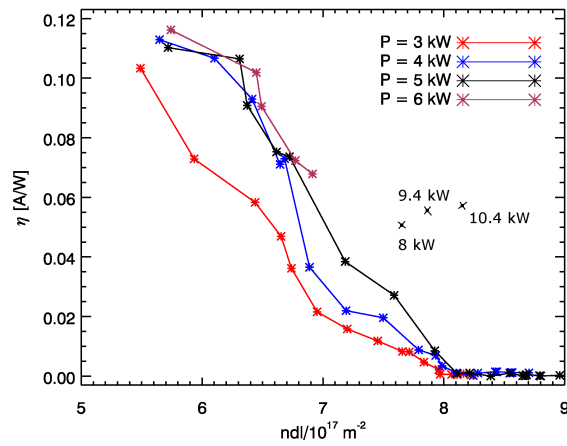


**Figure 5.13:** Current drive efficiency for discharges in helium with a injected non-resonant power up to 10.4 kW

density dependencies at higher injected power were not possible due to the limitations mentioned before.

## 5.4 Plasma Currents in OXB Heated Discharges

In this section the experiments with over-dense plasmas are shown. Here; a mode conversion process, described in section 2.3.2, is used to generate electron Bernstein waves for plasma heating. After describing the temporal discharge development, the results of the plasma current measurements are shown. The plasma parameters in this scenario allowed to determine the plasma energy and plasma pressure at WEGA for the first. These results are shown in section 5.6.

The temporal development of two discharge types utilizing the OXB mode conversion scenario are explained. In case of using helium as working gas the related time traces of the discharge parameters are shown in figure 5.14

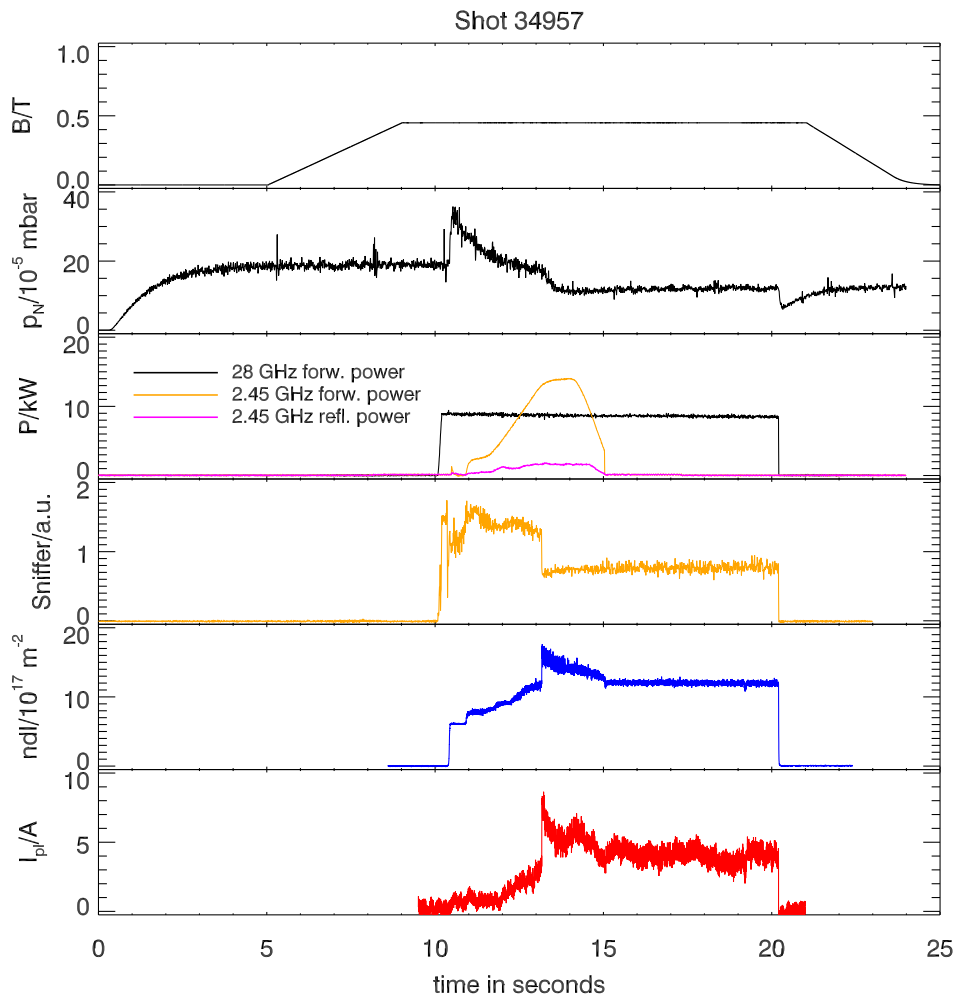


**Figure 5.14:** Discharge developing for the examination of the plasma current and pressure in an OXB heated plasma. From top to bottom are shown: toroidal magnetic field  $B$ , neutral gas pressure  $p_N$ , forward power of the 28 GHz gyrotron (resonant) and 2.45 GHz magnetron as well as its reflected power, sniffer signal, line-integrated electron density  $ndl$ , and plasma current  $I_{pl}$

The toroidal magnetic field is set to 0.47 Tesla on the axis due to Doppler down-shift of the resonance of the later generated electron Bernstein waves (EBW). The incident angle of the elliptical polarized O-wave is  $55^\circ$  with respect to the toroidal magnetic field. The plasma is ignited with a maximum forward power of 8.5 kW of the gyrotron. Starting from 10.9 s the magnetron is additionally used for non-resonant heating. Above a critical density of  $n_e = 0.97 \cdot 10^{19} \text{ m}^{-3}$  the mode conversion of the O-wave into the slow X-wave and finally into an electrostatic Bernstein wave takes place. This wave heats mainly the plasma now. With reducing the magnetron power starting at 14 s till a final switching off at 15 s the over dense plasma regime can be held by the gyrotron alone till the discharge ends at 20.2 s.

In the other case of using Argon as working gas, an additional heating source like the above used magnetron is not necessary for the OXB heating scenario. Here, through the use of the gyrotron is sufficient to reach the critical density and therefore fulfilling the conditions for the mode conversion.

With the transition in the OXB regime the sniffer signal, which is an indicator for the non-absorbed microwave radiation on the torus, collapses caused by a better absorption and therefore better absorption efficiency [GCH<sup>+</sup>01]. This can be seen at 13.2 s in figure 5.14. Additionally, an increase in the channels of the EBE diagnostic is detected, which measures the electron Bernstein wave radiation leaving the plasma under a preferential angle and using the inverse mode conversion process (BXO). The central channels measure radiation temperatures of more than 10 keV. This temperature can now be associated with the electron energy of the super thermal particles due to a high optical depth for Bernstein wave emission [Sta09].

However, from Langmuir probe measurements performed at second 19.5 the electron temperature of the bulk plasma can be estimated with 10 eV. Therefore, and for energetic reasons the mentioned radiation has to come from a small population of the super-thermal particles.

These Langmuir probe measurements are also used to cross check the averaged plasma pressure determined by the magnetic diagnostics.

The main focus lies in the stationary OXB regime regarding the current drive measurements. For plasma pressure measurement however the fast changes like the entrance and exit of the OXB regime are important, since long term influences (e.g. through warming of the diagnostics) change on much larger time scale.

In order to investigate the influence of OXB heating on current drive two almost identical discharges have been considered. In one case the gas flow was reduced by about 6 percent with respect to a second case so that it was not possible to reach the over dense state, as seen in figure 5.15.

In comparing both discharges the relative slow plasma current rise from 12 s till short before reaching the OXB transition and the slow decrease from 15 s till 16.5 s can be traced back to the influence of the magnetron. However, these current changes are not a matter of lower hybrid current drive, since the direction of the plasma current equals the  $k_{\parallel}$  spectrum. However, this spectrum of the radiated microwave should lead in case of LHCD to plasma current in the opposite direction, as seen in section 5.3. Thus, these plasma current changes must be caused by a

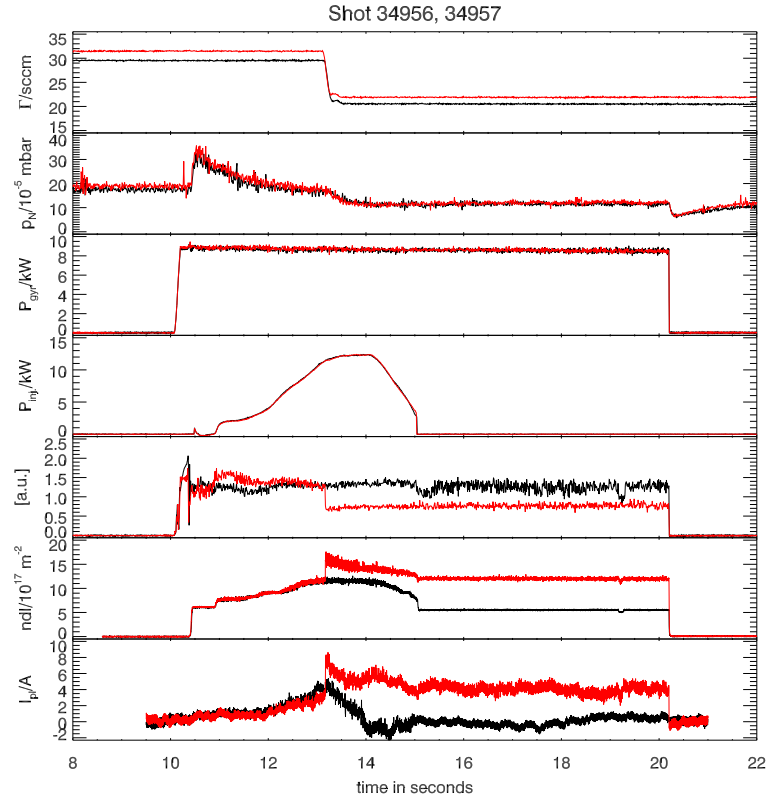


**Figure 5.15:** Plasma current measured for two different discharges which distinguish by a change in the gas inlet by 6 percent resulting in reaching the OXB phase for 34956 (black) compared with 34957 (red)

pressure gradient driven bootstrap current.

With the instantaneous transition into the OXB regime, an additional current change of 5 A occurs. This current component can be held till the end of the discharge. However, the plasma current predicted by ray-tracing calculations for the OXB phase was more than one order of magnitude higher compared with the measured results [Urb09]. Further investigation needs to be done here.

In the next step a parameter analysis for the stationary OXB phase was performed. In order to exclude perturbations from the non-resonant magnetron heating only the pure gyrotron heating phase was investigated for the analysis. However, the parameter range, where a stable OXB phase without the magnetron could be realized, was quite limited in case of helium discharges. Therefore, the magnetron was used over the whole length of the discharge.

Additionally, further discharges have been performed in argon, where no additional heating source was necessary and where the accessible parameter range was much broader - at least for the variation of the gas flow and therefore the neutral gas pressure. The plasma current dependency on the neutral gas pressure and line integrated density is shown in figure 5.16. Here, for both gases by not using the magnetron the current and density are almost constant over a wide range by varying the neutral gas pressure. By additional use of the magnetron the plasma current



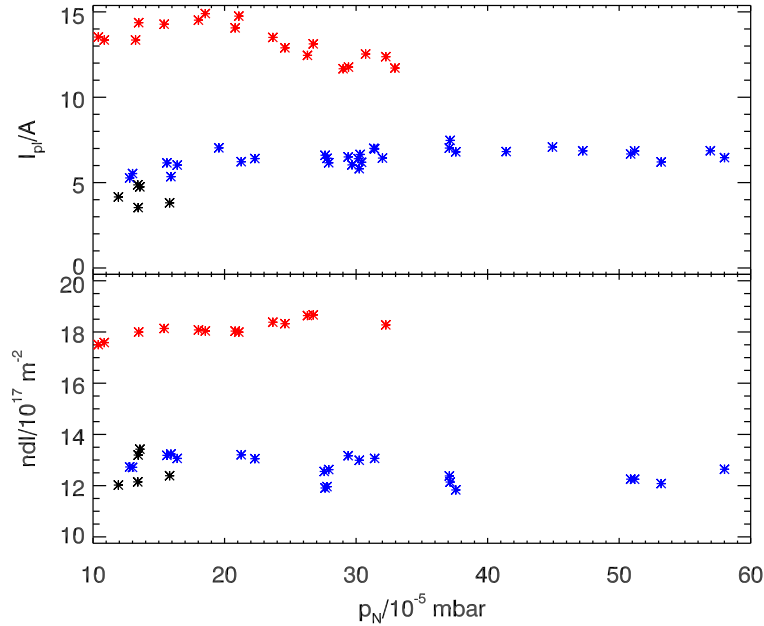


**Figure 5.16:** Plasma current in OXB regime in dependency on neutral gas pressure for discharges with argon (blue), helium (black) and helium by additional use of the magnetron (red)

rose by a factor of 1.5 - 2 and the density by a value of around 1.5, too. Comparing the current measured in OXB discharges without the magnetron with respect to the results from the X2 heating scenario (section 5.2) no significant difference is observed.

Furthermore, power modulation experiments, as can be seen in figure 5.17 for an argon discharge, have been performed to examine the transition into the OXB phase. Here, argon as well as helium experiments have been investigated. By using argon the gyrotron forward power was varied from 8 to 3 kW from 11 to 19 s.

Using a modulation frequency of 13 Hz, 110 cycles have been realized in one discharge in order to average over the different cycles to suppress disturbing magnetic field ripple influences and warming drifts of the inner Rogowski coil. The change of the gyrotron power was used as trigger signal here. With this method it is also possible to average over cycles of more than one discharge in order to improve the signal/noise ratio. The results for a consideration of two discharges are shown in figure 5.18. Here, with switching off the gyrotron power a collapse in the plasma current and radiation temperature occurs while the density changes on a longer time scale. Here, the stationary plasma current in the non OXB phase (gray shadowed regime R2 and R4) was set to zero in order to show the change with respect to the OXB phase (gray shadowed regime R1 and R3). The time difference between the signal of the internal and the external Rogowski coil can be traced back to the influence of the skin effect of the vessel. Consequently for fast changes the use of the internal Rogowski coil takes advantage since their faster response. However, still after using 220 cycles for averaging a influence of the magnetic field ripple can

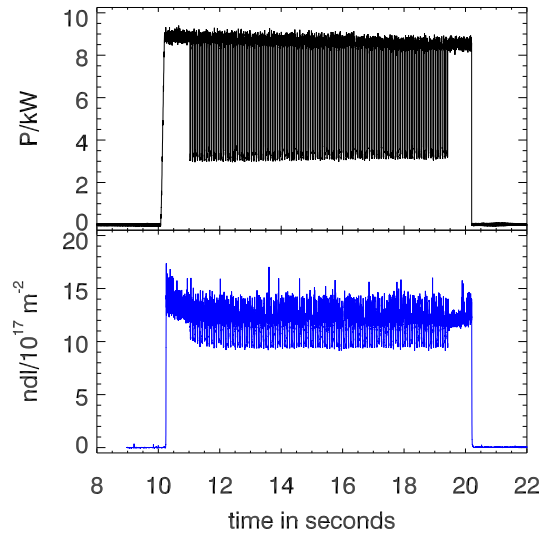


**Figure 5.17:** Power modulation of the gyrotron to investigate the plasma current behavior during OXB transition

be seen there. With leaving the OXB phase the current drops by about 4 A within one millisecond. On the other hand to reach the OXB phase a time of about 18 milliseconds is necessary for the mode conversion and the change of the pressure gradient driving the plasma current.

Performing the same discharges again with helium and the permanent use of the magnetron to satisfy the reaching of the critical density for the mode conversion with each cycle, a frequency of 23 Hz was chosen. Here, 175 cycles in one discharge have been realized, where the averaged signal is shown in figure 5.19. By comparing argon and helium the current signal from the fast internal Rogowski coil drops by 70 percent within 1.2 ms for argon by leaving the OXB phase, whereas for helium 3.3 ms are required for this change. On the other hand for reaching the maximum current in helium 6.5 ms are necessary compared with 15 ms in argon. Thus, investigation of the influence of the magnetron for the faster reaching of the OXB phase combined with keeping the pressure gradient by leaving the OXB phase and therefore a related slower reduction in the plasma current has to be done. Changing the direction of the main toroidal field, like performed for the experiments with purely resonant heating as described in section 5.2, the measured plasma current also changed its direction here. Taking density and temperature profiles measured by means of Langmuir probes, a first approximation of the bootstrap current could be performed using equation 2.69. For an OXB heated discharge in helium without the additional use the magnetron, this cross check leads to a value of 12 A, which corresponds with the order of the measured value by means of the Rogowski coils and supports the fact of driving bootstrap currents at WEGA.

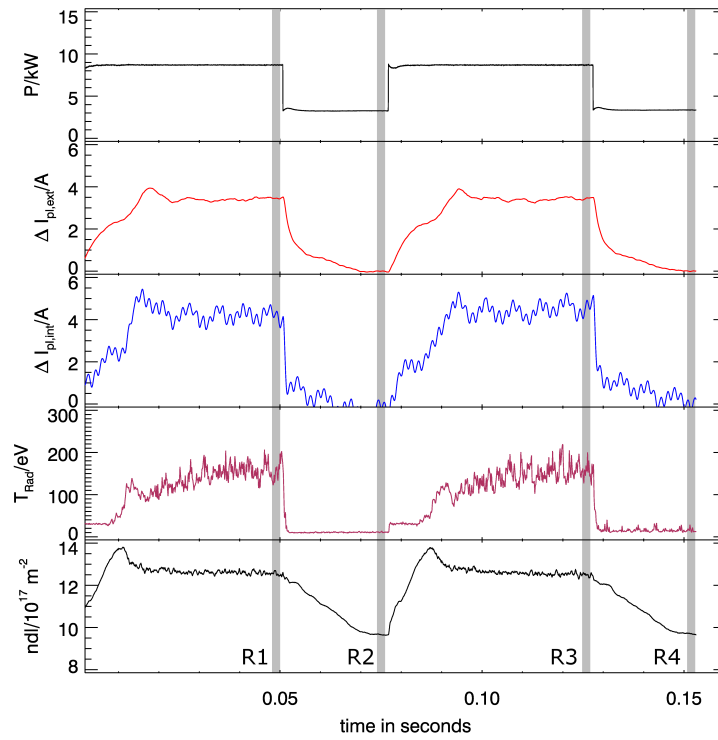


*Figure 5.18: Plasma current change with transition in OXB regime for argon*

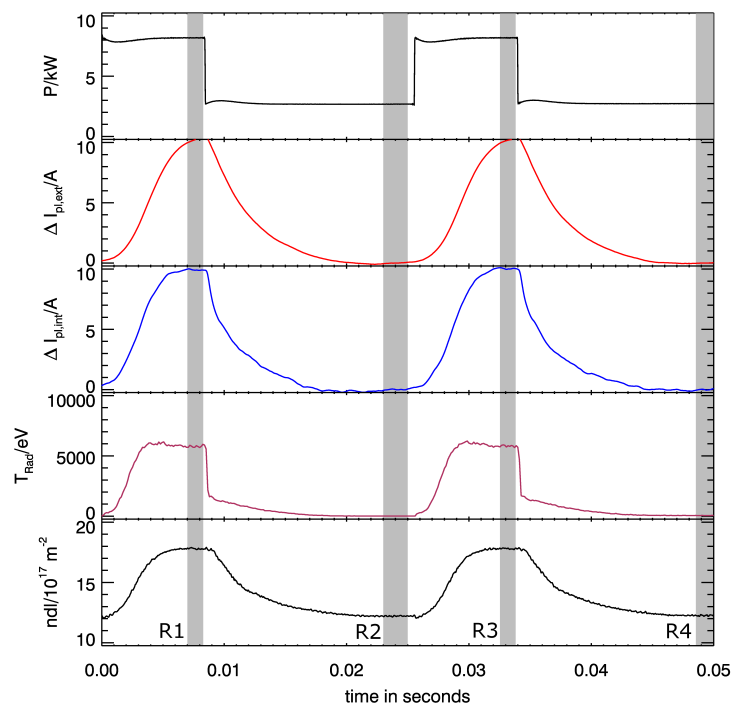


*Figure 5.19: Plasma current change with transition in OXB regime for helium by additional use of permanent magnetron power of 14 kW*

## 5.5 Inductive Current Drive Measurements

In this section the results of experiments with ohmically driven plasma currents are shown. The discharge evolution is similar to the X2-heated experiments described in section 5.2, but with the additional use of the transformer from 17.0 s to 17.4 s. The experiments were performed using helium as working gas. A voltage of 69.57 V was applied to the primary windings leading to a loop voltage of about 1 V.

For different line-integrated densities, realized by varying the gas flow, the plasma current is shown in figure 5.20. At a line-integrated density of  $3.8 \cdot 10^{17} \text{ m}^{-2}$  the current increased up to 660 A. Due to technical problems only the density before driving the ohmic current could be measured. Thus, a possible increase of the density through ohmic heating could not be detected. However, the ohmic heating power of  $P_{OH} < 660 \text{ W}$  is negligible compared with the used microwave heating of 8.5 kW. Furthermore, technical issues lead to a shift of the plasma inside the torus which may have changed the resonant heating and magnetic confinement. For line-integrated densities below  $3.8 \cdot 10^{17} \text{ m}^{-2}$  no measurements could be performed due to the existing X-ray condition.

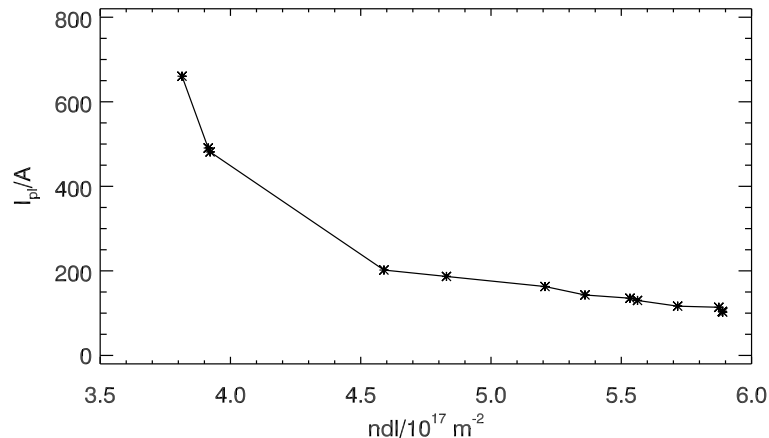


**Figure 5.20:** Inductively driven plasma current for discharges with different densities

The transformer was also used during OXB heating experiments which are described in section 5.4. Here, a plasma current of 93 A could be measured on average at a line-integrated density of  $12.8 \cdot 10^{17} \text{ m}^{-2}$  and a neutral gas pressure of  $7.1 \cdot 10^{-5} \text{ mbar}$ . Using equation 2.75 these values would lead to an average electron temperature in the region of 4.5...7.5 eV, where the uncertainty results due to the unknown ionization grade and measurement tolerances. Langmuir probe measurements could be realized here. A measured temperature profile is shown in figure 5.21. Here, in order to compare the plasma parameter at different toroidal positions a coordinate transformation of the minor radius  $r$  to an effective radius  $r_{eff}$  was applied.  $r_{eff}$  is flux surface label which is defined as the radius of a circle with the same area as the corresponding flux surface. Data were available in this case for  $r_{eff} > 28 \text{ mm}$ .

The profile leads to a volume averaged temperature of 7.2 eV which supports the value determined by the magnetic diagnostics.

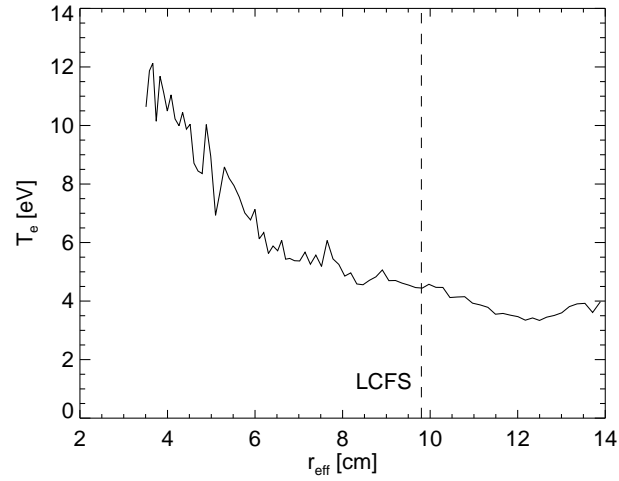


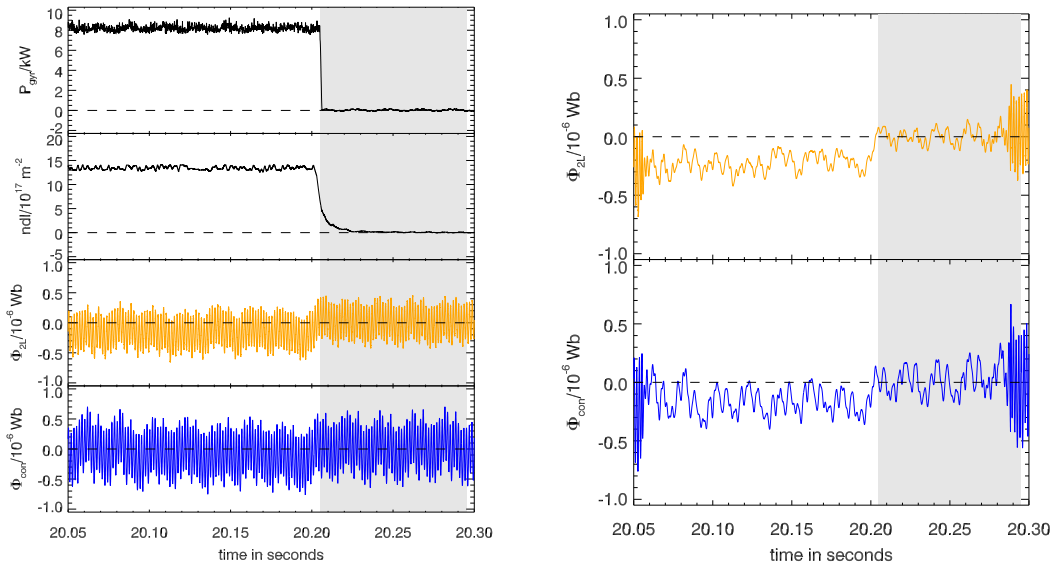
**Figure 5.21:** Temperature profile measured by a Langmuir probe to support the electron temperature determined by means of the Spitzer resistivity

## 5.6 Plasma Pressure Measurements

In this section, results concerning plasma pressure and energies measurements are shown which could be performed for the first time at WEGA. The expected plasma energy in WEGA is in the order of 1 Joule. Any minor perturbation signal like a warming of the coils could lead to effects in the same order but on a relatively long timescale. Therefore, fast changes, like the switching off process, are considered here first. Different experiments will be shown with the aim to exclude several perturbation effects which may cause a signal comparable to the real diamagnetic effect. Then results from power modulation experiments will be explained.

The starting point in this examination is a discharge as shown in figure 5.14. Here, the plasma heating was switched off at 20.2s. In the following the flux change  $\Delta\Phi$  caused by the diamagnetic effect is presented which will later be converted to the plasma energy and pressure. Due to the perturbation effects described in section 5.1 (warming of the diagnostics due to microwave stray radiation) the signal of the flux difference of both diamagnetic systems given by equation (3.12) and 3.16 is set to zero for the time short after the discharge. Hence, the flux caused by the diamagnetic effect is negative as defined in section 2.1.

In the following the system consisting of the diamagnetic loop (16 windings) and compensation coil (19 windings) is referred to as conventional system (index is “con”). The two-loop-system get the index “2L”. In figure 5.22 the switching off process can be seen, with the drop to zero of the forward power and line integrated density.



(a) Leaving OXB phase at second 20.2

(b) Fourier filter for frequencies above 570 Hz is used between 20.06 s and 20.28 s for better flux change detection

**Figure 5.22:** Flux change measured during leaving OXB phase by means of the conventional diamagnetic system as well as the 2-loop system

For a better identification and determination of the flux change, a Fourier filter has been applied from second 20.06 to 20.28, which can be seen in figure 5.22(b), in order to suppress frequencies above 570 Hz caused mainly by the magnetic field ripple. But even without the filter the flux change can be seen in figure 5.22(a). The two coil systems measure an absolute flux change of  $\Delta\Phi_{2L} \approx 2.3 \cdot 10^{-7} \text{Wb}$  and  $\Delta\Phi_{con} \approx 2.0 \cdot 10^{-7} \text{Wb}$ , respectively.

Similar flux changes were observed at a spontaneous loss of the OXB conversion process leading to a fast (ms) drop of plasma parameters. Such a loss may be caused by minor changes in the plasma parameters like  $\iota$  or the gas flow  $\Gamma$ .

In both cases i.e. switching off the plasma and the loss of the OXB phase, the plasma current also dropped on a comparable short timescale. Therefore, a parasitic influence of the current on the flux measurements had to be ruled out. For this purpose, a discharge has been realized analog to the one shown in figure 5.14 but driving an additional inductive plasma current from 19s till the end of the discharge which was directed oppositely compared to the non-inductive current during the OXB phase. Thereby, it was possible to compensate the plasma current at the time when the plasma was switched off. The flux change in this case remained the same as in the case with finite  $I_{pl}$ . Thus, the plasma current can also be excluded as a possible perturbation effect.

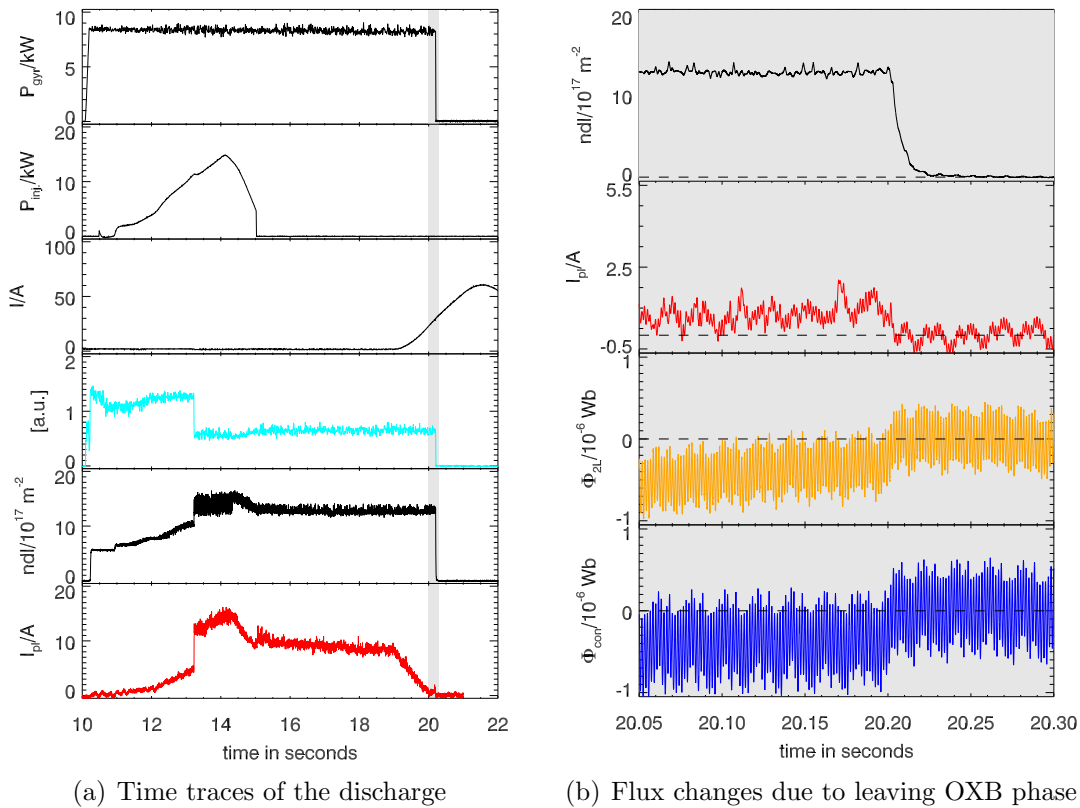


**Figure 5.23:** Ohmic transformer used at the end of the discharge for plasma current compensation

After excluding the possible perturbations, the different terms in equation (2.31) had to be estimated in order to determine the plasma energy and pressure. The use of the cylindrical approximation is justified for the plasma parameters in WEGA [Gei09].

Using the measured plasma current of 10 A and a magnetic field of 0.47 T the paramagnetic term due to the total plasma current leads to a value of

$$\Delta\Phi_{para,I_{tot}} = \frac{\mu_0^2 I_{pl}^2}{8\pi B_\phi} \quad (5.4)$$

$$\approx 1.3 \cdot 10^{-11} \text{ Wb} \quad (5.5)$$

which is 4 orders of magnitude smaller than the measured total flux change given above. The paramagnetic term depending on the plasma current profile determines a flux change of

$$\Delta\Phi_{para,I_{pro}} = \frac{\mu_0 \nu_{vac}}{R} \frac{I_{pl} a^2}{2(m+2)} \quad (5.6)$$

$$\approx 1.5 \dots 5.8 \cdot 10^{-9} \text{ Wb} \quad (5.7)$$

where the peaking factor  $m$  has been varied from 1 to 10 since the current profile is unknown for WEGA.  $\Delta\Phi_{para,I_{pro}}$  is still two orders of magnitudes smaller compared to the measured values. Since the paramagnetic terms are negligible compared to the diamagnetic term, only the latter is taken for further calculation, keeping in mind that the resulting values represent a minimal plasma energy and minimal averaged plasma pressure, respectively. Consequently the plasma energy is given by

$$\begin{aligned} W &= -\frac{3\pi R B_0}{\mu_0} \Delta\Phi \\ &= -2.538 \cdot 10^6 \frac{\Delta\Phi}{[\text{WB}]} \text{ J} \end{aligned} \quad (5.8)$$

with  $\Delta\Phi$  as negative defined flux change in case of diamagnetism. The related pressure is defined by equation (2.29) which results in an averaged plasma pressure of

$$\begin{aligned} \bar{p}_{pl} &= \frac{W}{3\pi^2 R a^2} \\ &= 0.0469 \frac{\Delta\Phi}{[\text{Wb}]} / \left(\frac{a}{\text{m}}\right)^2 \cdot 10^{-2} \text{ mbar} \quad . \end{aligned} \quad (5.9)$$

with  $a$  as the plasma radius. In order to make qualitative statements about the confined energy, power modulation experiments have been performed where the transition from and into in the OXB phase was triggered. Here, the modulation experiments described in section 5.4 were analyzed.

In case of using helium as working gas the critical density, which was necessary to reenter the OXB phase during the high power times of the modulation, could only



be reached by continuous use of the magnetron. Thus the magnetron has been used from 11 s till 20 s with an injected power of about 12 kW. Between 13 s and 19.4 s power modulation of the gyrotron with a frequency of 39 Hz and an amplitude of 5 kW has been performed in order to investigate stationary plateaus regimes.

In figure 5.24 the results from averaging over four discharges with 175 cycles each are shown. Here, the stationary period outside of the OXB regime is used as offset time to compensate thermal drifts of the loops. Thus, this time is taken as zero line so that the change in energy shows up when entering and leaving the OXB phase.

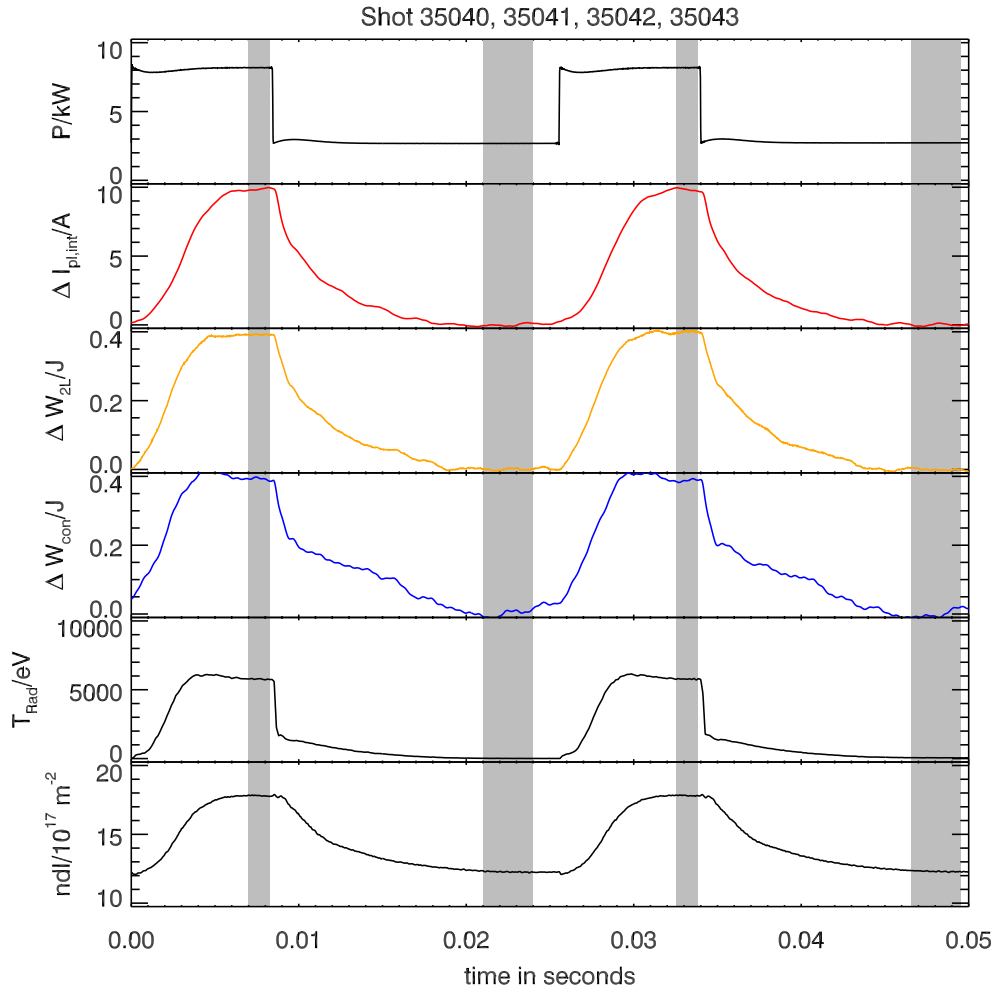


**Figure 5.24:** Plasma energy change measured by the two-loop system as well as the conventional system at the transition from and into the OXB regime for helium with additional use of permanent injected magnetron power of 12 kW

With reaching the OXB phase the density, the plasma current and electron temperature increases. The rise and the drop of the EBE signal ( $T_{rad}$ ) represents the emission of electron Bernstein waves and therefore the start and the end of the OXB regime.

For these magnetron supported helium discharges a change of the energy of  $\Delta W_{2L} = 0.396 \text{ W}$  and  $\Delta W_{con} = 0.390 \text{ W}$  leading to a change in the averaged plasma pressure of  $\overline{\Delta p_{2L}} = 1.93 \cdot 10^{-2} \text{ mbar}$  and  $\overline{\Delta p_{con}} = 1.90 \cdot 10^{-2} \text{ mbar}$  could be determined. The relative difference between both system was below 2%, which supports the accuracy of the given values as they are determined by independent systems.

For Argon discharges performed by the pure use of the gyrotron as heating source an energy change of  $\Delta W = 0.160 \text{ W}$  (averaged over both systems) being equivalent to  $\overline{\Delta p_{pl}} = 0.78 \cdot 10^{-2} \text{ mbar}$  with reaching the OXB could be measured after averaging over 840 cycles as seen in figure 5.25.

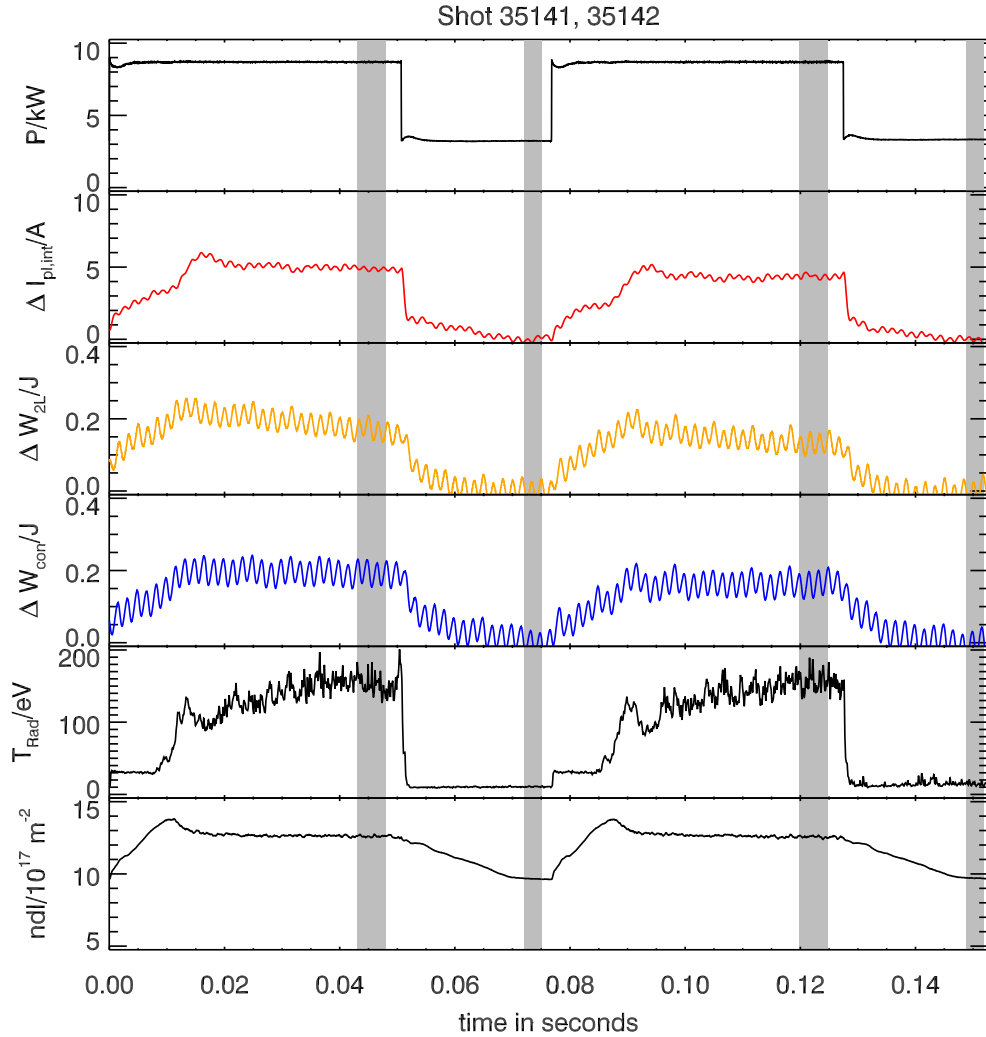


**Figure 5.25:** Plasma energy change measured by the two-loop system as well as the conventional system by the transition from and into OXB regime for argon

The difference in rise and decay time of the plasma parameters between both gases may be caused by the additional use of the magnetron in case of helium as discussed in section 5.4.

For the case of helium discharges it was also possible to determine the total confined plasma energy by investigating the switching off process of the discharges. Here, discharges were chosen with a time evolution as shown in figure 5.14 where the magnetron was only used till 15 s to reach the OXB state. Figure 5.26 shows the result of averaging over 11 discharges. In this case the total plasma energy was  $W = 0.73 \pm 0.2 \text{ J}$  corresponding to an average plasma pressure of  $\bar{p}_{pl} = (3.57 \pm 0.98) \cdot 10^{-2} \text{ mbar}$ . Using equation (2.39) finally leads to an approximation for the plasma beta with  $\beta = 4.1(\pm 1.3) \cdot 10^{-5}$ .

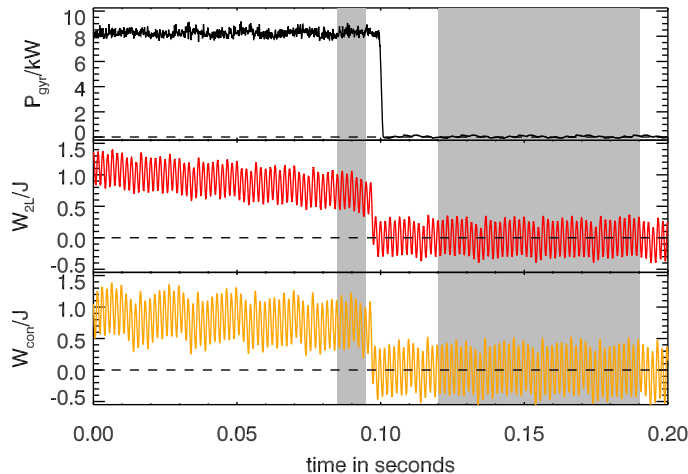


**Figure 5.26:** Plasma energy change measured by the two-loop system as well as the conventional system for the switching off process of the plasma averaged over 11 helium discharges

By means of Langmuir probe measurements a value for the averaged plasma pressure can be determined. Here, equation (2.35) is applied to radial density and temperature profiles. The resulting pressure profile can be seen in figure 5.27.

The volume averaged plasma pressure in this case was  $p_{pl,Langmuir} = 7.1 \cdot 10^{-2} \text{ mbar}$ . This value deviates from the previous one by a factor of about 2. This is, however, still a rather good coincidence due to the unavoidable systematic errors of both diagnostics. In the case of the magnetic diagnostics, for example, parasitic influences of plasma currents on the measurements were minimized but cannot be completely ruled out. Further on, measuring plasma energies in the order of 1 J is a completely new application of diamagnetic diagnostics as these are typically used in fusion experiments with energies in the order of MJ. For the Langmuir probes the data can, at least for the temperature, only be seen as a rough approximation. The data were derived applying a simple model to the probe data which assumes a non-magnetized plasma with a Maxwellian electron energy distribution function. The existence of super thermal electrons may have a significant influence on the probe data as it has already been shown for OXB heated plasmas in WEGA at a low magnetic field using the magnetron [Hor04].

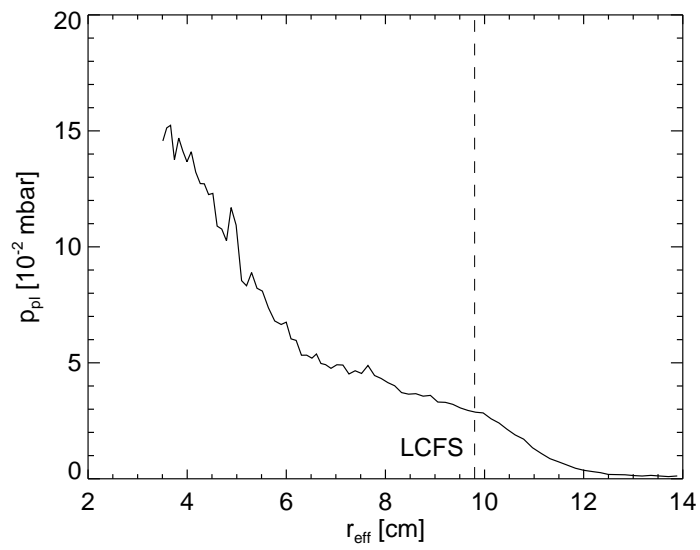


*Figure 5.27: Plasma pressure determined by means of Langmuir probe measurements*



## 6 Summary

Various types of plasma currents can occur in toroidally confined plasmas. On one hand, it is possible to drive plasma currents via external sources, such as a transformer, or through use of microwave radiation. On the other hand, plasma currents can also occur solely due the existence of pressure gradients in the plasma. In both processes it is possible to generate net toroidal plasma currents with a resulting poloidal magnetic field required for the twisting of the magnetic field lines in a tokamak. In addition, pressure-gradient-driven plasma currents flow in poloidal direction, resulting in a weakening of the toroidal magnetic field, which is known as the diamagnetic effect. In this process, the Lorentz force produced by the magnetic field and the diamagnetic current balances the pressure gradient. The poloidal plasma currents are therefore essential for the plasma balance and magnetic confinement.

The aim of the work was to set up a magnetic diagnostic system, and thus to determine and classify the various plasma currents on the WEGA stellarator. In addition, evidence of the diamagnetic effect in WEGA plasmas ought to be given by measuring the plasma pressure and energy. The plasma energy was expected to be in the order of only 1 J.

The diamagnetic diagnostic consists of a compensating coil and a diamagnetic coil installed at a poloidal plane inside the torus. The surface through which the flux passes is placed perpendicular to the toroidal magnetic field and measures the poloidal current components. A relative resolution of flux signals in the region of  $10^{-5}$  was necessary for the detection of the diamagnetic effect. Furthermore, a two-loop system, comprised of two additional diamagnetic coils of different diameter, was developed and integrated in the torus. In this way it was possible to verify measurements of the diamagnetic effect using two independent diagnostic.

The measurement of the toroidal plasma current was accomplished by means of one internal and one external Rogowski coil. These coils represent a bended coil solenoid and also enclose the plasma in a poloidal plane. The loops are sensitive to the poloidal magnetic field that results from the plasma current.

In order to insert the inner diagnostic devices through the existing WEGA ports into the torus and install them here, a multilayered, folding pipe system was designed.

The pipes served to shield the cables from the stray microwave radiation, which had destroyed previous internal diagnostic devices due to their insufficient shielding. In addition, three Rogowski coils from the Wendelstein 7-AS experiment were brought into operation, which measure the currents through the toroidal, helical and vertical field coils.

As these inductive diagnostic methods only measure a signal proportional to the changes in magnetic flux, an integration of the measured values is necessary in order to come to a conclusion on the flux or the plasma current generating this flux. For the purpose of integrating the raw data, the digital integrator developed for Wendelstein 7-X (W7-X), which is based on a chopped input stage and later digital integration, was used. With regard to digital integration, a completely new integration algorithm was developed. This led to an improved signal resolution and a reduction in aliasing effects at the same computing time, enabling real-time processing of the signals. A technical improvement to the measuring electronics was also made, which resulted in further optimization of the signal quality. An experimental determination of the plasma energy was only possible once all of these optimizations, as well as the careful calibration of the diagnostic devices, had been carried out.

A change in magnetic flux due to the diamagnetic current could be clearly detected once it was possible to generate over-dense plasmas at WEGA. This was accomplished by means of mode conversion (OXB) of the incident microwave. The measured change in flux at 0.5 T corresponds to confined plasma energy of around 0.7 J, which equals an average plasma pressure of about  $3.4 \cdot 10^{-2}$  mbar. A value in this region was also confirmed by density and temperature measurements from Langmuir probes. Negative effects, such as thermoelectric voltage, plasma current influences or the warming of the magnetic coils through stray microwave radiation, were clearly ruled out in various tests. Special modulation experiments of the heating performance were also carried out, in which the transition to the over-dense plasma state was investigated.

During the classification of plasma currents generated at WEGA, initial investigations were made in resonant discharges at 0.5 T. It was possible to attribute the current drive during the purely resonant heating phase to internal plasma currents, the so-called bootstrap currents. In this process, the incident angle of the heating microwave was varied, and the direction of the primary magnetic field was reversed. The latter resulted in a complete reversal of the toroidal plasma current, which can only be explained by the bootstrap current.

The additional use of non-resonant heating through radiation of a 2.45 GHz microwave caused a significant increase in the current drive. The plasma currents generated in this mode can be attributed to the lower hybrid formalism, which is characterized by the generation of super thermal particles. It was possible to clearly verify these particles by independent diagnostics. By exceeding the critical neutral gas pressure of approximately  $1.5 \cdot 10^{-5}$  mbar, it was possible to completely suppress this type of plasma current drive.

---

For measurements taken below this critical value, in which plasma currents up to approximately 1200 A were measured, a current drive efficiency with a maximum value of 0.11 A/W was established.

Plasma currents were also investigated on OXB-heated plasma. On entering the over-dense plasma regime, and with the associated instantaneous increase in density, a rise in current of around 7 A was measured which was also attributed to the bootstrap current. It was not possible to obtain clear evidence of current drive from electron Bernstein waves from these experiments.

In the final stage, inductively-driven currents were investigated using the transformer on the WEGA stellarator. From the current measurements, and the loop voltage creating these currents, it was possible to determine an average electron temperature. This was consistent with the Langmuir probe measurements, and was within the range between 5 and 10 eV for OXB heated plasmas.

It was thus possible to add two further standard diagnostics to the ongoing experiment operations at the WEGA stellarator. Substantial improvements were also made to the digital integrator designed for the W7-X. Furthermore, it was possible to clearly determine bootstrap and lower hybrid plasma currents on WEGA as well as, for the first time, a plasma energy of 0.7 J.





## 7 Outlook

With the opportunity to measure plasma currents with a accuracy of 1 A at WEGA, specific investigations of the bootstrap current can be performed at WEGA. For this purpose, the combination of the results from Langmuir probe measurements, which give access to the required plasma pressure profiles, is essential.

Further potential exists through a possible realignment of the heating mirror system used for ECRH heated discharges. Through this, an asymmetric propagation of Bernstein waves could occur, which may lead to detectable Bernstein wave-driven plasma currents.

The knowledge gained through working with the digital integrator could also be used to further setup additional magnetic diagnostics as well, as the related data acquisition and analysis. For instance, mini-Rogowski coils that penetrate the plasma could be used to determine the plasma current profile. This would also help to detect local plasma currents flowing in different directions. Another opportunity to get access to these profiles would exist by means of an array of poloidally arranged Rogowski coils.

Finally, the developed reconstruction and integration code, which is required by the digital integrator technique, can be implemented in the analysis routines of the magnetic diagnostics at W7-X.



# Acknowledgments

First of all, I want to thank my family for their great support, which made this work possible in the first place. I especially want to express my gratitude to my mother Birgit, who encouraged me so many times throughout the past year. Furthermore, I want to thank my sister Sandy as well as Gerrit Buck for the great assistance they provided with technical information regarding the construction of the diagnostics.

I am deeply thankful to my best friend and colleague, Torsten Stange, for his amazing mental and professional support in the last year. The endless common night shifts and the shared liters of coffee will remain unforgettable to me.

With respect to the scientific support, for the supply of data on Langmuir probe measurements, the proof-reading of this thesis, as well as for the many lessons in our office, I want to express my gratitude to my co-worker, Stefan Marsen. I am also grateful to the whole WEGA team for their continuously support. I especially want thank the WEGA machine operators for making my desired discharge scenarios possible. Special recognition goes out to Dieter Aßmus. Furthermore, I also want to thank Matthias Otte for his continuously help, his encouraging words, and for the proof-reading.

I would like to express my particular gratitude to Joachim Geiger and Andreas Werner for the very helpful discussions and many essential contributions to my work. It is also a pleasure to thank the whole CoDaC team for always being quick to help. A special thank goes to Torsten Bluhm for his support with the Wendelstein W7-X control and data acquisition system. Furthermore, I am deeply grateful to Mirko Marquardt for their fast implementation of electronics work.

Additionally, I want to thank my scientific supervisor, Heinrich Laqua, for his valuable suggestions, scientific explanations and advice, as well as much guidance through this work. I am thankful for the many talks he and I had regarding current drive experiments. I also want to express my sincere gratitude to Professor Dr. Dr. Friedrich Wagner for the allocation of my topic, therefore giving me the opportunity to work at the IPP. I am really thankful for all of the helpful advice and discussions during our meetings.



# 8 Appendix

Regarding the cable drawing for the magnetic diagnostics, the determination of the maximum misalignment of the windings inside the pipes, which cause a change of the flux area, is shown for the different coils.

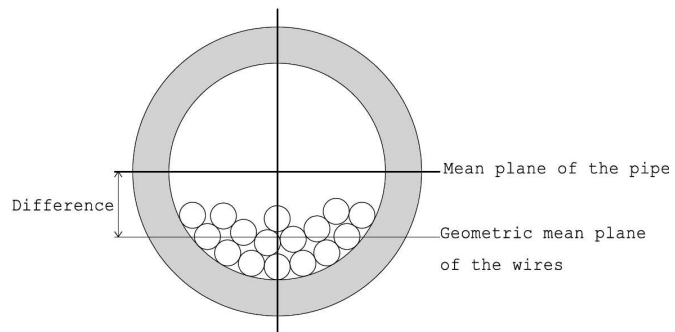


*Figure .1: Diamagnetic loop consisting of 16 windings*

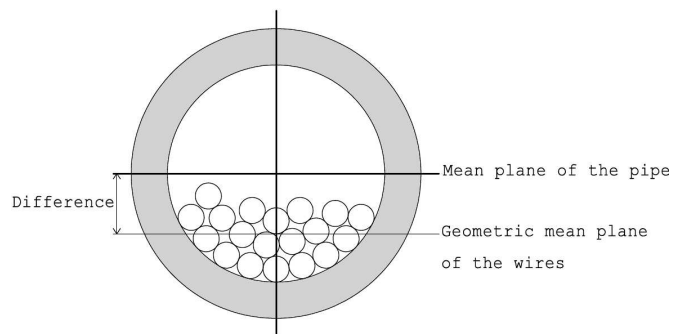


*Figure .2: Compensation loop consisting of 19 windings*

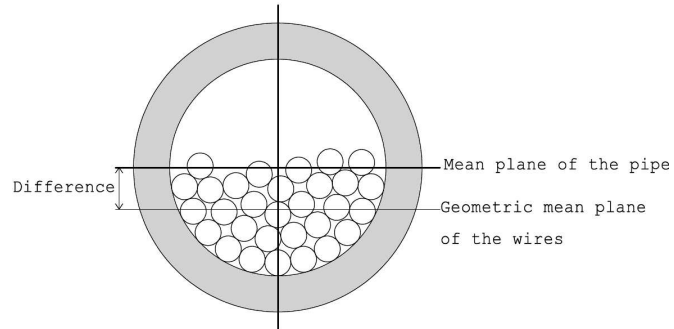


**Figure .3:** Diamagnetic loop of the two-loop system consisting of 30 windings each

**Table 8.1:** Maximal deviation of the cable paket inside the pipe againt the pipe axis

	windings	deviation/mm
diamagnetic loop	16	1.81
compensation coil	19	1.67
two-loop system	30	1.16

# Bibliography

- [AAK93] ALI-ARSHAD, S. ; KOCK, L. de: Long-pulse analog integration. In: *Rev. Sci. Instrum.* 64 (1993), Nr. 9, 2679-2682. <http://dx.doi.org/10.1063/1.1143855>. – DOI 10.1063/1.1143855
- [Ba01] BESSHOU, S. ; AL. et: Diamagnetic double-loop method for a highly sensitive measurement of energy stored in a Stellarator plasma. In: *Rev. Sci. Instrum.* 72 (2001), S. 3859
- [Bet39] BETHE, I.A.: Energy Production in Stars. In: *Phys. Rev.* 55 (1939), Mar, Nr. 5, S. 434–456. <http://dx.doi.org/10.1103/PhysRev.55.434>. – DOI 10.1103/PhysRev.55.434
- [BHI<sup>+</sup>77] BLANC, P. ; HESS, W. ; ICHTCHENKO, G. ; LALLIA, P. ; NGUYEN, T. ; TONON, G. ; MAHN, C. ; OHLENDORF, W. ; PACHER, G. ; PACHER, H. ; WEGROWE, J.: RF Heating Experiments in the WEGA Tokamak. In: *Journal de Physique Colloques* 38 (1977), S. C3–165–C3–169
- [BLS04] BAK, J. G. ; LEE, S. G. ; SON, DeRac: Performance of the magnetic sensor and the integrator for the KSTAR magnetic diagnostics. In: *Rev. Sci. Instrum.* 75 (2004), S. 4305
- [Che74] CHEN, F. F.: *Introduction to plasma physics*. New York: Plenum Press, 1974
- [CSR50] COHEN, Robert S. ; SPITZER, Lyman ; ROUTLY, Paul M.: The Electrical Conductivity of an Ionized Gas. In: *Phys. Rev.* 80 (1950), Oct, Nr. 2, S. 230–238. <http://dx.doi.org/10.1103/PhysRev.80.230>. – DOI 10.1103/PhysRev.80.230
- [EG94] ERCKMANN, V. ; GASPARINO, U.: Electron cyclotron resonance heating and current drive in toroidal fusion plasmas. In: *Plasma Phys. Controlled Fusion* 36 (1994), S. 12
- [FB80] FISCH, N.J. ; BOOZER, A.H.: Creating an Asymmetric Plasma Resistivity with Waves. In: *Phys. Rev. Lett.* 45 (1980), Sep, Nr. 9, S. 720–722. <http://dx.doi.org/10.1103/PhysRevLett.45.720>. – DOI 10.1103/PhysRevLett.45.720



- [Fis87] FISCH, Nathaniel J.: Theory of current drive in plasmas. In: *Rev. Mod. Phys.* 59 (1987), Jan, Nr. 1, S. 175–234. <http://dx.doi.org/10.1103/RevModPhys.59.175>. – DOI 10.1103/RevModPhys.59.175
- [Fre08] FREIDBERG, Jeffrey P.: *Plasma physics and fusion energy*. Cambridge : Cambridge Univ. Press, 2008
- [GCH<sup>+</sup>01] GANDINI, F. ; CIRANT, S. ; HIRSCH, M. ; LAQUA, H. P. ; NOWAK, S. ; A. BRUSCHI AND, G. G. ; ERCKMANN, V. ; MELLERA, V. ; MUZZINI, V. ; NARDONE, A. ; SIMONETTO, A. ; SOZZI, C. ; SPINICCHIA, N.: The detection of the non-absorbed millimeterwave power during EC heating and current drive. In: *Fusion Eng. Des.* 56-57 (2001), S. 975–979
- [Gei09] Private communications with Joachim Geiger
- [Gla10] GLAUBITZ, Michael: *Bolometer-Optimierung und -Anwendung auf WEGA-Plasmen*, Ernst-Moritz-Arndt-Universität Greifswald, Diplomarbeit, 2010
- [Glt99] GUANG-LI, Kuang ; TEAM, The HT-7: Experimental Research on Lower Hybrid Current Drive in Superconducting Tokamak HT-7. In: *Plasma Science and Technology* 1 (1999), Nr. 1, S. 7
- [Har07] HARTFUSS, Jürgen: *Mikrowellendiagnostik (lecture script)*. 2007
- [Hir80] HIRSHMAN, S. P.: Classical collisional theory of beam-driven plasma currents. In: *Phys. Fluids* 23 (1980), S. 1238
- [HKW06] HARTFUSS, H.-J. ; KÖNIG, R. ; WERNER, A.: Diagnostics for steady state plasmas. In: *Plasma Phys. Control. Fusion* 48 (2006), S. R83–R150
- [Hor04] HORVATH, Kinga: *Characterisation and Optimisation of WEGA Plasmas*, Ernst-Moritz-Arndt-Universität Greifswald, Diss., 2004
- [HRM86] HIRSHMAN, S. P. ; RIJ, W. I. ; MERKEL, P.: Three-dimensional free boundary calculations using a spectral Green's function method. In: *Computer Physics Communications* 43 (1986), Nr. 1, 143 - 155. [http://dx.doi.org/DOI:10.1016/0010-4655\(86\)90058-5](http://dx.doi.org/DOI:10.1016/0010-4655(86)90058-5). – DOI DOI: 10.1016/0010-4655(86)90058-5. – ISSN 0010-4655
- [HWM<sup>+</sup>08] HENNIG, Ch. ; WERNER, A. ; MARQUARDT, M. ; BLUHM, T. ; KROISS, H. ; KÜHNER, G. ; HEIMANN, P. ; MAIER, J. ; RIEMANN, H. ; ZILKER, M.: Continuous data acquisition with online analysis for the Wendelstein 7-X magnetic diagnostics. In: *Fusion Eng. Des.* 83 (2008), Nr. 2-3, 321 -

325. <http://dx.doi.org/DOI:10.1016/j.fusengdes.2007.09.003>. – DOI DOI: 10.1016/j.fusengdes.2007.09.003. – ISSN 0920–3796. – Proceedings of the 6th IAEA Technical Meeting on Control, Data Acquisition, and Remote Participation for Fusion Research
- [JD02] JOFFRIN, E. ; DEFASNE, P.: Differential method for the real time measurement of the diamagnetic beta and internal inductance in Tore Supra. In: *Rev. Sci. Instrum.* 73 (2002), Nr. 6, 2266–2269. <http://dx.doi.org/10.1063/1.1475350>. – DOI 10.1063/1.1475350
- [KLBS08] KA, E. M. ; LEE, S. G. ; BAK, J. G. ; SON, D.: Performance test of the integrator system for magnetic diagnostics in KSTAR. In: *Rev. Sci. Instrum.* 79 (2008), Nr. 10, 10F119. <http://dx.doi.org/10.1063/1.2966396>. – DOI 10.1063/1.2966396
- [LBK+08] LEE, S. G. ; BAK, J. G. ; KA, E. M. ; KIM, J. H. ; HAHN, S. H.: Magnetic diagnostics for the first plasma operation in Korea Superconducting Tokamak Advanced Research. In: *Rev. Sci. Instrum.* 79 (2008), Nr. 10, 10F117. <http://dx.doi.org/10.1063/1.2953587>. – DOI 10.1063/1.2953587
- [LEH+97] LAQUA, H. P. ; ERCKMANN, V. ; HARTFUSS, H. J. ; LAQUA, H. ; ECRH GROUP, W7-AS T.: Resonant and Nonresonant Electron Cyclotron Heating at Densities above the Plasma Cutoff by O-X-B Mode Conversion at the W7-As Stellarator. In: *Phys. Rev. Lett.* 78 (1997), May, Nr. 18, S. 3467–3470. <http://dx.doi.org/10.1103/PhysRevLett.78.3467>. – DOI 10.1103/PhysRevLett.78.3467
- [LMM+03] LAQUA, H. P. ; MAASSBERG, H. ; MARUSHCHENKO, N. B. ; VOLPE, F. ; WELLER, A. ; KASPAREK, W.: Electron-Bernstein-Wave Current Drive in an Overdense Plasma at the Wendelstein 7-AS Stellarator. In: *Phys. Rev. Lett.* 90 (2003), Feb, Nr. 7, S. 075003. <http://dx.doi.org/10.1103/PhysRevLett.90.075003>. – DOI 10.1103/PhysRevLett.90.075003
- [LMV+03] LAQUA, H.P. ; MAASSBERG, H. ; VOLPE, F. ; TEAM, W7-AS ; ECRH-GROUP: Electron Bernstein wave heating and current drive in overdense plasmas at the W7-AS stellarator. In: *Nucl. Fusion* 43 (2003), S. 1324–1328
- [LST94] LITVAK, A.G. ; SUVOROV, E.V. ; TOKMAN, M.D.: On the possibility of current drive in tokamaks by Bernstein modes. In: *Phys. Lett. A* 188 (1994), S. 64–67
- [MBT03] MORET, J.-M. ; BUHLMANN, F. ; TONETTI, G.: Fast single loop diamagnetic measurements on the TCV toka-

- mak. In: *Rev. Sci. Instrum.* 74 (2003), Nr. 11, 4634-4643. <http://dx.doi.org/10.1063/1.1614856>. – DOI 10.1063/1.1614856
- [Mül10] MÜLLER, Eric: *Aufbau einer Supersonic Helium Beam Diagnostik und erste Untersuchungen am WEGA-Stellarator*, Ernst-Moritz-Arndt-Universität Greifswald, Diplomarbeit, 2010
- [Nüh07] NÜHRENBERG, Jürgen: *Stellaratortheorie*. WS 2006/2007. – Skript
- [NI] <http://www.ni.com/pdf/products/us/3sv414-416.pdf>
- [NRL] NRL: *NRL Plasma Formulary*
- [OKAIa+01] OIKAWA, T. ; KAMADA, Y. ; A. ISAYAMA AND, T. F. ; SUZUKI, T. ; UMEDA, N. ; KAWAI, M. ; KURIYAMA, M. ; GRISHAM, L.R. ; IKEDA, Y. ; KAJIWARA, K. ; USHIGUSA, K. ; TOBITA, K. ; MORIOKA, A. ; TAKECHI, M. ; ITOH, T. ; TEAM, JT-60: Reactor relevant current drive and heating by N-NBI on JT-60U. In: *Nucl. Fusion* 41 (2001), S. 1575–1583
- [Pee00] PEETERS, A. G.: The bootstrap current and its consequences. In: *Plasma Phys. Control. Fusion* 42 (2000), S. B231–B242
- [Pod06] PODOBA, Yurij: *Radio frequency heating on the WEGA stellarator*, Ernst-Moritz-Arndt-Universität Greifswald, Diss., 2006
- [REG+97] ROME, M. ; ERCKMANN, V. ; GASPARINO, U. ; HARTFUSS, H. J. ; KÜHNER, G. ; MAASSBERG, H. ; MARUSHCHENKO, N.: Kinetic modelling of the ECRH power deposition in W7-AS. In: *Plasma Phys. Control. Fusion* 39 (1997), S. 117
- [Rog12] ROGOWSKI, Walter: Die Messung der magnetischen Spannung. In: *Archiv für Elektrotechnik und Übertragungstechnik* (1912)
- [SFMT08] STRAIT, E. J. ; FREDRICKSON, E. D. ; MORET, J.-M. ; TAKECHI, M.: Chapter 2: Magnetic Diagnostics. In: *Fusion Sci. Technol.* 53 (2008), S. 304–334
- [SH53] SPITZER, Lyman ; HÄRM, Richard: Transport Phenomena in a Completely Ionized Gas. In: *Phys. Rev.* 89 (1953), Mar, Nr. 5, S. 977–981. <http://dx.doi.org/10.1103/PhysRev.89.977>. – DOI 10.1103/PhysRev.89.977
- [Sha98] SHANNON, C. E.: Communication in the Presence of Noise. In: *Proc. IEEE* 86 (1998), S. 447
- [Spi62] SPITZER, L. ; SPITZER, L. (Hrsg.): *Physics of Fully Ionized Gases*. Interscience Publishers, 1962

- 
- [Sta09] Weekly talks with Torsten Stange
- [Sti62] STIX, Thomas H.: *The Theory of Plasma Waves*. McGraw-Hill, Inc., 1962
- [SWZ04] SHEN, B. ; WAN, B.N. ; ZHANG, X.Q.: Diamagnetic measurement on HT-7 superconducting tokamak. In: *Fusion Eng. Des.* 70 (2004), S. 311–318
- [TCK86] TONETTI, G. ; CHRISTIANSEN, J. P. ; KOCK, L. de: Measurement of the energy content of the JET tokamak plasma with a diamagnetic loop. In: *Rev. Sci. Instrum.* 57 (1986), Nr. 8, 2087-2089. <http://dx.doi.org/10.1063/1.1138747>. – DOI 10.1063/1.1138747
- [Urb09] Private communication with Jakub Urban
- [Wag07] WAGNER, F.: *Hochtemperturplasmaphysik*. WS 2006/2007
- [WC87] WESSON, John. ; CONNOR, J. W.: *Tokamaks*. Clarendon Press, Oxford ; New York :, 1987. – x, 309 p. : S. – ISBN 0198563280
- [WEGK08] WERNER, Andreas ; ENDLER, Michael ; GEIGER, Joachim ; KOENIG, Ralf: W7-X magnetic diagnostics: Rogowski coil performance for very long pulses. In: *Rev. Sci. Instrum.* 79 (2008), Nr. 10, 10F122. <http://dx.doi.org/10.1063/1.2957933>. – DOI 10.1063/1.2957933
- [Wer06] WERNER, A.: W7-X magnetic diagnostics: Performance of the digital integrator. In: *Rev. Sci. Instrum.* 77 (2006), Nr. 10, 10E307. <http://dx.doi.org/10.1063/1.2220073>. – DOI 10.1063/1.2220073
- [Wer09] Private communications with Andreas Werner



# List of Tables

2.1	Ionic charge dependence on $\gamma_E$ . . . . .	33
4.1	Dimensions of the used pipes for construction the diamagnetic loop .	47
4.2	Dimensions of pipes used for construction of the compensation loop .	49
4.3	Dimensions of the pipes used for construction of the 2-loop system . .	51
4.4	Signal at the different channels of the intgrator board and ADC . . .	61
5.1	<i>Calibration factors showing value for measured current per integrated unit for the different Rogowski coils . . . . .</i>	<i>67</i>
8.1	Maximal deviation of the cable paket inside the pipe againt the pipe axis . . . . .	104



# List of Figures

1.1	Binding energy per nucleon in dependency on the mass number A . . .	2
1.2	Reactions rate for possible fusion processes in dependence on the temperature [Har07] . . . . .	2
1.3	Motion of charged particles along magnetic field lines . . . . .	4
1.4	Coordinate system for a toroidal symmetry . . . . .	5
1.5	Schematic setup of a tokamak . . . . .	6
1.6	Schematic setup of a classical stellarator . . . . .	6
1.7	Schematic diagram of the WEGA stellarator and the flux surfaces . .	8
1.8	Movable mirror system at WEGA for changing the heating scenario .	9
1.9	Overview of diagnostics at the WEGA stellarator . . . . .	10
2.1	Diamagnetic particle drift leads to a current perpendicular to the magnetic field and pressure . . . . .	13
2.2	Resultant diamagnetic current in the single particle model due to temperature gradient (a) and density gradient (b) . . . . .	14
2.3	Coordinate system used for screw pinch symmetry . . . . .	14
2.4	High plasma pressure leads to the increase of plasma beta and to a reduction of the inner magnetic field . . . . .	19
2.5	Transformer used for current drive in fusion device . . . . .	25
2.6	Influence of phase space by the diffusion operator [REG <sup>+</sup> 97] . . . . .	27
2.7	Influence of trapped particle cone for current drive . . . . .	27
2.8	Generated current by means of multi pass absorption of the ECRH wave . . . . .	28
2.9	Velocity distribution of the electrons by using lower hybrid waves with a parallel phase velocity between 3 and 5 times the thermal velocity for current drive [Fis87] . . . . .	29
2.10	Influence of phase space by the diffusion operator for electron Bernstein waves [LMM <sup>+</sup> 03] . . . . .	30
2.11	Banana orbit in a magnetically confined plasma . . . . .	31
3.1	Rogowski coil . . . . .	36
3.2	Flux area of a diamagnetic and compensation coil . . . . .	38
3.3	2-loop system used to measure the plasma energy . . . . .	40
3.4	Passive RC-integrator and RL-integrator . . . . .	41
3.5	Active integrator . . . . .	42
3.6	Principle of the digital integrator . . . . .	43



---

4.1	Signal path for the evaluation of magnetic diagnostic measurements at WEGA . . . . .	46
4.2	Setup of the diamagnetic loop consisting of 4 stainless steel pipes . . .	47
4.3	Change of the position of the pipes in order to implement the shielded loop inside the WEGA torus . . . . .	48
4.4	Mounting device for diamagnetic loop . . . . .	48
4.5	Destroyed diamagnetic loop in 2006 . . . . .	49
4.6	Mounting structure for assembling the compensation coil . . . . .	50
4.7	System of diamagnetic (in front) and compensation loop (back) . . .	50
4.8	Two segmented external Rogowski coil for plasma current measurements	52
4.9	2nd magnetic diagnostic system consisting of two diamagnetic loops (white cables) and the internal Rogowski coil (red cable) . . . . .	53
4.10	Rogowski coils to measure the toroidal (a), helical (b) and vertical (c) field coil current . . . . .	54
4.11	Example of magnetic flux surfaces at WEGA for $t \approx 0.2$ . . . . .	54
4.12	Magnetic flux surface including the LCFS for the planes with a vertical plasma ellipse . . . . .	54
4.13	Magnetic diagnostics mounted inside the vacuum vessel where the access is only possible through the existing ports. The picture was also made through one port. . . . .	55
4.14	Top: raw signal coming from magnetic diagnostics after the chopping process; middle: integrator clock signal (black) and generated mask signal (red); bottom: raw signal multiplied by mask signal . . . . .	57
4.15	Interpolation (orange curve) of the missing samples due to the switching process of the digital integrator by means of a left $f_l$ (blue) and a right regression line $f_r$ (green) as well as a direct line $f_d$ (red) . . .	58
4.16	Comparison of the integrated (bottom) and reconstructed raw signal (top) between the newly developed code (black solid line) and the prior used code based on an average process (red dash dot line)[Wer06]	59
4.17	High temporal resolution of the integrated signal showing a WEGA field pulse and the temporal magnetic field ripple . . . . .	60
4.18	Pin configuration of the intergrator boards . . . . .	60
4.19	Saturation of the amplifier (red boxes in the top) leading to errors in the flux measurements (bottom) . . . . .	62
4.20	Interactive user interface of the program MagPlot used for data processing of the signal measured by the magnetic diagnostics as well as other diagnostics . . . . .	63
4.21	Interface to control the different digital integrator and analog-to-digital converter channels in order to convert the data, written in the Objectivity data bank system, into netCDF files . . . . .	64
5.1	Setup used for calibration of the different Rogowski coils . . . . .	66
5.2	Time development of the magnetic field used for calibration of the inductive diagnostics . . . . .	67

5.3	Difference of the flux signals of the diamagnetic loop and compensation loop allowing a relative resolution of $3 \cdot 10^{-5}$ . . . . .	68
5.4	Change in the calibration factor D and k with respect to a change in the toroidal magnetic field . . . . .	69
5.5	Time traces of a ECRH helium discharge. From top to bottom are shown: the magnetic field B on the torus axis, the neutral gas pressure $p_N$ , the forward power of the gyrotron P, the sniffer signal, the line integrated density $ndl$ and the plasma current $I_{pl}$ . . . . .	70
5.6	Neutral gas pressure and ECRH power scan for plasma current measurement . . . . .	71
5.7	Plasma current measured for different radiation angles of the microwave . . . . .	72
5.8	Influence of the bootstrap current by changing magnetic field direction from clockwise (black) to anti-clockwise (red) leading to change in plasma current direction . . . . .	73
5.9	Time development of lower hybrid current drive discharge . . . . .	74
5.10	Plasma current dependence on injected power of radiated waves with a frequency of 2.45 GHz . . . . .	75
5.11	Plasma current driven by lower hybrid waves for different densities and neutral gas pressures. Different lines corresponding to values taken from different points during the power ramp up time . . . . .	76
5.12	Plasma current developing for the case having a line-integrated density above $8 \cdot 10^{17} \text{ m}^{-2}$ during the non-resonant heating phase . . . . .	77
5.13	Current drive efficiency for discharges in helium with a injected non-resonant power up to 10.4 kW . . . . .	78
5.14	Discharge developing for the examination of the plasma current and pressure in an OXB heated plasma. From top to bottom are shown: toroidal magnetic field $B$ , neutral gas pressure $p_N$ , forward power of the 28 GHz gyrotron (resonant) and 2.45 GHz magnetron as well as its reflected power, sniffer signal, line-integrated electron density $ndl$ , and plasma current $I_{pl}$ . . . . .	79
5.15	Plasma current measured for two different discharges which distinguish by a change in the gas inlet by 6 percent resulting in reaching the OXB phase for 34956 (black) compared with 34957 (red) . . . . .	81
5.16	Plasma current in OXB regime in dependency on neutral gas pressure for discharges with argon (blue), helium (black) and helium by additional use of the magnetron (red) . . . . .	82
5.17	Power modulation of the gyrotron to investigate the plasma current behavior during OXB transition . . . . .	83
5.18	Plasma current change with transition in OXB regime for argon . . . . .	84
5.19	Plasma current change with transition in OXB regime for helium by additional use of permanent magnetron power of 14 kW . . . . .	84
5.20	Inductively driven plasma current for discharges with different densities . . . . .	85
5.21	Temperature profile measured by a Langmuir probe to support the electron temperature determined by means of the Spitzer resistivity . . . . .	86

5.22	Flux change measured during leaving OXB phase by means of the conventional diamagnetic system as well as the 2-loop system . . . . .	87
5.23	Ohmic transformer used at the end of the discharge for plasma current compensation . . . . .	88
5.24	Plasma energy change measured by the two-loop system as well as the conventional system at the transition from and into the OXB regime for helium with additional use of permanent injected magnetron power of 12 kW . . . . .	90
5.25	Plasma energy change measured by the two-loop system as well as the conventional system by the transition from and into OXB regime for argon . . . . .	91
5.26	Plasma energy change measured by the two-loop system as well as the conventional system for the switching off process of the plasma averaged over 11 helium discharges . . . . .	92
5.27	Plasma pressure determined by means of Langmuir probe measurements	93
.1	Diamagnetic loop consisting of 16 windings . . . . .	103
.2	Compensation loop consisting of 19 windings . . . . .	103
.3	Diamagnetic loop of the two-loop system consisting of 30 windings each . . . . .	104